X-RAY DOSE DEPENDENCE OF DARK CURRENT IN AMORPHOUS SELENIUM-ALLOY X-RAY PHOTOCONDUCTORS

A Thesis Submitted to the College of

Graduate Studies and Research

In Partial Fulfillment of the Requirements for the Degree of Master of Science

In the Department of Electrical and Computer Engineering

University of Saskatchewan Saskatoon, SK, Canada

by

KALAIVANI PACHAI CHETTIAR SADASIVAM

Saskatoon, Saskatchewan, Canada

PERMISSION TO USE

In presenting this thesis/dissertation in partial fulfillment of the requirements for a Postgraduate degree from the University of Saskatchewan, I agree that the Libraries of this University may make it freely available for inspection. I further agree that permission for copying of this thesis/dissertation in any manner, in whole or in part, for scholarly purposes may be granted by the professor or professors who supervised my thesis/dissertation work or, in their absence, by the Head of the Department or the Dean of the College in which my thesis work was done. It is understood that any copying or publication or use of this thesis/dissertation or parts thereof for financial gain shall not be allowed without my written permission. It is also understood that due recognition shall be given to me and to the University of Saskatchewan in any scholarly use which may be made of any material in my thesis/dissertation.

DISCLAIMER

The [name of company/corporation/brand name and website] were exclusively created to meet the thesis and/or exhibition requirements for the degree of [title of degree] at the University of Saskatchewan. Reference in this thesis/dissertation to any specific commercial products, process, or service by trade name, trademark, manufacturer, or otherwise, does not constitute or imply its endorsement, recommendation, or favoring by the University of Saskatchewan. The views and opinions of the author expressed herein do not state or reflect those of the University of Saskatchewan, and shall not be used for advertising or product endorsement purposes.

Requests for permission to copy or to make other uses of materials in this thesis/dissertation in whole or part should be addressed to:

Head of the Department of Electrical and Computer Engineering

3B48 Engineering Building

57 Campus Drive,

Saskatoon, Saskatchewan S7N 5A9 Canada

OR

Dean

College of Graduate Studies and Research

University of Saskatchewan

107 Administration Place

Saskatoon, Saskatchewan S7N 5A2 Canada

ABSTRACT

The dark current is an important characteristic of a photoconductive X-ray detector, and can impact the dynamic range of the detector and its detective quantum efficiency. It is therefore essential that the dark current and its behavior with time and x-ray irradiation are well characterized and understood in amorphous selenium (a-Se) X-ray detectors for the future enhancement of these detectors. Throughout the course of this work, the dark current in practical a-Se multilayer photoconductors were studied as function of time and x-ray dose delivered to the detector material. The dark current in these multilayer structures has been measured as a function of different rest time periods, sample structure, single X-ray irradiation on the sample and multiple irradiation on the sample. Experiments were performed by resting the sample in dark for a period of time (24 hours) and then samples were exposed to X-ray radiation. It has been observed that most of the trapped charge carriers in the bulk of the material are discharged after resting the sample in dark for 24 hours. It was observed that multilayer sample structures *p-i-n* and *n-i-p* exhibit much less dark current compared to other samples with single layer and double layer structures, that is, *i*-layer only, *n-i* and *p-i* structures. The experiments support that the dark current is controlled by injection of charge carriers from contacts. Single X-ray irradiation and multiple irradiation experiments were performed on multilayer a-Se photoconductors at a dose rate of 0.51 Gy s^{-1} with an exposure duration of 3 s. Samples were exposed to single irradiation at 100 s and 400 s. The dark current following the photocurrent was recorded. Multiple irradiation experiments were also performed on these multilayer samples. With different reverse bias voltages, samples were irradiated 10 times from 200s to 2000s. It was found that the dark current tends to increase with repeated X-ray irradiation but the increase depends on the applied reverse bias; the increase is negligible at a field of 10 V μm^{-1}. After the cessation of the irradiation, the dark current decays and tends to reach a steady state value at t = 4000s. After 24 hr of resting in the dark, the dark current was nearly as low as the original dark current before the X-ray irradiation.

ACKNOWLEDGEMENT

I would like to say my sincere thanks to all those who made the completion of this work to a reality. First of all, I would like to thank my husband Karthikeyan Narayanan who helped me to pursue my dreams and provided continuous support during the MSc program. I would also like to thank my Mother, Vanaja and Uncle, Baskaran for always inspiring me to pursue my academic dreams. I am greatly indebted to my supervisor Dr. S.O. Kasap whose supervision and understanding have guided me academically and professionally. I would like to extend my thanks to Dr. George Belev who have been instrumental in carrying out this work. I am grateful to Dr. Kasap for providing financial support during the course of this work. I thank all the faculty members and my colleague Dr. Joel Frey who guided me to carry out the work.

TABLE OF CONTENTS

LIST OF TABLES

LIST OF FIGURES

LIST OF ABBREVIATIONS

AB	Anti-Bonding
AMA	Active Matrix Array
a-Se	Amorphous Selenium
CB	Conduction Band
CCE	Charge Collection Efficiency
CZT	Cadmium Zinc Telluride
DC	Direct Current
DOS	Density Of States
DQE	Detective Quantum Efficiency
DR	Dynamic Range
EHP	Electron-Hole Pair
ESR	Electron Spin Resonance
FPXI	Flat Panel X-ray Imager
GPIB	General Purpose Interface Bus
IFTOF	Interrupted Field Time-Of-Flight
IR	Infrared
ITO	Indium-Tin-Oxide
IVAP	Intimate Valence Alternation Pair
LDOS	Localized Density of states
LP	Lone Pair
MRI	Magnetic Resonance Imaging
MTF	Modulation Transfer Function
NB	Non-Bonding
O	Over-coordinated
PDF	Probability Density Function
PE	Potential Energy
ppm	parts-per-million
PVD	Physical Vapour Deposition
QE	Quantum Efficiency
SNR	Signal to Noise Ratio
TFT	Thin Film Transistor
TOF	Time-Of-Flight
U	Under co-ordinated
VAP	Valence Alternation Pair
VB	Valence Band

CHAPTER 1. INTRODUCTION

1.1 X-ray Imaging

X-rays was discovered by German scientist Wilhelm Röntgen on the 8th November 1895. Röntgen was investigating a phenomena caused during the passage of an electrical discharge from an induction coil through a partially evacuated glass tube. Although the tube was completely covered with black paper and the whole room was dark, he observed that, a paper screen covered with the fluorescent material barium platino-cyanide became illuminated elsewhere in the room [1]. Röntgen named these unknown rays of invisible light as X-rays. His discovery spread quickly throughout the world and due to the availability of the cathode tubes, his experiments could be duplicated with ease. The X-rays were soon incorporated into clinical studies and experiments for bone fractures and gunshot wounds as early as 1896 in the US [1]. This technique of using X-rays to image anatomical body parts came to be known as Radiography [2].

In Radiography, the emission scope of X-rays is changed by an aperture. The X-rays are directly aimed at the part of the body which is to be inspected. Transmitted x-rays are made incident on a scintillator screen (intensifier screen) to generate fluorescence light. The fluorescence causes the photographic film next to the intensifier screen to capture the emitted fluorescence photons and develop an image; and is dependent on the amount of incident radiation and hence on how much radiation has passed through the bones and the soft tissues in the body. The bone is denser than the soft tissue and it blocks the radiation thereby allowing less radiation to pass through the body and appears white in the X-ray film. The soft tissues are less dense and the radiations can easily pass through and those areas appear black in the X-ray film. X-ray film development involves time consuming chemical processes and also involves concerns for being stored physically and not electronically. Considering these drawbacks in analogue imaging; digitization technique of the X-ray image became widely used and it has steadily replaced the conventional radiography [3].

1.2 Digital X-ray Imaging

Digital imaging is a replacement of conventional imaging technique and it gained widespread acceptance in 1970's. It uses flat panel detectors to capture the X-ray image and directly convert to digital form with the least number of X-ray photons. It can amplify screens, films and provide further insight in the anatomy and function of human body [4]. In conventional X-ray film imaging, the photographic emulsion film serves as an image detector, display and storage medium. Similarly, in digital radiography the imaging process can be split into several processes such as detection, digitization, image processing, storing, display and film recording as shown in Figure 1.1, and thereby performance of each process can be optimized individually in [4].

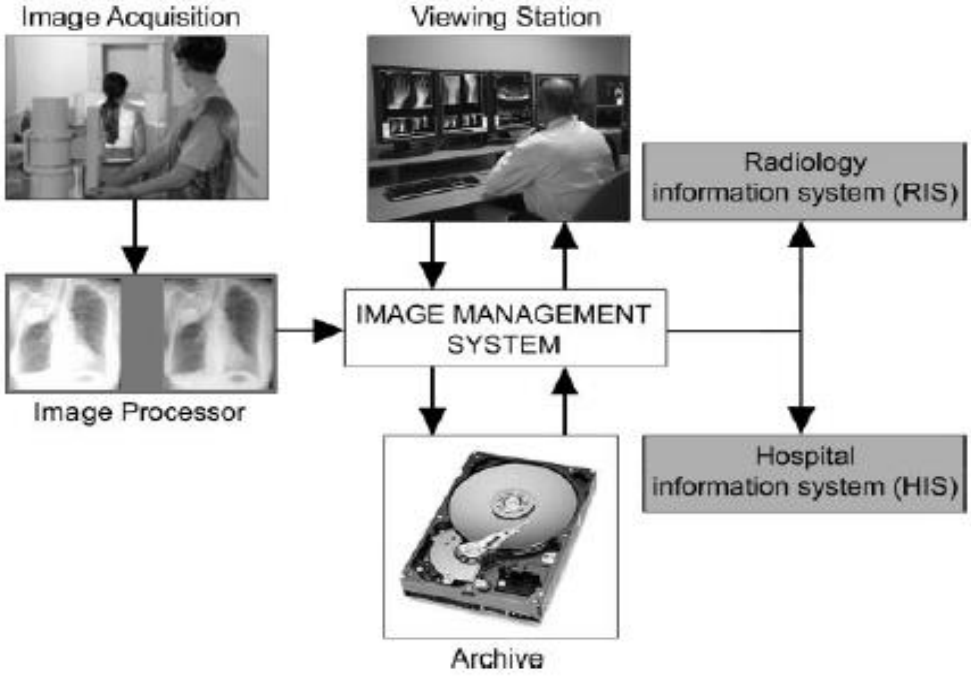

Figure 1.1: Illustration of digital radiographic system, the image is stored in a digital archive after the image is captured. The stored image will be further distributed to Information system, viewing station and electronic patient records by the image management system [5].

1.3 Digital radiography

There are two major types of digital radiography; they are computed radiography (CR) and direct radiography (DR). Both CR and DR are available for the acquisition of projection radiographs. The general description of digital radiography is illustrated in Figure 1.2. Various components of digital detectors can be seen in Table 1.1 [6].

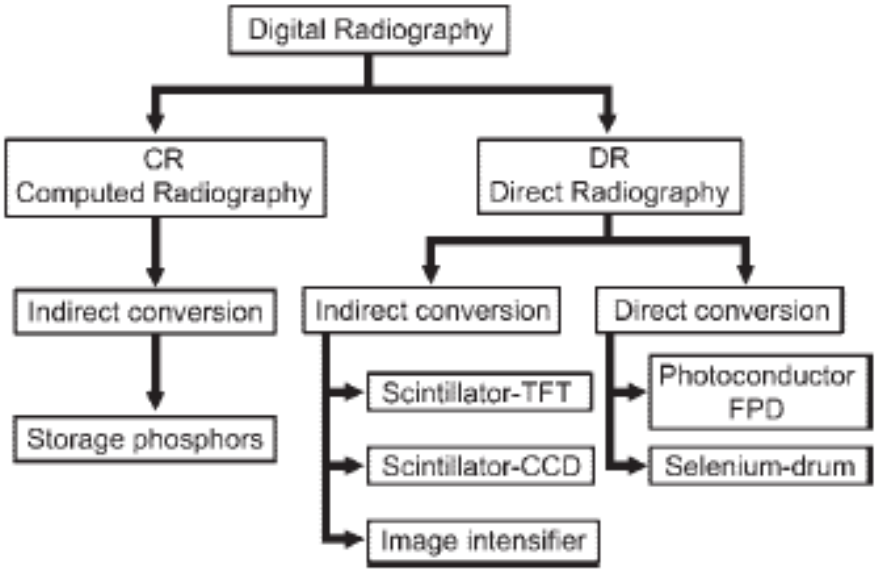

Figure 1.2: General description model of digital X-ray technology [6]

Table 1.1: Components of digital detectors [6].

Detector Technology		Capture element	Coupling element	Charge readout
Computed radiography		$BaFBr:Eu^{2+}$	Photo stimulated luminescence (PSL) light-guide	Photo-multiplier tube; signal digitization
Direct radiography	Direct flat panel conversion	a - Se	None	TFT Array
	In direct flat panel conversion	CsI or Gd_2O_2S phosphor	Contact layer	a-Si photodiode /TFT array

Computed Radiography makes use of image plates with detective layer of photostimulable crystals which contains different halogenides such as bromide, chlorine, or iodine. Storage phosphors are molded into plates in an unstructured way. Exposed X-ray energy is captured and temporarily stored in these crystals by bringing electrons to a higher energy level. The absorbed X-ray energy can be stored for several hours depending on the physical properties of phosphor crystals; however, the readout process should start as soon as possible because the amount of energy stored decreases over time. In the readout process, the stored X-ray energy in the detector is scanned pixel by pixel by a high energy laser beam and thereby the stored energy is set free as emitted light with a different wavelength from that of the laser beam. The emitted light is collected by a photodiode and it is converted to a digital image [5] Figure 1.3 illustrates the CR system based on storage phosphor plates.

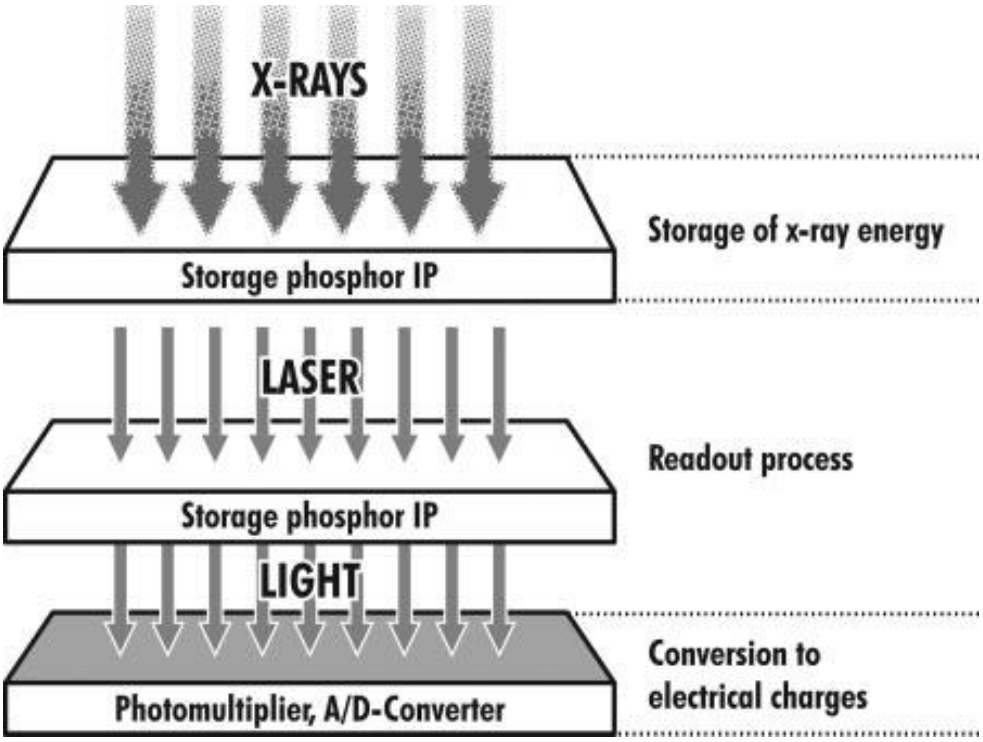

Figure 1.3: Illustration of Computed Radiography system based on storage phosphor image plates. (i) Image plate is exposed to X-ray energy and detective layer stores the energy (ii) Laser beam scans the image plate; and the stored energy is set free to emit the light. (iii) Photomultiplier collects the light and it is converted to electrical charges After [5].

Computed Radiography is also a time consuming process similar to the conventional/film screen systems and furthermore the image quality is limited Computed Radiography uses image intensifier systems and the image is obtained instantly but the quality of the image which is very important is poorer than quality produced by film based techniques. The image intensifier used is very bulky and expensive which limits the usage of Computed Radiography.

Direct radiography under Digital radiography is divided into indirect and direct conversion. In indirect conversion system, the first stage converts the X-rays into visible light using a scintillator and the second stage converts visible light into an electric charge by means of amorphous silicon photodiode array. In direct conversion, the X-ray photoconductor converts directly at one stage X-ray photons to electric charges.

Digital imaging technology uses flat panel detectors which have X-ray photon absorption layer coupled to solid state array recording layer. The photo-absorption layer converts the incident X-ray photons to electrical charges or to a visible light and the photodiode layer converts the visible light to charge. Solid state array layers are made of amorphous silicon circuits deposited on the glass plate to form an array of thin film transistors. Capacitors are connected to each transistor to collect the charge produced.

Flat panel detectors are distinguished into Direct and Indirect detectors based on the conversion process. Indirect flat panel detectors involve two processes: the first being conversion of incident X-ray energy radiation to visible light photons by scintillating phosphor layer and the second process involves the detection of these visible light photons by the pixel Figure 1.4 represents the amorphous silicon based indirect conversion DR System [7]. The scintillating phosphor layer is made of Gd_2O_2S or CsI. The electronic charges are read out by TFT array.

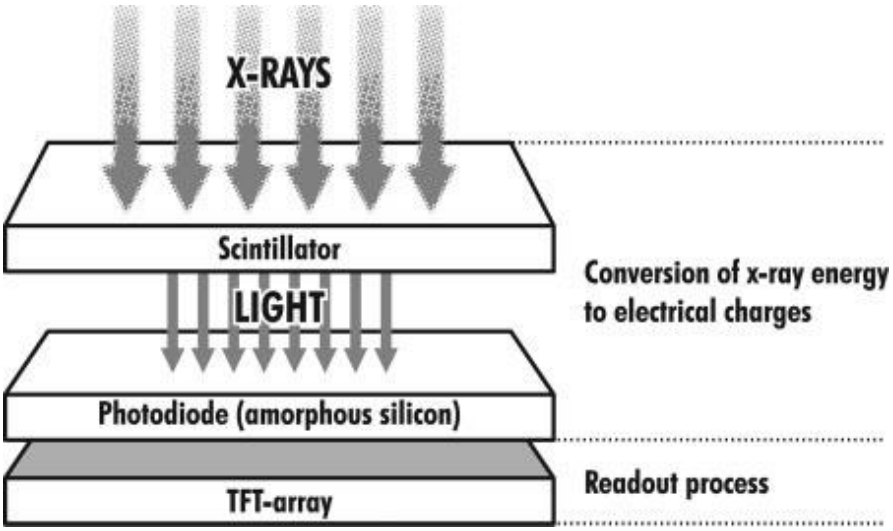

Figure 1.4: Representation of Amorphous silicon based indirect conversion DR system [5]

Direct conversion is a newer generation DR system which makes use of amorphous selenium (a-Se) based flat panel detectors. The Flat panel detector uses a layer of Selenium coupled to the array of thin film transistors (TFT). It converts the emitted X-ray photons into electrical charges and the charge pattern is recorded by the TFT array. Representation of Direct conversion flat panel detectors is shown in Figure 1.5.

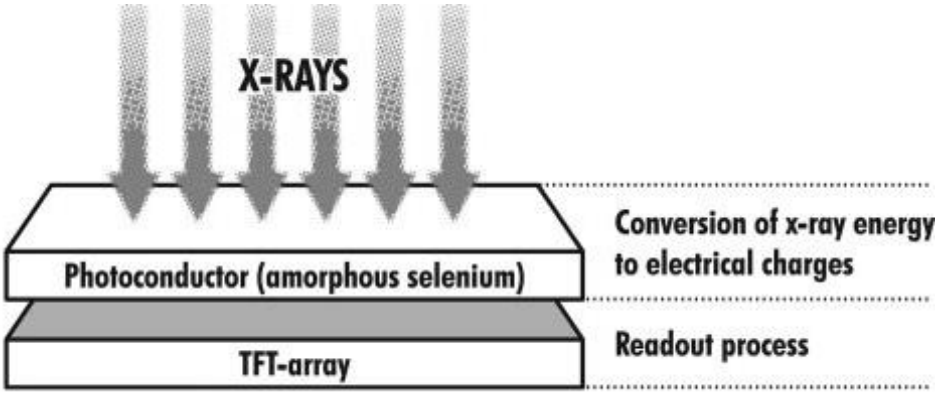

Figure 1.5: Representation of Selenium based flat panel detector system. The incident X-ray photons on the photoconductor is directly converted to electrical charge and read out by a coupled TFT array [5]

Direct conversion has a greater advantage of clinical usefulness and the flat panel detectors provides an image quality which is equivalent to the other flat panel detectors and Selenium drum detectors and it is also superior to conventional radiography.

Figure 1.6 shows the image quality of an x-ray image of a human head using flat panel detector and conventional radiography [5].

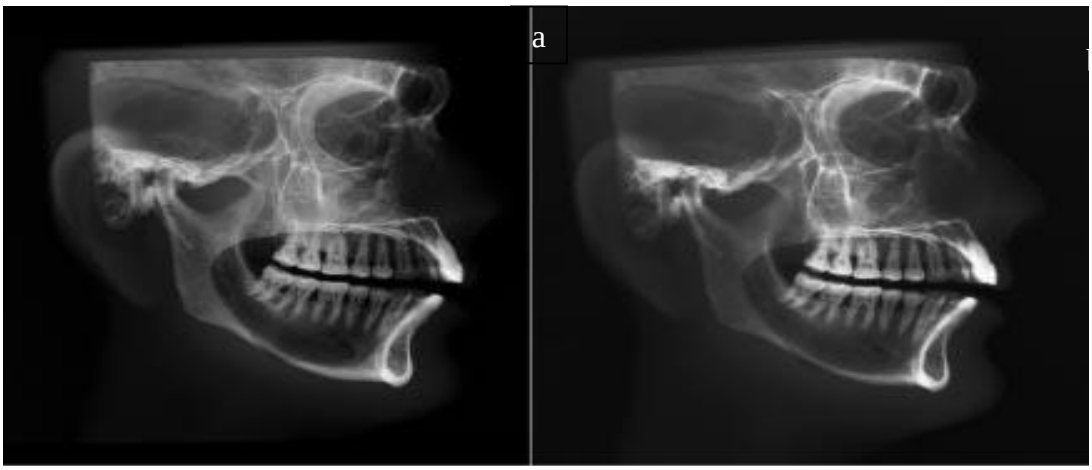

Figure 1.6: Comparison of a human skull obtained by using (a) a-Se flat panel detector (b) Conventional radiography. Selenium based flat panel detectors are widely used in a clinical application field called Mammography [3]

1.4 Applications of Digital Radiography

Digital radiography is used in the medical imaging applications. Medical imaging uses flat panel detectors that have active matrix arrays (AMA) or large integrated circuits for large- area displays [8]. The flat panel detectors are widely used in breast screening and examination of symptomatic women. According to 2014 Breast cancer statistics in Canada 14% of the cancer deaths are due to Breast cancer. An estimated 24,400 women will be diagnosed with Breast cancer and 5000 will die out of it. Increased Mammography usage in screening process has raised the breast cancer incidence rate steadily from early to late 1980's in Canada. There is

further increase in the detection of breast cancers cases in Canada due to the widespread implementation of breast cancer screening programs. [9]

Film mammography and digital mammography are used in the screening of breast cancer tissues. Unlike film mammography, digital mammography has shortened procedure time, increased dynamic range with reduced breast compression and the images taken are electronic and can be altered for contrast and resolution. Figure 1.7 represents the imaging of breast.

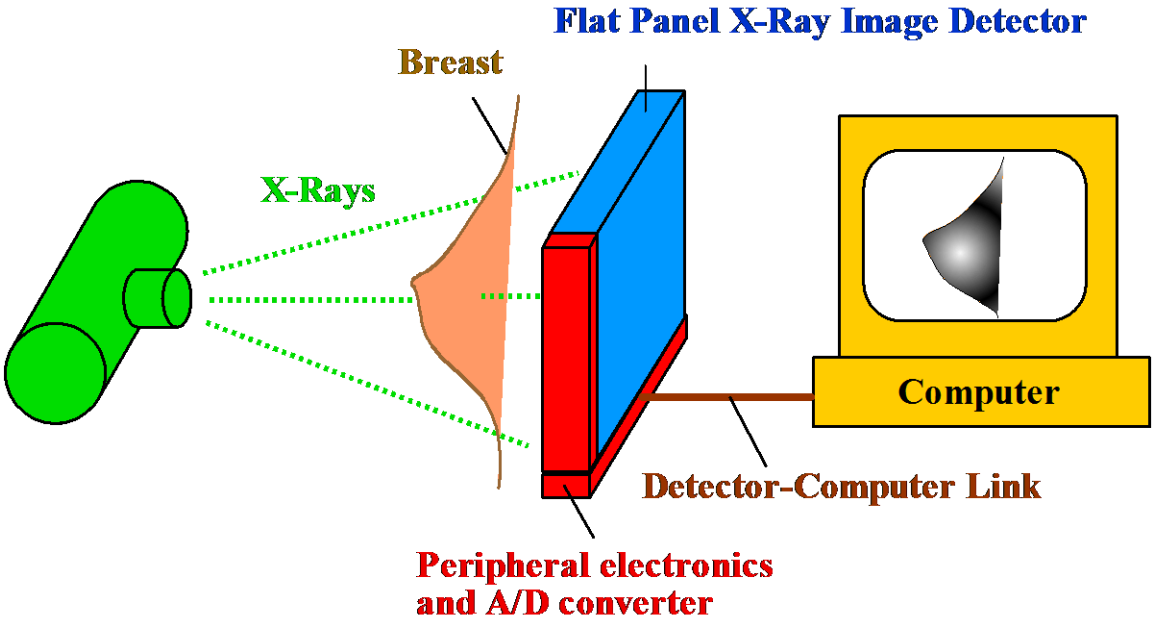

Figure 1.7: Schematic representation of a flat-panel X-ray image detector for digital mammography. The detector is connected to a computer through a convenient communication link.

It is also claimed that digital mammography gives rise to lower radiation exposure for women compared to film mammography. MRI is another method that uses no radiation for screening but the screening time is estimated to approximately 40 minutes which is even more than the film mammography [9].

More recently tomosynthesis has become another technique (recent technique of mammography) that is used in mammographic imaging. It is a new technique for capturing high resolution three-dimensional picture at radiographic dosage levels. In digital tomosynthesis, the X-ray tube moves in arc angle while the breast is compressed and series of images are taken at different

angles. During the movement of X-ray tube, sequence of exposures results in multiple projection image data sets. Multiple thin slice images of 1mm are reconstructed from the image data sets. Balance between dose and image quality is a major consideration in breast tomosynthesis that has to be taken care of by the manufacturers. As the image quality is dependent on dose a minimal higher dose greater than the current digital mammographic dose is required (http://www.ncbi.nlm.nih.gov/pmc/articles/PMC3118307/). Another recent study using tomosynthesis has said that there is relatively high image noise in the reconstructed thin slices. Therefore, the high image noise raises the value of 1 cm thick slices computed from reconstructed slices for picture interpretation (http://www.ncbi.nlm.nih.gov/pmc/articles/PMC3043718/).

Comparing all the screening techniques it is evident that digital mammography is best suited for screening breast cancer and screening at a very early stage can reduce the death rate due to breast cancer.

1.5 Direct Conversion Flat Panel Detectors in Mammography

Recent research has shown that a-Se flat panel detector is the most promising direct digital radiographic system used in medical imaging applications like mammography and it is based on using a large-area thin film transistor (TFT) active matrix array (AMA) (of the n-type used in flat panel displays) as a read-out system These direct conversion digital detectors were introduced in early 1990's by ThoraVision™ (Phillips Medical systems). In 1985 Du Pont Corporation (USA) introduced the first flat panel DR detector. In mammographic imaging, X-ray image detector must be large enough to capture image and AMA's are now available for very large areas such as 40 cm × 40cm and even larger AMA's can be made available in the future.

Active matrix arrays consist of individual pixel electrodes with TFT's connected to source and gate lines. A representation of AMA with few pixels can be seen in the Figure 1.8. Each pixel has a TFT and a storage capacitor with a capacitance value of 0.1 pF. They are connected to gate lines G_1, G_2 etc. Every pixel in the row reads the charge simultaneously and the series is repeated for each consequent row until the entire array is read out.

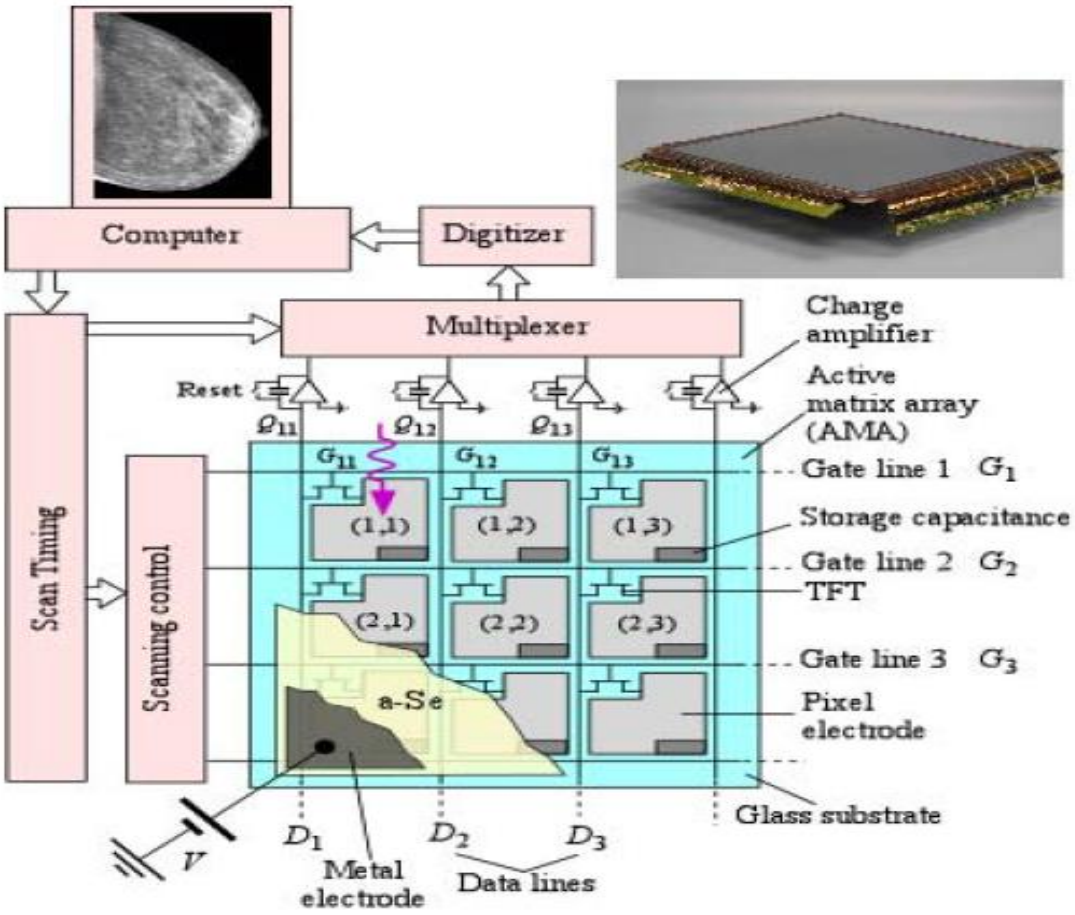

Figure 1.8: TFT active matrix array with self-scanned readout used in X-ray image detectors [3, 10].

The read out is amplified by the charge amplifier before reaching the multiplexer. The entire AMA is coated with a-Se photoconductive layer and a top electrode. Representation of a single pixel can be seen in the Figure 1.9. There is a storage capacitor C_1 and thin film transistor TFT1 at the pixel. Each pixel acts as individual detector and has a top electrode (labelled A) deposited on the photoconductive layer for the application of bias. With the application of negative bias to electrode A and with the absorption of X-ray photons by the photoconductive layer, EHP pairs are generated in the photoconductor and they drift under the action of applied electric field. Dielectric layer at the top electrode traps the holes and electrons get accumulated in the storage capacitors C_1 and provide charge readout Q_1 which is proportional to the amount of incident X-ray radiation X_1 on the photoconductor over that pixel. The FET is turned ON every Δt seconds and the charge on the pixel is read out via an amplifier.

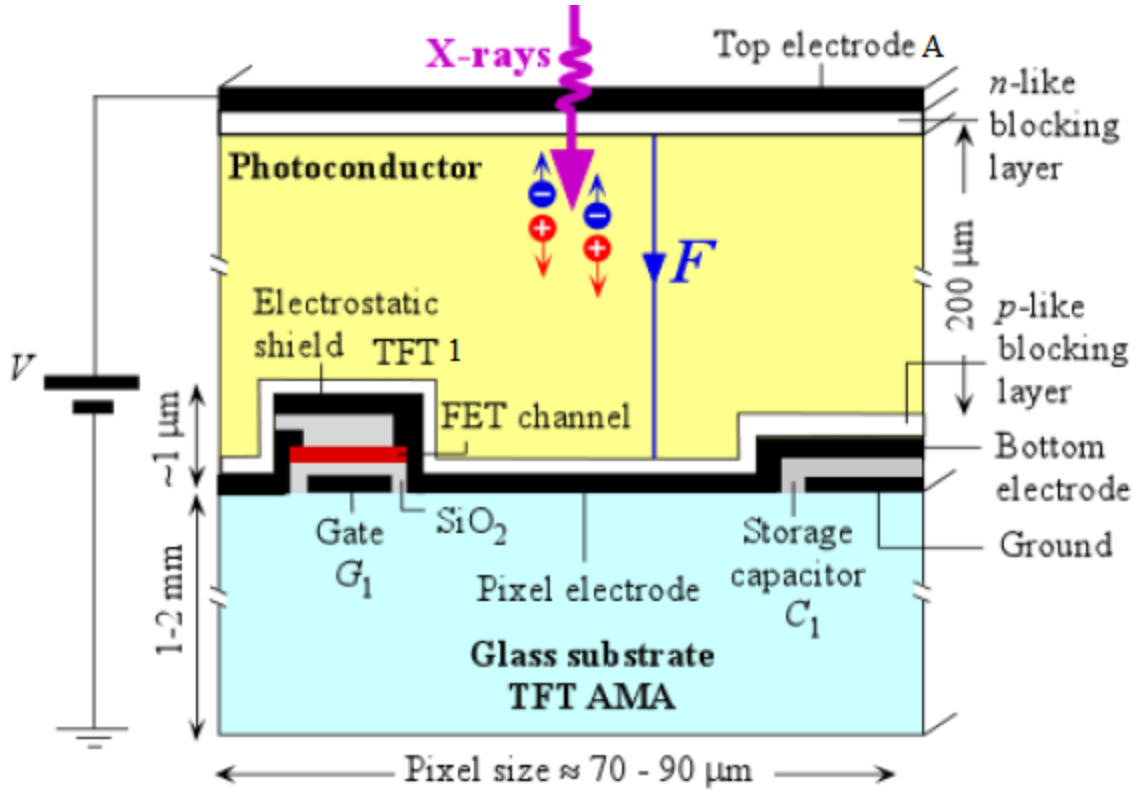

Figure 1.9: Simplified cross section of a pixel [10].

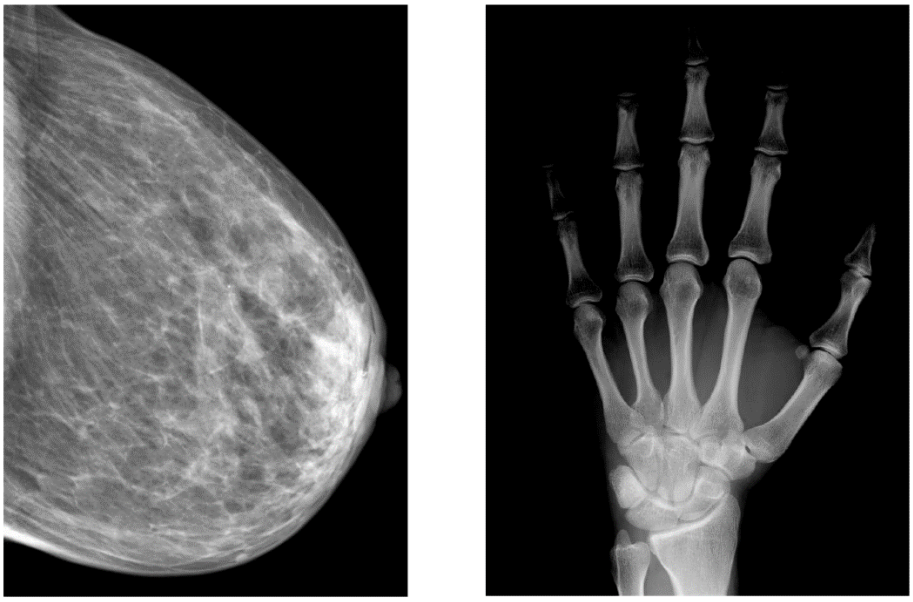

Figure 1.10: X-ray images representing a breast mammography and image of a hand taken by a-Se FPXI [10].

Figure 1.10 shows the examples of a breast mammogram and a hand taken by a-Se flat panel A-ray photoconductor. Rowlands and his Co-workers was the first to demonstrate the proto type of a-Se Flat panel X-ray based on using an active matrix readout panel. After their demonstration, more research has been performed on a-Se in understanding and characterizing the imaging properties of a-Se.

Commercial a-Se based flat panel X-ray detector can be seen in the Figure 1.11. The field of view is 24cm x 30 cm. These flat panel detectors have high detective quantum efficiency (DQE), high Modulation Transfer Function (MTF), high contrast, high dynamic range and high patient throughput [10].

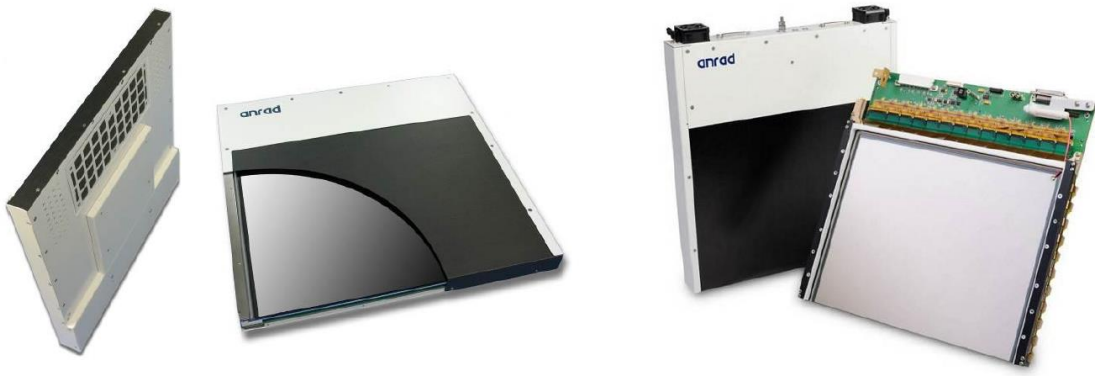

Figure 1.11: Commercial mammographic a-Se detectors FPXI AXS-2430 [10].

1.6 Flat Panel Photoconductive X-ray Detector

Dynamics of the flat panel X-ray photoconductor and the features affecting the performance of the detector are presented in this section. The performance of the flat panel detector is dependent upon the photoconductor thickness, charge transport properties and pixel size and the performance of the detector is measured by X-ray Sensitivity, Detective Quantum Efficiency (DQE) and Modulation Transfer Function (MTF). Both DQE and MTF depend on the spatial frequency

X-ray Sensitivity of a Photoconductive Detector

The X-ray sensitivity of the a-se flat panel detector relies on three distinct properties. First is that the X-ray attenuation in the photoconductor determined by a factor denoted A_Q, and is called the

quantum efficiency in medical physics. It measures the fraction of incident photons that are absorbed. The second property is the conversion of the absorbed energy to electron and hole pairs (EHPs). This quantity is also termed as ionization energy $W_{\pm}$. The third property is efficiency (η_{cc}) determined by the drifting of charge carriers and the final collection of photogenerated charge carriers. X-ray sensitivity S_x of the photoconductor is the charge collected per unit incident radiation per unit area. X-ray exposure irradiated on the photoconductor is measured in units of Roentgen. At one specific photon energy $E_{ph,}$ the X-ray sensitivity is given by [8]

$$S_x = \left(\frac{5.45 \times 10^{13} e}{(\alpha_{air}/\rho_{air})}\right) \times A_Q \times \left(\frac{(\alpha_{en}/\alpha)E_{ph}}{W_{\pm}}\right) \times \eta_{cc} \qquad 1.1$$

The first term is the incident number of photons per unit Roentgen in which α_{air} is the energy absorption coefficient and ρ_{air} is the density of air. Second term is the X-ray attenuation of the incident photons, third term is the electron hole pairs generated per absorbed radiation energy and the last term is the actual charges collected [10, 8]. x in Equation 1.1 is given by

$$x = \frac{\mu\tau F}{L}$$

L is the schubweg per unit thickness and $\Delta = \frac{\delta}{L}$ is the normalized attenuation depth of the photoconductor material.

X-ray Attenuation

The photoconductor used in medical imaging is required to absorb as much of the incident radiation as possible to reduce the patient exposure. The attenuated fraction $A_Q(E)$ of the incident photons with energy E in the beam is given by

$$A_Q(E) = \text{attenuated fraction} = [1 - \exp(-\alpha L)] \qquad 1.2$$

where $\alpha = \alpha(E, Z, d)$ linear attenuation coefficient of the photoconductor material. The linear attenuation coefficient α is a function of photon energy E, Z is the atomic number, d is the density of the photoconductor material with a thickness L. A_Q in medical physics is the quantum efficiency because it is the efficiency with which the photoconductor attenuates photons. The

attenuation depth δ is simply $1/\alpha$ and represents the thickness of photoconductor needed to attenuate the photons by 63%. Figure 1.12, shows the linear attenuation coefficient (α) and the attenuation depth (δ) as a function of photon energy E for various semiconductors. It can be seen that in the mammographic photon energy range, the attenuation depth of a-Se is in the 50 – 100 μm range so that a 200 μm a-Se photoconductive layer would attenuate more that 86% of incident radiation. On the other hand, it is apparent that in the chest radiology range the attenuation depth is poor; at 60 keV, δ is 1000 μm which means that we would need a-Se layers that is more than 2 mm thick to achieve 85% attenuation. This is one of the disadvantages of a-Se. While a practical a-Se detector of thickness 200 μm absorbs nearly all the incident radiation in the mammographic range, a practical a-Se photoconductor for chest radiology presents a number of challenging problems that must be overcome before a commercial detector can be marketed.

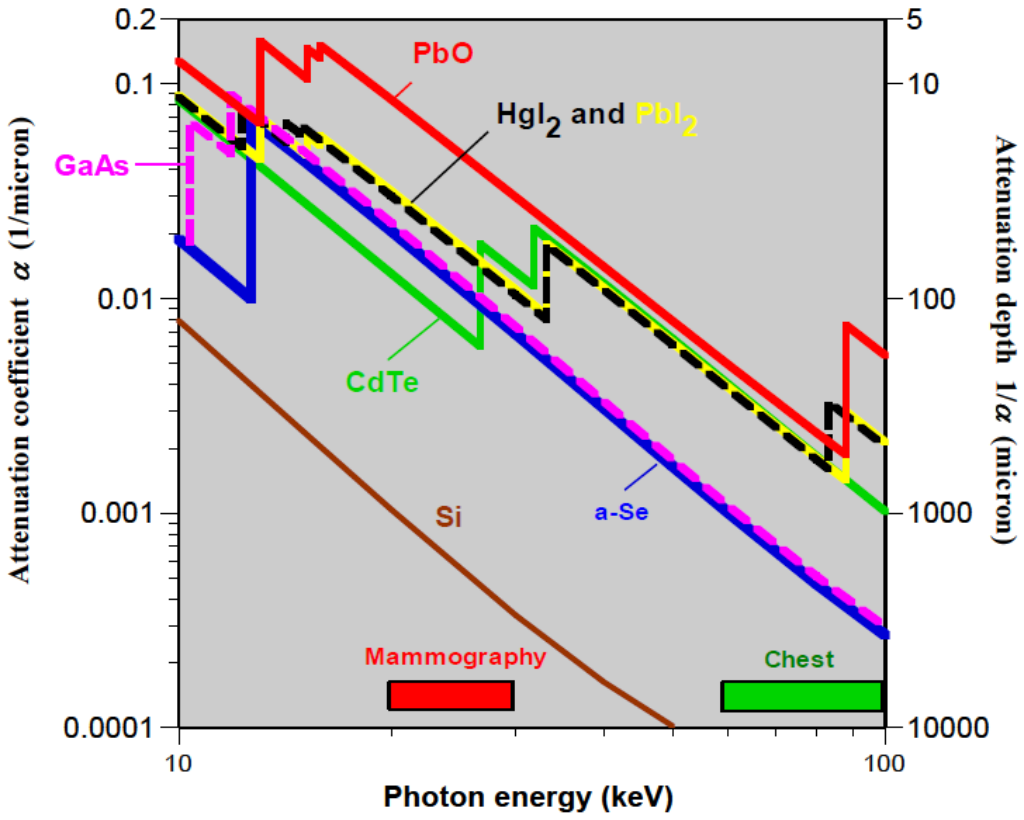

Figure 1.12: Linear attenuation coefficient vs photon energy for various semiconductors [10]

In order to minimize the dosage to a patient, and the detector should absorb all of the incident radiation. Ideal photoconductor's thickness L should be several times the attenuation depth δ of the material. It means the photoconductor thickness depends on the specific imaging application as mentioned above. The location of K-shell and L-shell attenuation are important. The K–edge of a –Se is at 12.7 Kev making its particularly useful for mammography.

In order to increase the fraction of absorbed photons (increase A_Q), the detector thickness L must be increased which is one of the requirements of an ideal flat panel detector, but there are three issues that limit the thickness L of the photoconductive layer. Firstly, when the detector thickness L is increased there is a high probability of trapping X-ray generated charge carriers during their drift to reach the bias electrodes. The second factor is, when the thickness of the material increases then there is a proportional increase in applied voltage to maintain the operating field, which is typically 10 V μm^{-1} in a-Se. Thirdly, very thick photoconductive layers are very difficult to fabricate without defects or without delamination or flaking off from the substrate; and practically it is not cost efficient.

Electron-Hole Pair Creation Energy: Ionization Energy

When X-ray radiation particle is incident on a photoconductive material an energetic photoelectron is ejected from one of the inner core subshells of the host atom, for example, from the K-shell. This electron has a very high kinetic energy and is often called the primary projectile electron. The energetic projectile photoelectron travels with high speeds and collides with other atoms and generate more electron and hole pairs along its path. The quantity of radiation energy absorbed by the photoconductive material to create a single electron and hole pair is called electron-hole pair creation energy or ionization energy $W_{\pm}$. The absorbed X-ray radiation energy ΔE generates an amount of charge ΔQ which is given by

$$\Delta Q = e\Delta E/W_{\pm} \qquad 1.3$$

In order to increase the sensitivity of the detector, the value of charge ΔQ should be as high as possible, which means that the EHP creation energy should as small as possible.

For most semiconductors, the ionization energy required to create a single electron-hole pair is dependent upon energy bandgap E_g which is given by Klein's rule [8]

$$W_{\pm} \approx 2.8\, E_g + E_{\text{phonon}} \qquad 1.4$$

where E_{phonon} is a phonon energy term (involving many phonons) and smaller than 0.5eV. In the case of crystalline semiconductors $W_{\pm}$ is independent on applied electric field it is well defined. For example, $W_{\pm}$ is well defined in high purity Si and Ge crystalline semiconductors and they are used to measure the energy of X-rays in spectrometers [8] However, in the case of a-Se, the ionization energy $W_{\pm}$ depends on the electric field and its value decreases with increasing field.

In the case of a stabilized a-Se, $W_{\pm}$ for a given energy E decreases with the electric field F and it has been approximated by

$$W_{\pm} \approx W_{\pm}^{0} + \frac{B}{F} \qquad 1.5$$

where B is a constant that depends on energy and it is a constant and $W_{\pm}^{0}$ is a saturated EHP creation energy [8]. Numerous experiments performed by Blevis suggested that $W_{\pm}$ is also controlled by the columnar recombination mechanism and at high fields this recombination also depends on $1/F$ [11].

Charge Transport and Collection efficiency

Charge collection efficiency is one among different factors that affect the sensitivity of the X-ray photoconductor and it is represented by $\eta_{\text{collection}}$ .The collection efficiency depends on the electron and hole schubwegs $\mu\tau F$ where μ is the drift mobility, τ is the carrier lifetime. The product of drift mobility (μ) and lifetime (τ) is called carrier range, the average distance drifted by a carrier per unit field before it is captured by a deep trap or it recombines with an opposite sign carrier Schubweg is the mean distance travelled by a carrier under a field F and is given by $\mu\tau F$. A trapped or recombined carrier is unavailable for conduction and collected by the electrodes.

Figure 1.13 shows the absorption of X-ray photons and photo generation of carriers in a photoconductor and this process decreases exponentially in a photoconductor from $x = 0$ to $x = L$.

The $x = 0$ is the positive radiation receiving electrode where more absorption of photons takes place and radiation energy decreases exponentially through the sample along x, thereby photo-generating electron hole pairs in the same exponential manner. At $x = 0$, the charge collection efficiency for holes is given by Equation 1.6 [8].

$$\eta_{\text{collection}}\,(\text{holes}) = \frac{\mu_h \tau_h F}{L-x}\left[1 - \exp\left(-\frac{L-x}{\mu_h \tau_h F}\right)\right] \qquad 1.6$$

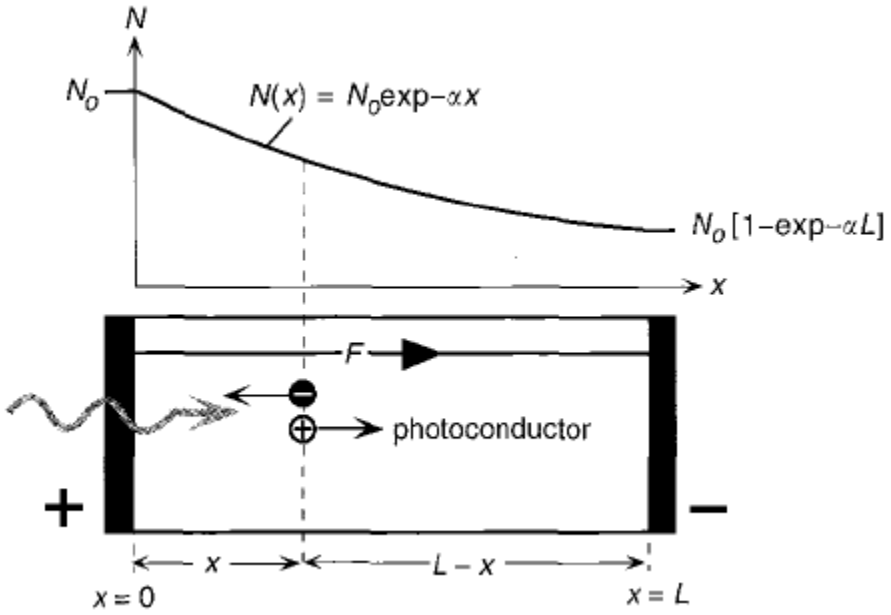

Figure 1.13: Photoconductor showing absorption of photons and photo generation of charge carriers. N is the number of photons incident on the photoconductor, Incident radiation decreases as it travels to the negative electrode [8].

L is the thickness of the detector, τ_h and μ_h is the lifetime and the drift mobility's for the hole. By considering the charge collected for photo generation at x and by integrating it across the detector thickness, the total collected charge can be calculated. The overall sensitivity of the photoconductor in the Figure 1.13 with the receiving electrode biased positively can be put into the normalized sensitivity S form

$$\frac{S}{S_x} = s(x_h, x_e, \Delta) = x_h\left[\left(1 - e^{-1/\Delta}\right) + \frac{1}{\frac{\Delta}{x_h} - 1}\left(e^{-1/x_h} - e^{-1/\Delta}\right)\right]$$

$$+x_e\left[\left(1 - e^{-1/\Delta}\right) - \frac{1}{\frac{\Delta}{x_e} + 1}\left(1 - e^{-1/\Delta - 1/x_e}\right)\right] = s_{\text{hole}}(x_h, \Delta) + s_{\text{electron}}(x_e, \Delta) \qquad 1.7$$

From Equation 1.7 it is understood that the sensitivity is controlled by x_h and x_e and as well as the normalized absorption depth $\Delta = \delta/L$ [8]

In the above equation, $x = \mu\tau F/L$ and the subscripts e and h are the charge transport parameters on x, μ and τ refers to electrons and holes respectively, e.g. $x_e = \mu_e\tau_e F/L$.

In the expression for Equation 1.7, S/S_x depends only on the charge transport and absorption effects without considering ionization energy term $W_{\pm}$. $W_{\pm}$ is excluded in the equation as it is a material property and can be taken as constant. S_x depends on the field, when all the incident radiation is absorbed and all the charges are collected, then the sensitivity is simply S_x (unity for x_e, $x_h >> 1$ and $\Delta << 1$) [12].

Ghosting

Ghosting changes the sensitivity of the amorphous selenium detector in consequent exposures as a result of X-ray exposure collected in previous cycles. When a region of the photo detector is irradiated, an exposure leaves that part of the detector with a lower sensitivity compared to the other region of the detector. A consequent exposure on a larger region of the same photo detector will have the image that holds the ghost of the first image. This ghost image is due to the reason that the sensitivity of the detector during the first exposure has reduced in that region [13, 14]. Carriers trapped in the bulk and recombination between the trapped and the drifting carriers is one of the major reason for ghosting [15]. Figure 1.14 illustrates the smaller region exposed to X-ray exposure and subsequent exposure in which larger area is exposed to X-rays. The shadow of the first image can be seen in the second image and the reduced sensitivity can be seen in the second image for the smaller region [16].

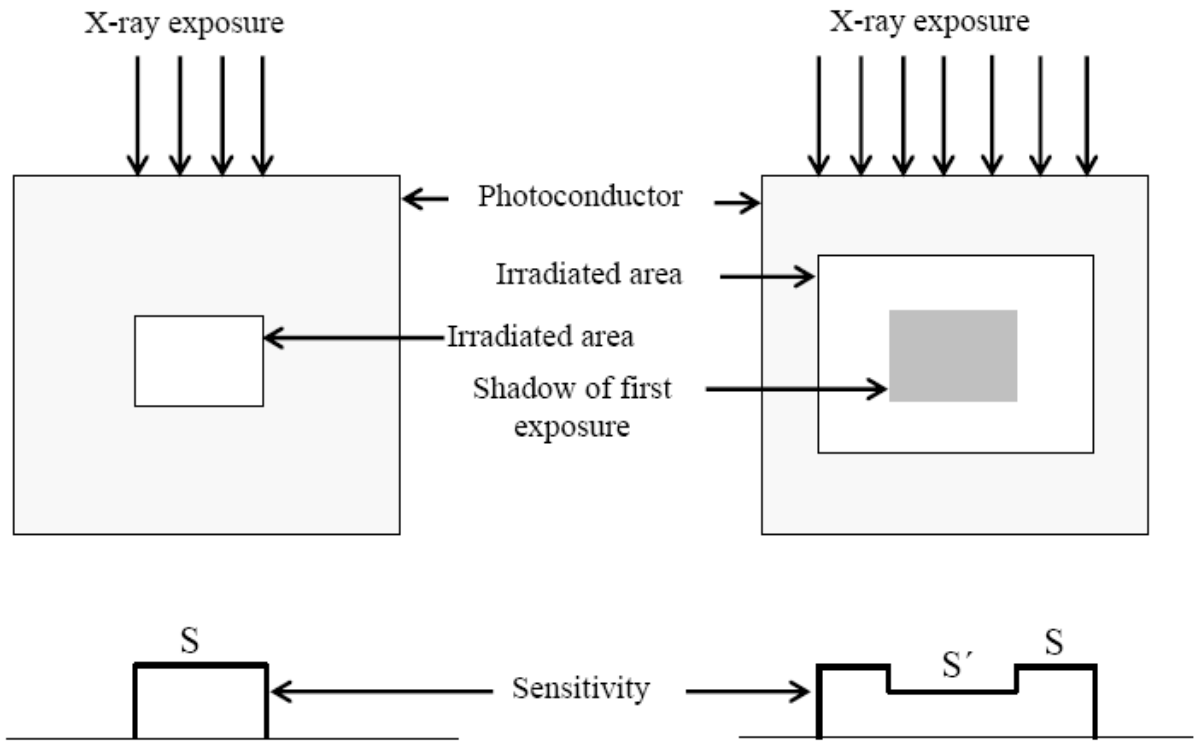

Figure 1.14: a) Photoconductor with a small area exposed (b) Subsequent exposure on the larger area of the photoconductor with the shadow of the first image seen (c) Sensitivity of the smaller area (d) Sensitivity of the exposed area of the photo detector with the reduced sensitivity on the smaller area due to the prior exposure [16].

1.7 Requirements of an Ideal Photoconductive Flat Panel Detector

The performance of an X-ray flat panel detector depends on the selection of the photoconductive semiconductor material. In order to identify and classify an ideal flat panel radiographic detector certain photoconductive material properties should be taken into consideration and they are listed as follows.

- The ideal flat panel radiographic detector should accept the whole image at one time with reduced patient dosage, and the read out should be immediate and electronic with ease to store and access.
- The image quality should be good which has high quantum efficiency for absorption of X-rays and should not degrade the image by excessive noise [17].

- The flat panel detector should have high X-ray Sensitivity. In order to have high X-ray sensitivity when an X-ray radiation is incident on a photoconductor the ionization energy required to create single electron-hole pair must be low as possible.
- The unwanted electric current known as dark current exhibited by the photoconductor due to the applied bias when there is no light incident on the conductor should be negligibly small.
- The longest carriers time should be shorter than the access time of the pixel
- The photoconductor material in the detector should not exhibit the property of bulk recombination of electrons and holes
- The deep trapping of electrons and holes should be negligible as possible
- The flat panel detector should exhibit the above mentioned properties and should not degrade with time and x-ray exposure [8].
- Although the direct digital detector was able to partially achieve the requirements of the ideal detector, it still has some limitations which have to be overcome.

1.8 Limitations of a-Se Flat Panel Detectors

In order to get good X-ray sensitivity, a-Se photoconductive layer has to be operated at very high electric fields. The photogeneration process in a-Se depends on the electric field and EHP creation energy, which is the ionization energy, $W_{\pm}$ is a function of applied electric field. Electron and hole traps can appear in a-Se as a result of fabrication or alloying and doping; and it can lead to ghosting and lagging if there is a significant amount of charge trapped in the layer.

Only when a high electric field is applied to a-Se, there is an acceptable level of X-ray sensitivity, negligible lagging and ghosting can be achieved. For this reason, the applied electric field to a-Se photoconductive layer is typically set to 10 V μm^{-1}. This large electric field will lead to high dark current, which is a disadvantage and many works have been done to reduce the dark current to an acceptable level. The dark current is an electric current due to the applied field across the photoconductive layer in the dark, and this is not due to the photogenerated carriers. Though the nature of the dark current is not fully understood, it is assumed that there are two factors such as thermal generation of charge carriers in the bulk and injection of charge careers from the contacts that contribute to the dark current. It is assumed that dark current by thermal

generation of charge careers in the bulk is considered to be negligible and injection of charge careers from the contacts leads to a significant amount of dark current and this can be minimized by adding blocking layers [18]. The current research is based on analyzing the dark current in various sample structures before and after exposure to establish whether x-ray exposure modifies the dark current.

1.9 Research Objectives

In order to understand the nature of dark current in the a-Se flat panel detectors and how it can be minimized, various experiments listed below were performed in a-Se monolayer and multilayer structures provided prepared by conventional vacuum deposition techniques

- Investigation of the dark current with no exposure in a-Se single and multi-layered structures
- Investigation of dark current with single x-ray exposure in a-Se single and multi-layered structures
- Investigation of dark current with multiple x-ray exposures in a-Se single and multi-layered structures.
- To determine whether x-ray exposure has an effect on the dark current or the effect can be neglected.

1.10 Thesis Outline

This chapter provides an outline of X-rays, its application in Medical Imaging, and further developments in X-ray imaging technology. Chapter 1 also talks about the different kinds of digital detectors, a comparative study between direct and indirect digital detectors, and flat panel direct digital detectors based on a-Se.

The remainder of the thesis is divided into 4 chapters. Chapter 2 provides an overview of Amorphous Selenium and its properties of an X-ray photoconductor such as dark current, x-ray sensitivity, ghosting, trapping, recombination, effect of doping and alloying.

Chapter 3 provides information about the creation of a-Se sample structures, and the experimental set up used in measuring the dark current for different sample structures.

Chapter 4 reports the experimental work performed and discusses the results in all the four sample structures. Results on the single and multi-layered structures show the dark current as a function of time without exposure, with single exposure and with multiple exposures.

Chapters 5 present the conclusion drawn from the work performed and provide suggestions for future work.

CHAPTER 2. BACKGROUND AND THEORY

2.1 Introduction

During 1960's and 1970's amorphous selenium (a-Se) and its alloys were thoroughly researched because of their significance in commercial xerography. In the last fifteen years, there has been much research on a-Se for its use as a photoconductor in flat panel X-ray imagers in medical imaging. It has been found that a-Se can be deposited as a uniform layer to produce large area photodetectors which is used in chest radiography. The thin photoconductive layer of amorphous selenium converts the incident X-ray photons to electric charges which are collected and read out as an image. Dark current that influences the Detective Quantum Efficiency (DQE) is one of the most fundamental characteristics of a-Se, and will be discussed in this chapter. The electrical and optical properties of a-Se will also be discussed in this section.

Progress in a-Se x-ray detectors depends on a thorough understanding of the electrical and optical properties; and how these depend on the bonding configurations in the structure. A-Se photoconductor layer that is actually used in a practical detector is called stabilized a-Se because of its alloying and doping components. Pure a-Se doped with Cl in 10-20 ppm range and alloyed with 0.2-0.5% of As is stabilized a-Se and is simply denoted as a-Se. In mammographic imaging, X-ray image detector must be large enough to capture imaging area that is roughly 30 cm × 30 cm. Therefore, the X-ray image detector should maintain the photoconductor properties over a large area, and this is one of the most important requirements in imaging. Considering this requirement, a-Se is highly suited compared to other X- ray sensitive crystalline semiconductors which are difficult to grow in large areas. Polycrystalline semiconductors can be prepared over a large area but their dark current level for the required sensitivity so far has been higher than that for a-Se [10]

A-Se has a well-established technology as an electrophotographic photoreceptor and it can be easily coated as thick films 100-1000μm onto a suitable substrate by a conventional vacuum deposition technique [11]. The flat panel x-ray image detectors based on a-Se have shown high spatial resolution and good sensitivity; and have been commercialized for use in mammography.

2.2 Structure of Amorphous Semiconductors

It is important to understand the bonding and atomic structure in semiconductors as it is the main feature which distinguishes amorphous materials from crystalline materials. When discussing the theory of crystalline semiconductors, the periodicity of atomic structure is considered to be the core as it has a significant importance in semiconductors [19]. A period potential energy for the electron allows the Schrodinger equation to be solved (often numerically) which leads to the electron wave functions, density of states and *E* vs. k diagrams. A crystalline solid is basically a three dimensional periodic network of atoms interconnected by bonds. A characteristic property of the crystal structure is its degree of symmetry and periodicity. The crystalline structure has highly ordered arrangement of atoms which is represented in Figure 2.1a. The bond length and relative bond angle in the crystalline network is same throughout the volume of the solid. Every atom in the crystalline network has the same coordination number as the number of neighbors to the atom is the same. This order exists throughout the solid at highly ordered degree so that the equilibrium position of any atom can be identified from any position in the network. This type of order is classified as long – range order resulting from the strict adherence to a well-defined bond length and this kind of network exists through entire volume of the solid.

The lines between the atoms in the Figure 2.1 represent the equilibrium bond lengths between periodically positioned points (atoms). The atoms oscillate about their equilibrium positions so the bond lengths are stretched and compressed but these oscillations are very small compared to the equilibrium bond length. In an amorphous semiconductor network presented in Figure 2.1b, the bond angles and bond lengths between the atoms are not same from one atoms to another. There seem to be a variation in the bond lengths and bond angles which destroy the spatial periodicity of the network after a few atomic distances The coordination number in an amorphous semiconductor is not same throughout the solid thereby resulting in a incorrect coordination number which is classified as a defect. The expected or normal coordination number is known as normal structural bonding (NSB). Typical elementary defects in an amorphous structure is of two types, Over –coordinated defects represented as (O) and under – coordinated defects represented as (U) in the Figure 2.1b [20]. However the position of an atom cannot be used to define a defect as it is not a practical reference point [19]. Amorphous and crystalline semiconductors are similar in terms of short range order. Short range order means that we can define the nearest neighbors of an average atom not its further neighbors. Similarity in

the short range order causes the amorphous and crystalline semiconductors to have similar electrical and optical properties.

The bonding arrangements for crystalline and amorphous semiconductors are represented in two dimensions in the Figure 2.1 a and b.

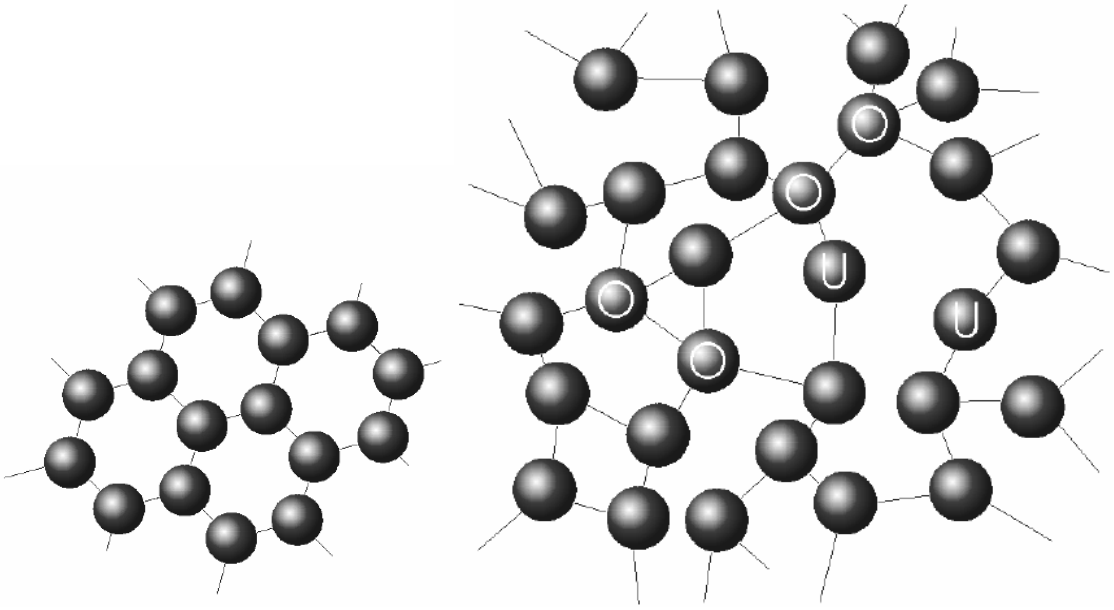

(a) (b)

Figure 2.1: Representation of 2 dimensional three-fold coordinated atomic structure (a): a crystalline semiconductor, (b) amorphous semiconductor. Over – coordinated (O) and Under – coordinated defects (U) are shown for the amorphous semiconductor structure After Fogal,[21]

2.3 Band Model of Amorphous Semiconductors

Bandgap plays a pivotal role in the properties of semiconductor and much experimental studies have been dedicated to understanding the nature of bandgap in the case of amorphous semiconductors [22]. The bandgap model and the density of states concept can be explained by the behavior of electrons in a solid in terms of quantum mechanics. When the atoms are brought in close proximity to form a solid, each electron in the atom will have an energy state and the bulk solid is said to have continuous electron energy states that can be described by a density of states (DOS). At a given energy E, density of states function for electron states can be represented by $g(E)$. The dependence of $g(E)$ on the electron energy E represents the DOS distribution, which is an important attribute for an amorphous semiconductor.

The behavior of electrons in quantum mechanics theory develops the band model in crystalline semiconductors. The energy band diagram of a crystalline semiconductor is represented in Figure 2.2. The Energy band comprises of two bands and these two bands are separated by a forbidden energy gap termed as energy bandgap E_g in which there are no allowed electron energy levels. The bonding band which is completely occupied by electrons is termed as valence band by virtue of the valence electrons it contains. It is the lower band in the Figure 2.2a, which is filled with electrons bonded covalently represented as E_v in the diagram.

The upper band is completely unoccupied by electrons (Figure 2.2). At temperatures above zero, the atoms vibrate and when electrons acquire sufficient energy from lattice vibrations, it can leave the valence band (VB) by surpassing the bandgap and enter the conduction band (CB) contributing to the conductivity of the semiconductor. As there is conduction in the upper band, it is termed as conduction band or anti-bonding band CB [23]. The electronic structure of amorphous semiconductor is more difficult to explain due to the lack of long range topological order (periodicity). However, the bandgap and density of states concepts do not depend on the periodicity of the structure and continue to be useful. Most importantly, the electron wave functions fall into two categories: (a) extended wave functions (b) localized wave functions. An important characteristic of amorphous semiconductors is that an electron can be spatially localized, that is the wave function amplitude decays exponentially (somewhat similar and there is a critical energy E_c that separates extended and localized states in the density of states distribution as shown in Figure 2.2(b). The origin of these localized states is the spatial variations in the bond lengths and angles that lead to random fluctuations in the potential energy of the electron through the solid. The electron can become localized in regions where the potential energy fluctuation is significant and traps the electron, similar to the trapping of an electron in a finite potential energy well. However, the amorphous semiconductor still has a bandgap as in the case of crystalline semiconductors that separates extended and localized states, and it is due to the short range order in the atomic structure. The density of states in the crystalline and amorphous semiconductors can be seen in the Figure 2.2[24]. The localized states below but near E_c, and those above but near E_v, are called tail states. In general, all states between E_v and E_c are called localized states and their density of states is called the *localized density of states* (LDOS)

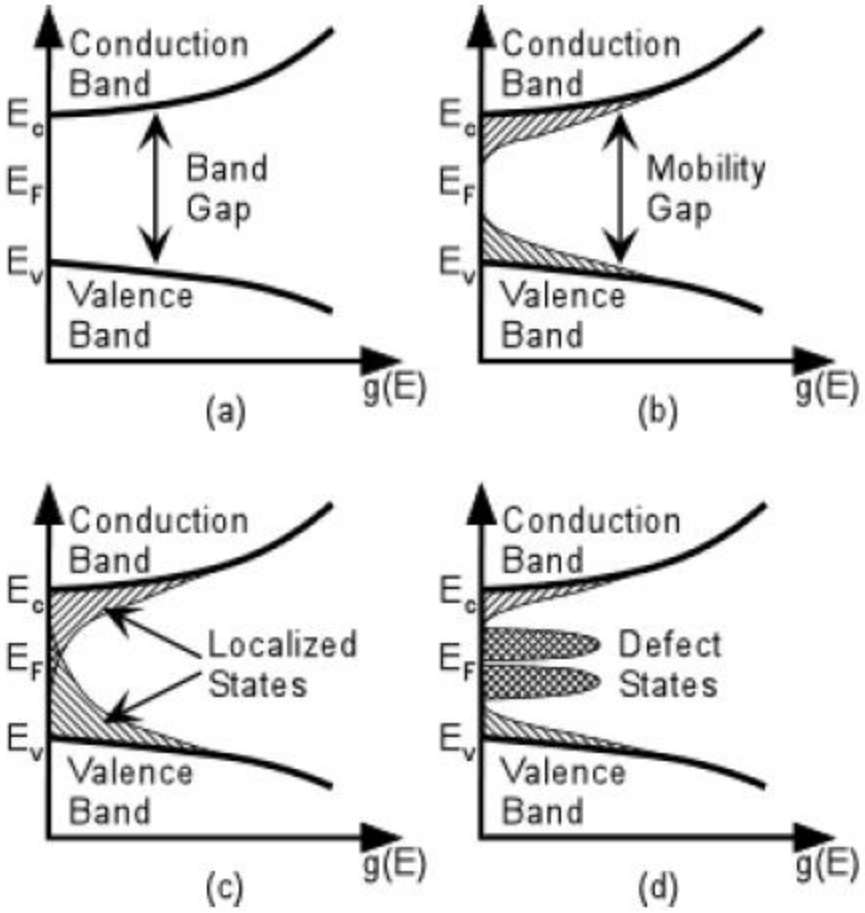

Figure 2.2: a) Energy band diagram of crystalline semiconductor, the valence band and conduction band are separated by a forbidden energy bandgap E_g.b) Density of states model proposed by Mott for amorphous semiconductor showing the localized states in the bandgap region. c) The CFO model showing the localized states that is continuous in the bandgap region. d) Deep localized states due to defects in the forbidden gap proposed by Marshall and Owen [24].

N.F. Mott first proposed the band model for amorphous semiconductors in the 1960s based on the following two features of crystalline semiconductors

- The extended Bloch wave functions describe that the individual electrons inside the crystal lattice possess long range order in amplitude and phase
- The well-defined energy gap known as forbidden energy gap separates the valence and conduction bands of electron energies

Mott assumed that all amorphous semiconductors have common characteristics i.e. he suggested that Bloch wave functions for electrons has short range order in their phases and long range order in their amplitudes resulting in the electrons localized states encroaching the bandgap[25]. Mott's model was centered on the random network developed by P.W. Anderson in 1958. In this model, it is described that the existence of electronic states are defined by energy and density. When the randomness of the network increases, the density and energy spread of the localized states will also increase. [26].

The proposed density of states model by N.F. Mott is represented in Figure 2.2b. The conduction band (E_c) and valence band (E_v) separated by bandgap can be seen in the Figure 2.2b. The disordered network in the solid introduces localized tail states at the beginning of the band edges E_c and E_v and tails off into the forbidden energy gap. Electrons in the localized tail states and extended band states move with different motilities. Electron transport within the extended band states is determined by the electron's effective mass and scattering from potential fluctuations and/or thermal vibrations of the lattice for energetic electrons. The electron transport within the localized tails states is controlled by thermally activated tunneling between the localized states. This difference in electron mobility between the localized tail states and extended band states gives rise to the well-known mobility gap in amorphous semiconductors which is similar to the concept of bandgap in crystalline semiconductors [27].

Figure 2.2c represents the Cohen, Fritzsche and Ovshinski (CFO) model for amorphous semiconductors showing the localized states that is continuous through the bandgap. This model is an extension of the Mott model by Cohen, Fritzsche and Ovshinski. In the CFO model , the localized tail states overlap with the Fermi level and it was claimed that the classical metallic conduction when there are states around E_F is not as expected in this case because these gap states are very highly localized in space [28].

Figure 2.2d represents the Marshal and Owen model where local defect states are predicted to be very high in concentration. There are two defect states appearing above and below the Fermi level between the two energy bands. These two defect states act as donor and acceptor like states and they significantly influence the electrical and optical properties of the amorphous materials even in smaller proportions [29].

2.4 Atomic Structure of Amorphous Selenium

Selenium belongs to the chalcogenides group of elements in group sixteen of the periodic table and the structure of selenium has been subject of discussion for many years. The atomic number of Selenium is Z=34 and it is classified as a non-metal. It was discovered by Jons Berzelius in 1817 and the word Selenium originated from the Greek word Selênê. The selenium atom has twenty-eight inner core electrons 6 valence shell electrons. Two of the valence shell electrons are paired in one of the *p*-orbitals, which becomes a lone-pair (LP). The other two *p*-orbitals each have one electron, that is, Se has two half-filled *p*-orbitals which are available for bonding with other atoms to form a solid. This results in both crystalline and amorphous phases, the selenium atom has two-fold coordination with a bond angle of 105°[30].

According to the literature (https://en.wikipedia.org/wiki/Selenium accessed on 02-08-2016) Selenium exists in various allotropes in the condensed state such as hexagonal (or trigonal), α and β monoclinic amorphous and vitreous phases but there are no grounds to differentiate between a vitreous form and an amorphous form of selenium which are both non-crystalline forms [31].

2.5 Crystalline Selenium

Crystalline form of selenium can be classified into hexagonal selenium, written as γ-Se (Se_n) and α-, β-monoclinic selenium, written as α- or β- Se_8 . While monoclinic Se has Se_8 rings, γ-Se has Se_n chains and for that reason amorphous selenium is said to have a mixture of rings and chain members. Amorphous selenium phase has been proposed to consist of selenium chain and rings structures mixed together [31]. Selenium has a twofold coordinated chain structure and the dihedral angle ϕ is constant but varies in sign randomly [32]. At normal pressure crystalline hexagonal selenium Se_n has a melting temperature of 217°C, α-monoclinic Se_8 has a T_m of 144°C and β-monoclinic has a T_m of 100°C [31]

Figure 2.3 represents the position of atoms, bond angle θ, and bond length r for the crystalline phase of Selenium. The position of atoms is fixed by symmetry and the magnitude of ϕ is a function of bond angle θ and bond length r. The monoclinic selenium is said to have CIS configuration in the arrangement of four atoms bonded in a sequential order to form a Se_8 molecule. The unit cell contains four Se_8 molecules and has the following parameters α= 905.4 pm, β = 908.3 pm and c =1160 pm. The valence angle is θ = 105.9° and dihedral angle ϕ =

101.0° [31]. Dihedral angle is defined as the angle between two adjacent bonding planes. Dihedral angle between 4 atoms is illustrated in the Figure 2.3. θ is the angle formed by the atom between two different atoms. In the crystalline form the position of Selenium atoms are fixed and the bond angle θ and bond length 'r' are fixed and therefore the dihedral angle ϕ is constrained as a function of bond length and angle [32].

In trigonal form of Selenium spiral patch of three atoms are formed by the dihedral angle that rotates along a moving chain. When there is a change in the sign of the dihedral angle ϕ like $+-+-+-$ then the regions are said to be ring like and if the sequence is like $+++ or \ ---$ it is termed as chain like structures [32]. The unit cell of the trigonal lattice is said to have the following parameters such as a = 436.8 pm, c= 495.8 pm. θ is the valency angle which is equal to 103.1 degrees.

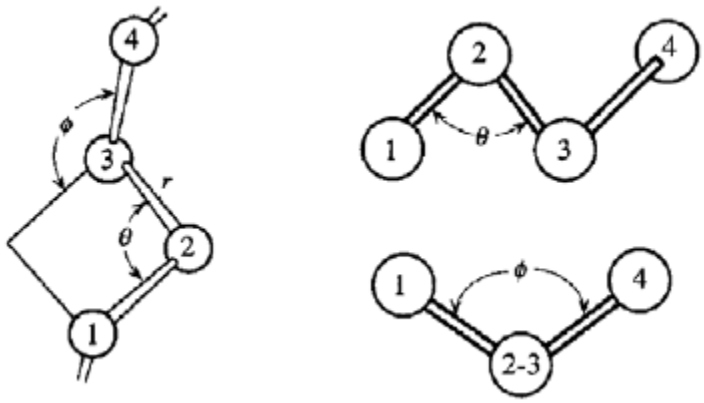

Figure 2.3: Definition of dihedral angle ϕ and Selenium chain molecule formation [32].

Table 2.1: Summary of various allotropic forms of Selenium and their properties and parameters [31].

No.	Name	Molecular composition	The bond length Å	The bond angle, deg.	The coordination number K_1	Unit cell constants			The transformation temperature T, °C	Density, $g.cm^{-3}$
						a	b	c		
						Å	Å	Å		
Crystalline										
1.	Trigonal	Spiral chains Se_n	2.37	103.1	2	4.366	-	4.954	Melting 217-221	4.819 [24]
2.	α-monoclinic	Rings Se_8	2.32	105.9	2	9.054	9.083	11.601	Transformation into trigonal 140-160	4.390 [24]
3.	β-monoclinic	Rings Se_8	2.34	105.5	2	12.85	8.07	9.31	Transformation into trigonal 140-180	
4.	α-cubic	-	2.97	-	6	2.970	-	-	-	
5.	β-cubic	-	2.48	-	4	5.755	-	-	-	
6.	Rhombohedric	Rings Se_6	2.35	101.1	-	11.362	-	4.429	Transformation into trigonal 120-135	4.710 [27]
7.	Ortho-rhombic	-	-	-	-	26.32	6.88	4.34	Transformation into trigonal 105	
Non-crystalline										
8.	Red amorphous	Rings	2.33		~2.4	-	-	-	$\approx T_{room}$	4.270 [24]
9.	Black amorphous	-	-		-	-	-	-		
10.	Vitreous	Chains and rings	2.33 2.46	105	2-2.2	-	-	-	Softening 30	4.280 [24]
11.	Melt									4.010 [24]

The characteristics and some of the forms of allotropic Selenium are summarized in Table 2.1. The trigonal Selenium in Figure 2.4a is said to be thermodynamically stable out of the other allotropic forms. Temperature plays a major role in the transformation of metastable selenium, as the temperature raises the monoclinic Se transforms to hexagonal Se after heating at 70°C for duration of 630 min. At a temperature higher than 105°C rhombohedric Se transforms to hexagonal Se and α-monoclinic Se. At 144°C α-monoclinic Selenium represented in Figure 2.4c melts and immediately transforms to trigonal Selenium which is thermodynamically stable. B-monoclinic Se represented in Figure 2.4b transforms to trigonal selenium at temperatures between 140°C to 180°C. These transformations of Selenium are irreversible and the modification of several allotropic forms can be seen in the Figure 2.4.

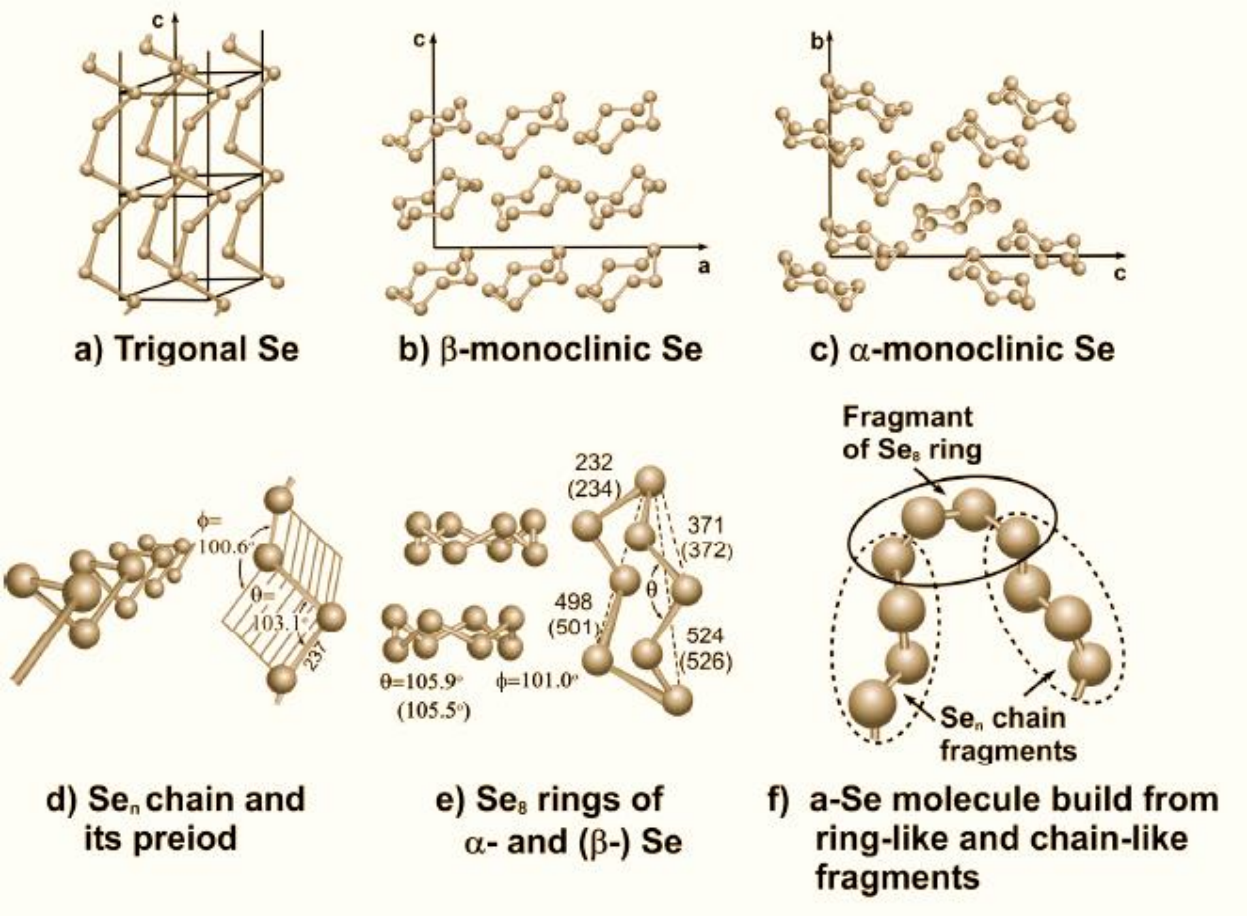

Figure 2.4: Illustration of selenium crystalline modifications a) trigonal selenium with shortest Se-Se distance in the Selenium chain is 237.3 pm and the distance between the Se atom and the fourth second atom neighbor in the three selenium spiral is 342.6 pm. b) β-monoclinic Selenium with θ = 105.5 °and r = 324 pm. C) α- monoclinic Selenium with θ = 105.9° and r= 232 pm. d) the trans-configuration of Se chains. e) "Crown" structure of Se_8 molecules in monoclinic α and β modifications. f) a-Se chains in random chain model build from ring and chain like fragments (From [18, 31])

The trans-configuration of Se_n chain can be seen in the Figure 2.4d with its valency angle θ = 103.1° and dihedral angle ϕ = 100.6°. Figure 2.4e represents the crown structure of Se_8 molecules in monoclinic α and β modifications where θ = 105.9° and dihedral angle ϕ = 101.0°. Representation of random Selenium chain model is given in Figure 2.4f that is characterized by +++-+-+---. This chain model which has a local molecular order and it is used to describe the vibrational spectra of stabilized amorphous selenium in the Raman scattering and infrared (IR) absorption [33, 20].

2.6 Amorphous Selenium

The structure of a-Se has been extensively debated in the literature and there is no well-defined consensus. It is generally accepted that the structure consists of fragments of Se_n chains and Se_8 rings as shown in Figure 2.4f. The exact ratio of Se_n-chain and Se_8 ring fragments is believed to play an important role in determining the properties of a-Se [34]. All the amorphous chalcogenide semiconductors are known to have defects with some of the atoms having over coordinated and some has under coordinated. Various bonding configurations for Se atom are represented in Figure 2.5 which is altered from [35]. The two fold coordinated state Se_2^0 is termed as lowest energy bonding state. It is involved in the normal bonding structure of the solid. Se_3^0 , the trigonally coordinated atom is a neutral defect. It has 3 valence electrons in the bonding state and 1 electron in the anti-bonding state. Se_1^0 , denotes the single coordinated bonding state and it is a neutral defect state. Se_1^0 , have 1 electron in the bonding state and 3 electrons in the non-bonding state. Anti-bonding state is represented as AB, non-bonding state is represented as NB, and bonding state is represented as B in the Figure 2.5a.

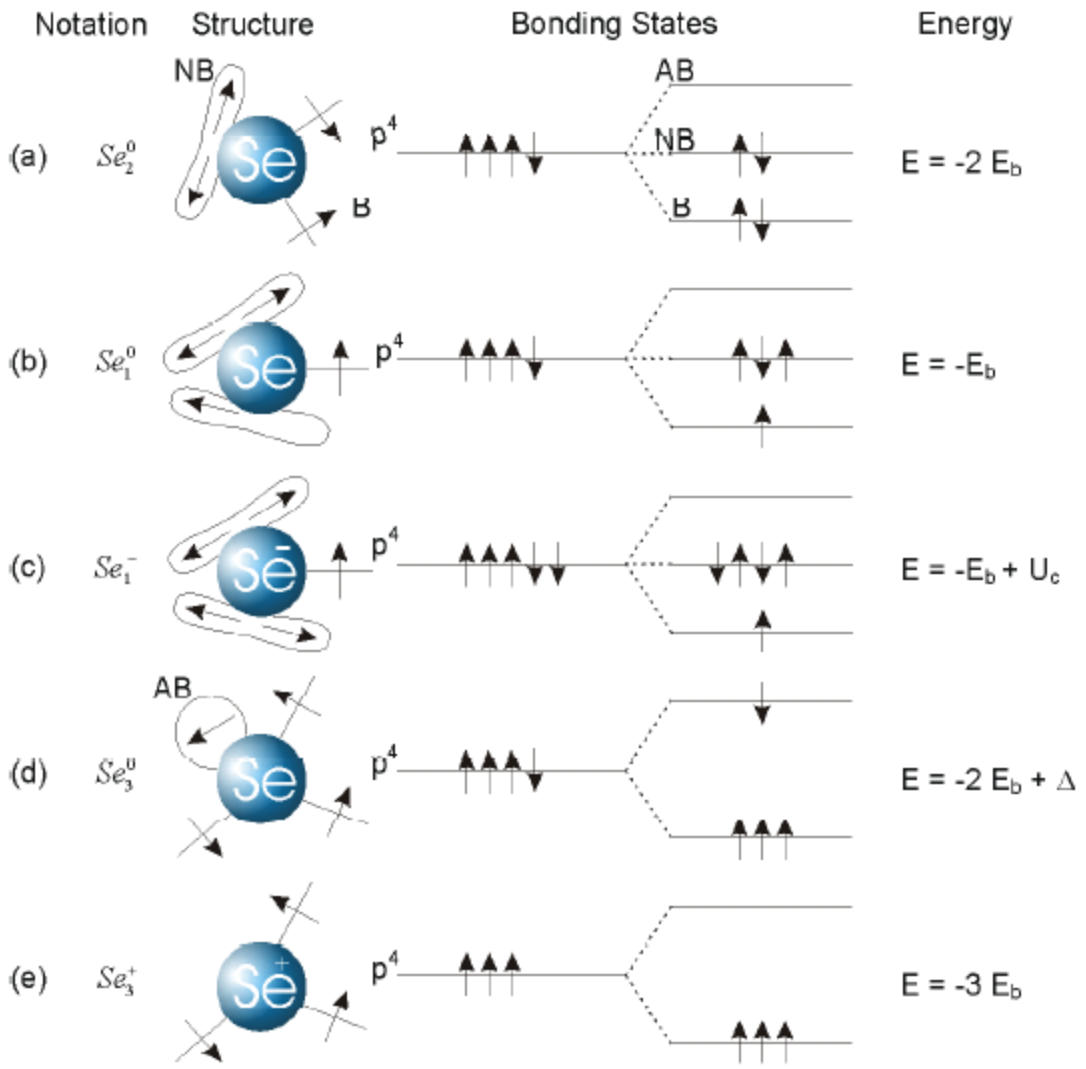

Figure 2.5: Representation of simple bonding configuration structure and energy for Selenium atom. Bonding orbitals are represented by straight line. Lobes are termed as lone-pair with zero energy, circles are antibonding orbitals. Adapted from[35].

Amorphous Selenium has various bonding arrangements; the absence of ESR signal confirms that there are no dangling bonds in the a-Se structure. Se_1^- and Se_3^+ in Figure 2.5c and Figure 2.5e are valence alternation pair defects termed as VAP defects. The concentration of VAP defects in a-Se has been estimated to be approximately 10^{18} cm^{-3} which is of a large concentration can be seen in Figure 2.5c and Figure 2.5e. The formation of Se_1^- and Se_3^+ defects are more favorable than the formation of Se_1^0 and Se_3^0.These defects exists because of the diamagnetic pair of charged under- coordinated and over coordinated VAP centers is

thermodynamically more stable than neutral defects. An intimate valence alternating pair (IVAP) defect is created when a dangling bond Se_1^0 approaches the lone pair on the normally coordinated atom Se_2^0. The schematic representation of the IVAP defect is given in Figure 2.6

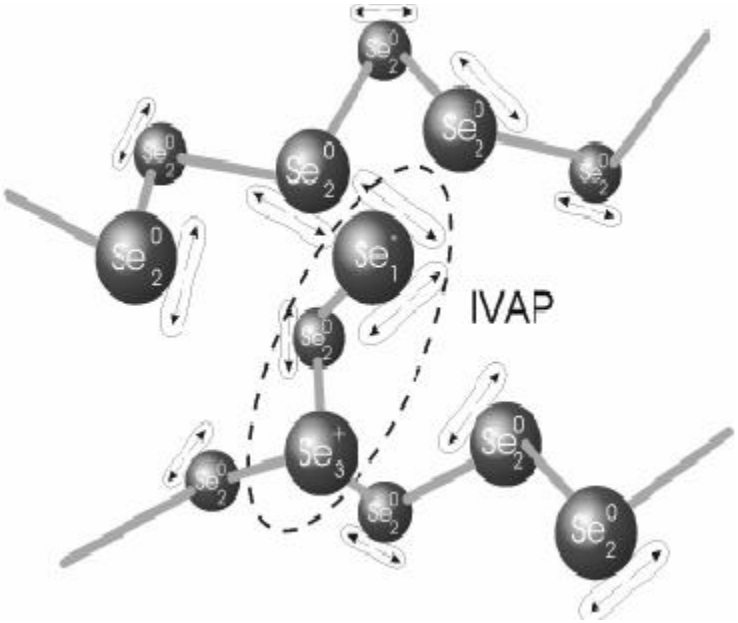

Figure 2.6: Amorphous Selenium with IVAP defect. After Fogal[20]

The formation of a VAP defect is given in Equation 2.1. The reaction in (Equation 2.1) is exothermic because the lone pair of electrons has joined the dative bonding scheme of a-Se chain.

$$Se_1^0 + Se_2^0 \rightarrow Se_1^- + Se_3^+ \qquad 2.1$$

These VAP- and IVAP- type defects can explain the photo electric properties of a-Se material. The explanation of these properties are discussed in detail in the literature [36, 37] .Many significant predictions has been made on the behavior of chalcogenide glasses due to the existence of defects at a structure level. For example, these defect states can explain the linear dependent relationship between photoconductivity and light intensity [38].

2.7 Properties of Amorphous Selenium

Density of states in the energy band model in an amorphous semiconductor is a very important tool in understanding the material's electrical properties. Electrical properties of crystalline selenium do not necessarily apply to amorphous selenium due to the absence of long-range order. In this section, the properties of a-Se will be discussed in relation to the density of states.

Density of States of Amorphous Selenium

Based on the bond orbital model, the energy band of a-Se has paired electrons in overlapping 4*p*-orbitals which forms the covalent bond, and leads to a σ-type band below the valence band edge. Lone pair 4p orbitals constitute the top of the valance band. As already discussed in an earlier section, the conduction band consists of antibonding states σ^*. The nature of valence and conduction band are the same in all phases of selenium as confirmed by photoemission experiments [39, 40]. The random variation in the dihedral angle leads to localized tail states above the valence band.

One of the most successful model of the DOS for a-Se was put forth by Abkowitz in 1988 [41]. This model was modification of the Owen-Marshall model for As2Se3 to be applicable to a-Se. The proposed Abkowitz model is represented in Figure 2.7. The shallow electron and hole traps are located at 0.35eV below E_c and 0.25eV and above E_v which are derived from the analysis in Time of Flight (TOF) transient photoconductivity measurements. The deep traps are present above and below the Fermi level at 1.22eV and 0.87 eV and have been determined from xerographic measurements such as cycled up first residual and the dark decays of the saturated residual potential. The mobility gap for amorphous selenium is set to 2.22eV as represented in the Figure 2.7. However, it is important to mention that the optical measurements yield an optical gap of about 2.0 eV, which is somewhat smaller than the mobility gap [42].

When the release time (τ_r) of the trapped carrier is greater than the observation time of the experiment then the trap is referred to as a deep trap. The shallow traps are those capture centers with which carriers interact multiple times over the observation time scale through the capture and release processes. Put differently, carriers are in quasi-thermal equilibrium with the shallow traps so there is no net rate of capture or release from the shallow traps. The shallow traps control the carrier drift mobility, which becomes reduced from its band transport value. Suppose that in the presence of shallow traps, we assign an effective carrier mobility μ to the drift of the

carriers. If the mobility of carriers in the band among the extended states, the so-called microscopic mobility, is μ_0, then we can relate the effective and microscopic mobility's by the Equation 2.2

$$\mu = \theta\mu_0 = \frac{p_{\text{free}}}{p_{\text{free}} + p_{\text{trapped}}}\mu_0 \qquad 2.2$$

Where, θ is the mobility reduction factor, p_{free} is the concentration of carriers in the trapped band and $\text{p}_{\text{trapped}}$ is the concentration of carriers in the shallow traps. In equilibrium, these carrier concentrations are constant.

The effective drift mobility of holes is given by the following thermally activated relationship [43]

$$\mu = \mu_0 \left[1 + \frac{N_t}{N_v}\exp\left(\frac{E_t}{kT}\right)\right]^{-1} \approx \mu_0 \frac{N_v}{N_t}\exp\left(-\frac{E_t}{kT}\right), \qquad 2.3$$

where N_t is the shallow trap concentration, N_v is the density of states at the valence band edge E_v and E_t is the difference in energy between the shallow trap energy and E_v.. The value of μ_0 for holes is of the order of 0.3–0.4 cm^2/Vs at room temperature.

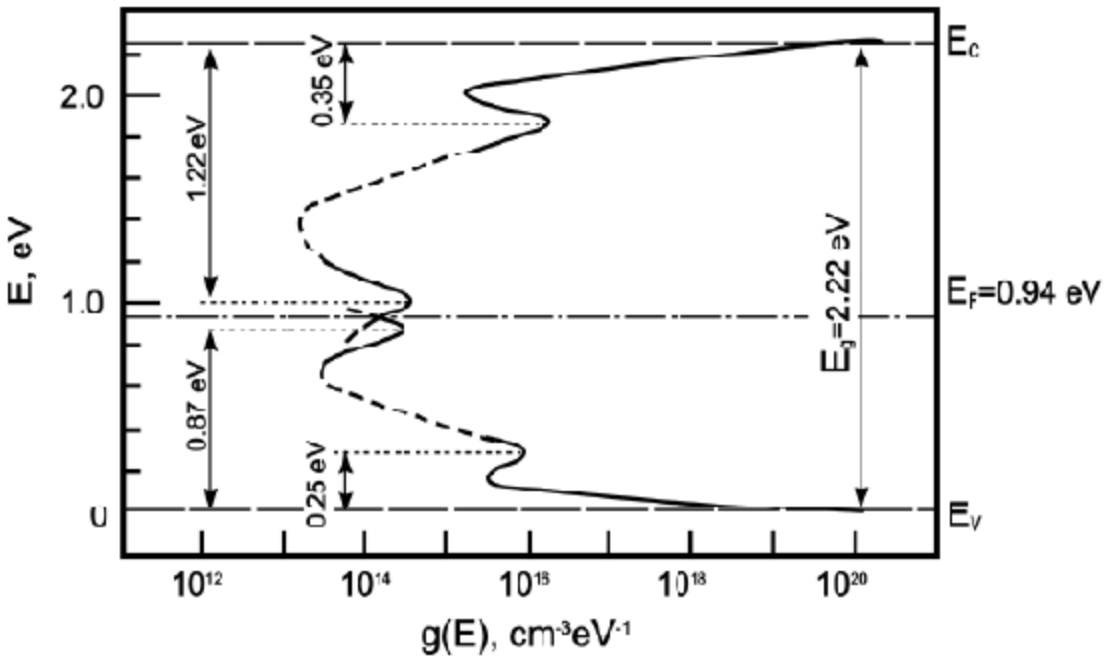

Figure 2.7: Density of states for a-Se proposed by Abkowitz [41]. Shallow traps exist at 0.25 eV above valence band E_v and 0.35 eV below conduction band E_c. Deep trap exists above the Fermi level at 1.22 eV and 0.87 eV below the Fermi level.

The deep trap states were examined by the photoinduced discharge measurements and cycled- up xerographic voltage residual measurements. The shallow electron and hole trap distributions show a background of exponential type decay with two peaks as shown in the Figure 2.7 from the transport band edges and their values were derived from transient photoconductivity measurements using micro-wave strip line techniques.

An alternative model of density of states for a-Se has been also put forth by Adriaenssens's group [44]. From the analysis of post-transit photocurrent experiments, the peak density of hole traps seem to occur at 0.4 eV above E_v and electron traps 0.52 eV below E_c. This representation can be seen in the Figure 2.8.

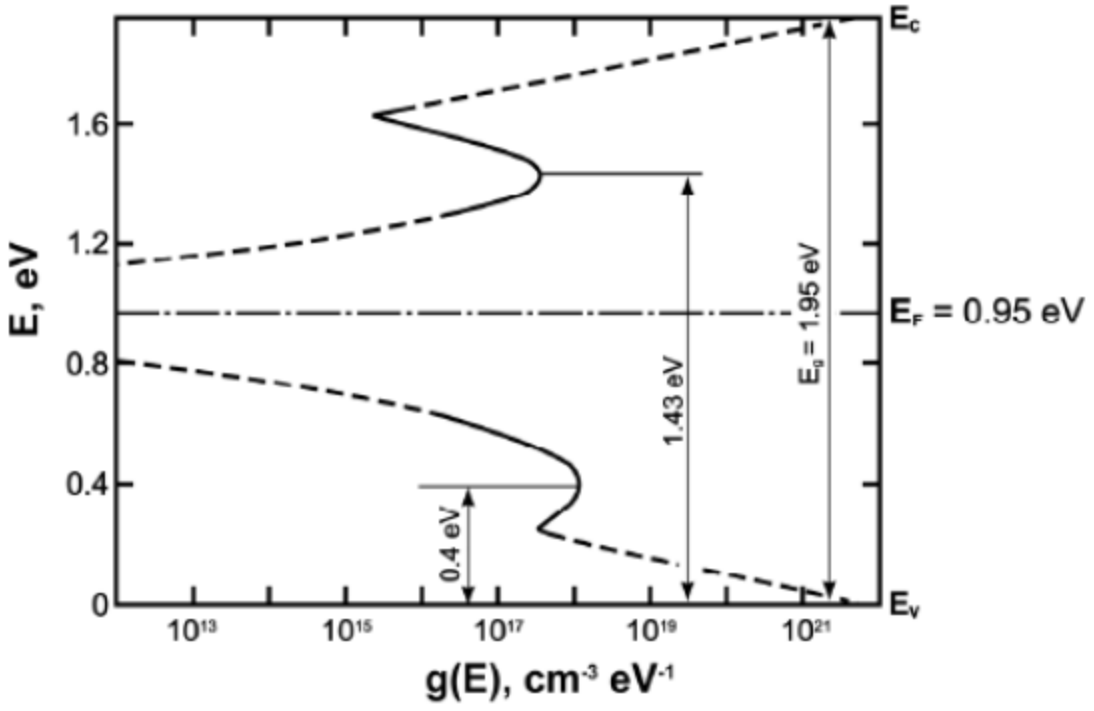

Figure 2.8: Schematic sketch of Adriaenssens's proposed model for the density of states distribution for a-Se. Single peaks at 0.4 eV above valence band edge E_v and at 0.52 eV below conduction band edge E_c from post-transit measurements. Figure constructed from [44].

In this model, the effective carrier mobility is expected to be determined by the decaying tail states.

$$\mu = \mu_0 \left(\frac{\Delta E}{kT}\right)^n \exp\left(-\frac{\Delta E}{kT}\right) \qquad 2.4$$

where ΔE is the width of the tail from the transport band, n is the power law dependence of the density of states on the energy, measured from E_c into the mobility gap, i.e. $g(E) = N_c[(E_t - E')/E_t]^n$ [37]. The DOS N_v decays to zero from E_v to $E_v + \Delta E$. Deep trapping states are not defined in this model and they do not affect the measured drift mobility from the transit time as long as there is no carrier release over the time scale of the experiment.

The concentrations of these trap states are much smaller in a-Se compared to other amorphous materials, especially other chalcogenide glasses, which further confirms the usefulness of a-Se as a suitable medium for X-ray photoconductor applications[37].

2.8 Recent Developments on Amorphous Selenium Photoconductors

Kabir in "Chapter 8, Handbook of Electronic and Photonic Materials" has critically discussed potential photoconductor materials, the charge transport and various properties such as X-ray sensitivity, Detector Quantum efficiency, Modular Transfer function, image lag and ghosting and their dependency on the detector structure and design [12].

The charge transport and image detector properties of various competing semiconductors such as a-Se, HgI_2, CdZnTe, PbI_2, PbO and TiBr are compared with the ideal photoconductor for X-ray imaging detectors. Table 2.2 and Table 2.3 displays the Material properties and Imaging properties of the potential detectors, respectively.

Table 2.2 Material properties of various photodetectors [45]

Photoconductor, state and preparation	E_g (eV)	$W_\pm$ (eV)	Density (g/cm^3)	Resistivity (Ω cm)	Electrons μ_e(cm^2/Vs), $\mu_e\tau_e$(cm^2/V)	Holes μ_h(cm^2/Vs) $\mu_h\tau_h$(cm^2/V)
Stabilized a-Se, vacuum deposition	2.1–2.2	~45 at 10 V/μm	4.3	10^{14}–10^{15}	$\mu_e = 0.003$–0.006 $\mu_e\tau_e = 0.3\times10^{-6}$–$10^{-5}$	$\mu_h = 0.12$ $\mu_h\tau_h = 10^{-6}$–6×10^{-5}
HgI_2, polycrystalline, PVD	2.1	5	6.3	$\sim 4\times10^{13}$	$\mu_e = 88$ $\mu_e\tau_e \approx 10^{-5}$–$10^{-4}$	$\mu_h = 3$–4 $\mu_h\tau_h \approx 10^{-6}$
HgI_2, polycrystalline, SP	2.1	5	6.3	$\sim 4\times10^{13}$	$\mu_e\tau_e \approx 10^{-6}$–$10^{-5}$	$\mu_h\tau_h \approx 10^{-7}$
$Cd_{0.95}Zn_{0.05}Te$, polycrystalline, vacuum deposition	1.7	5	5.8	$\sim 10^{11}$	$\mu_e\tau_e \approx 2\times10^{-4}$	$\mu_h\tau_h \approx 3\times10^{-6}$
PbI_2, polycrystalline, PVD	2.3	5	3–5	10^{11}–10^{12}	$\mu_e\tau_e = 7\times10^{-8}$	$\mu_h = 0.02$–0.15 $\mu_h\tau_h \approx 2\times10^{-6}$
PbO, polycrystalline, vacuum deposition	1.9	8–20	9.6	7–10×10^{12}	$\mu_e\tau_e \approx 5\times10^{-7}$	?
TlBr, polycrystalline	2.7	6.5	7.5	$\sim 5\times10^{9}$ at 20 °C	?	$\mu_h\tau_h \approx 1.5\times10^{-6}$

Table 2.3: Imaging properties of various photodetector [45]

Photoconductor, state and preparation	Typical operating F (V/μm)	Dark current (pA/mm^2)	Lag (fluoroscopic mode of operation)	Uniformity/sensitivity variation (standard deviation/average value)
Stabilized a-Se, single layer	~10	< 10 up to $F = 20$ V/μm	< 2% after 33 ms	Negligible
Stabilized a-Se, multilayer (PIN or NIP)	~10	< 1 up to $F = 20$ V/μm	< 2% after 33 ms	Negligible
HgI_2, polycrystalline, PVD	~0.5	~6 at $F = 0.5$ V/μm	~7% after 66 ms	~10%
HgI_2, polycrystalline, SP	~1.0	~8 at $F = 1.0$ V/μm	~7% after 66 ms	~10%
$Cd_{0.95}Zn_{0.05}Te$. polycrystalline	~0.25	~25 at $F = 0.25$ V/μm	~70% after 33 ms	~20%
PbI_2, polycrystalline, PVD	~0.5	10–50 at $F = 0.5$ V/μm	~75% after 66 ms	?
PbO, polycrystalline	~1.0	40 at 3 V/μm field	3–8% after 1 s	?
TlBr, polycrystalline	~1.0	?	?	?

Comparing the detector properties summarized in Table 1 and Table 2 clearly indicates that a-Se is the best choice for clinical X-ray image photodetectors. The next closest detector material is poly-HgI_2 which displays excellent Sensitivity, good resolution, acceptable levels of dark current and lag characteristics. Dark current and Image lag characteristics are poor in CZT, PbI2 and PbO detectors. The main downside of a-Se detector is its low conversion gain which affects the performance of the imaging sensor at low exposure. This can be resolved by utilizing on-pixel amplification [46] and/or by using the avalanche multiplication technique[47] in a-Se layer but additional research is needed to determine the basic operation and long term stability of this sensor utilizing these techniques[12].

As already discussed in earlier chapter, detector performance is determined by the X-ray sensitivity, Detective Quantum Efficiency (DQE) and Modulation Transfer function. X-ray sensitivity of a-Se, poly-HgI2, and poly-CZT detectors are listed in Table 2.4.

Table 2.4: X-ray sensitivity (S) and s for competing photodetectors [45]

Photoconductor	E (keV)	S_0 ($\mu C/cm^2R$)	$s = S/S_0$		S ($\mu C/cm^2R$)	
			Positive bias	Negative bias	Positive bias	Negative bias
Stabilized a-Se	20	0.244	0.9–0.98	0.8–0.98	0.22–0.24	0.2–0.24
	60	5.37	0.39–0.64	0.35–0.62	2.1–3.38	1.88–3.35
Poly-HgI_2	20	2.75	0.25–0.29	0.53–0.81	0.7–0.81	1.46–2.24
	60	38.54	0.15–0.3	0.21–0.4	6.76–11.21	8.18–15.6
Poly-$Cd_{0.95}Zn_{0.05}Te$	20	3	≈0.456	≈0.85	≈1.37	≈2.55
	60	35.87	≈0.41	≈0.51	≈14.69	≈18.12

The X-ray sensitivity (S) and s for competing photo detectors are listed in Table 2.4 and they were calculated using the normalized parameters Δ, x_e, x_h [12]. $s = S/S_0$, where S_0 is a constant that depends on E and the material properties of the detector. The maximum X-ray sensitivity S_0 value of a mammographic detector (E = 20 eV) is lesser than that of a conventional chest detector (E= 60 eV). The value of S_0 is higher in poly-HgI_2 and poly -CZT detectors compared to a-Se. S_0 for a-Se is less due to the higher value of $W_{\pm}$ [12].

The ability of the detector to transfer signal relative to noise from its input to output is termed as Detector Quantum efficiency (DQE). Kabir and Kasap has discussed DQE(0) (f = 0, where f is the spatial frequency) as a function of X-ray exposure for a-Se, poly-HgI_2, and poly- CZT detectors [48] . DQE(0) vs X-ray exposure plot for potential detectors listed above can be seen in Figure 2.9.

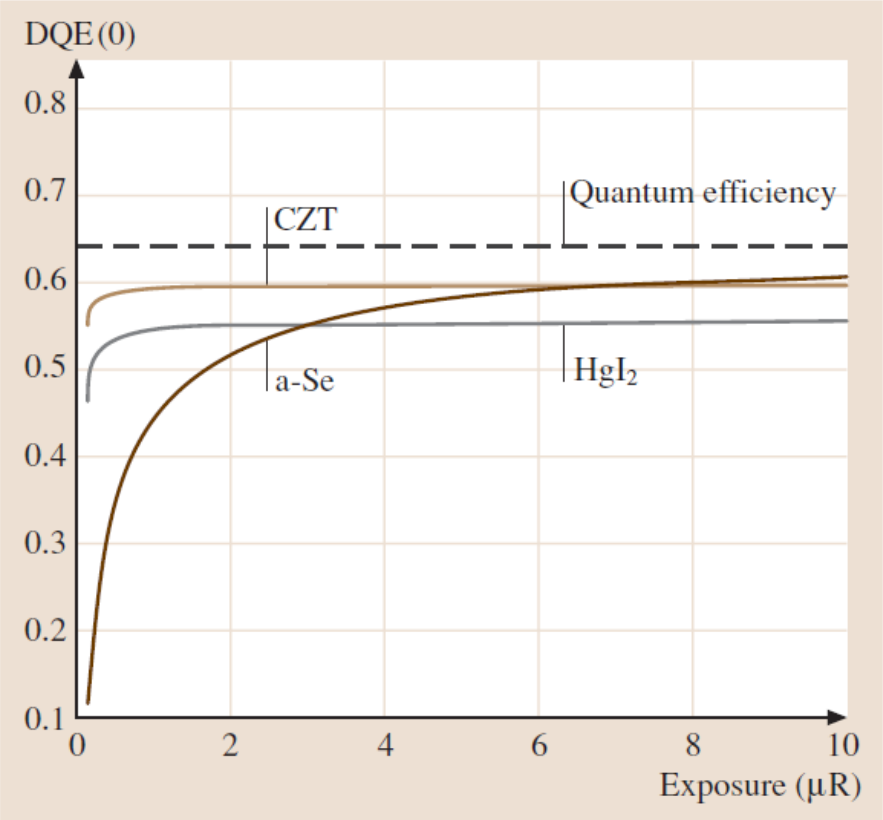

Figure 2.9: DQE(0) vs X-ray exposure for poly-CZT, poly-HgI_2, and a-Se for a 60keV monoenergetic beam. The field is assumed to be 10Vμm^{-1} for a-Se, 0.5V μm^{-1} for HgI_2 and 0.25 Vμm^{-1} for CZT[48].

From the Figure 2.9, it is observed that DQE remains unchanged for the CZT detector throughout the whole exposure range due to large conversion gain and high charge collection properties. The DQE for HgI_2 is smaller over the whole exposure range due to the low conversion gain. DQE for a-Se is small at low exposures and as the x-ray exposure increases the DQE increases. a-Se has low conversion gain. From the comparison, it is understood that high charge collection efficiency and high conversion gain are necessary to improve the DQE of X-ray image detector. The charge collection efficiency increases with increasing *F*, but increase in field greatly increases the dark current in CZT and HgI_2 detectors. Thus dark current can be kept small (within an acceptable limit) in a-Se even with the operating field of 20V μm^{-1}. Therefore the higher DQE can be observed in a-Se by achieving high charge collection efficiency (CCE) (due to high *F)* and with a reasonable W± which is a material property [48].

The ability to record separate images of small objects that are placed closed together is termed as resolution. The spatial resolution of an imaging device can also be termed as Modulation Transfer Function (MTF). In AMFPI, there is a loss of resolution due to charge carrier trapping and reabsorption of K-fluorescent X-ray photons. When some of the K-fluorescent X-ray photons are reabsorbed within the detector, there is a lateral spreading of signal and loss of resolution. The fluorescence reabsorption is maximum above the K-edge of the photoconductor. This can be overcome when the average energy of X-ray beam and K-edge occur at different energies and when the incident primary X-ray photon energy is lesser than the K-edge of the photodetector [49].

There is a significant effect on the resolution due to charge carrier trapping. Kabir and Kasap has examined that the effect of trapping on MTF increases with decrease in normalized life time [50]. It has been discussed that the MTF performance is degraded by trapping of carriers that moves towards the pixel electrode. This can be overcome and the sharpness of the image can be improved when these carriers move away from the pixels. Kabir and Kasap has modelled a theoretical fit with the experimental data for positively biased 300 μm CZT detector exposed to 80 kVp X-ray beam with 26 mm Al filtration. The experimental and theoretical fit are in good agreement and from Figure 2.10, it is seen MTF is due to the bulk carrier trapping only. This charge carrier trapping model can also be applied to a-Se and HgI_2 photodetectors [12].

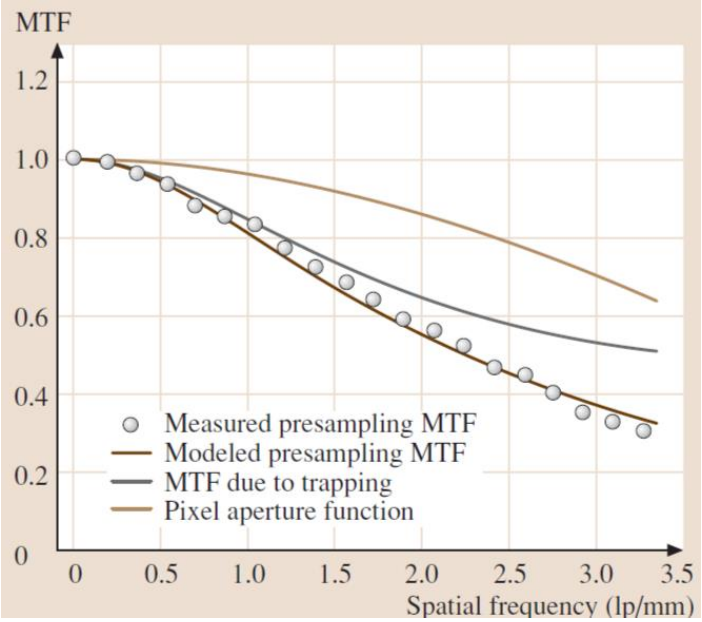

Figure 2.10: Theoretical and Experimental MTF fit for CZT detector. Detector thickness is 300 µm and Pixel pitch is 150 µm. MTF due to charge carrier trapping in the bulk of the photoconductor can be seen. (After [45] and [50])

2.9 Amorphous Selenium

The amorphous selenium (a-Se) photoconductor layer that is used as an x-ray photoconductor is called stabilized a-Se because of its alloying and doping components to stabilize a-Se against crystallization. Pure Se is not stable and tends to crystallize over a period of time from months to years and its crystallization rate depends on the ambient conditions. Pure Selenium when alloyed with 0.2-0.5% of As is termed as a-Se or stabilized Selenium. It is usually also doped with Cl in 0-20 ppm range. The doping with chlorine and alloying with arsenic in right amount ensures the desired type of electronic transport and maintains the stability of the photoconductive layer against crystallization. Typical transport properties of stabilized a-Se (a-Se: 0.2 – 0.5 % As + 0 – 40 ppm Cl) photoconductor films are represented in the Table 2.5. The effects of alloying with arsenic and doping with chlorine are discussed in the following sections.

Table 2.5: Typical properties of stabilized a-Se (a-Se:0.2-0.5 % As + 0- 40 ppm Cl) photoconductor film at room temperature [3].

Property	Typical Range	Schubweg at 5 V μm^{-1}	Comment
Hole mobility μ_h	0.12-0.14 $cm^2 V^{-1} s^{-1}$		Well reproducible. Probably shallow trap controlled.
Electron mobility μ_e	0.003-0.006 $cm^2 V^{-1} s^{-1}$		Decreases rapidly with As addition. Probably shallow trap controlled.
Hole lifetime τ_h	20-200 µs	1.2 – 12 mm	Depends on the substrate temperature.
Electron lifetime τ_e	200-1000 µs	0.3 – 1.5 mm	Sensitive to small quantity of impurities.
Hole range $\mu_h\tau_h$	2- 20x10^{-6} cm^2 V^{-1}		Substantially higher than PbI_2.
Electron range $\mu_e\tau_e$	1- 6x10^{-6} cm^2 V^{-1}		Somewhat higher than PbI_2.

Effect of Chlorine Doping in Amorphous Selenium

Doping a-Se with a few ppm of chlorine results in drastic effects on the electrical conductivity of Se [51]. Interrupted field Time-of-flight (IFTOF) experiments performed by Belev has illustrated that the addition of chlorine to a-Se has a significant effect in the transport property of holes and electrons. Increasing the concentration of chlorine increases the τ_h and $\tau_h \mu_h$. The hole drift mobility is unaffected by the addition of chlorine. Increasing the concentration of chlorine in a-Se tend to result in an opposite behavior in the electron transport i.e. the electron lifetime decreases with increase in chlorine doping. Similar to the hole drift mobility, the electron mobility also remains unaffected with the addition of chlorine.

Amorphous selenium has valence alternation pair (VAP) type intrinsic defects. These are over-coordinated atoms which corresponds to a positively charged triply bonded center $Se_3^+(D^+)$ and the under-coordinated atoms which is a negatively charged center Se_1^- (D^-) [52, 53]. It is believed that over Se_3^+ and under Se_1^- charged defects act as deep electron and hole traps in a-Se. Chlorine has high electronegativity (3.16) compared to Selenium (2.55) and the following reactions can be caused because of it.

$$Se_2^0 + Cl_1^0 \longrightarrow Se_3^+ + Cl_0^- \qquad 2.5$$

$$Se_1^- + Cl_1^0 \longrightarrow Se_2^0 + Cl_0^- \qquad 2.6$$

Addition of chlorine to the neutral selenium structure forms two types of defects. First is the well-known Se_3^+, which means that their concentration must increase. The second is Cl_0^-, which means that the Se_1^- concentration must decrease so that the overall neutrality is maintained. If one assumes that the occupied (by a single electron) center Cl_0^- does not produce a state in the mobility gap, then the above two reactions can explain the observed changes in the electrical properties. The decrease in deep hole traps increases the hole life time. This theory works, only when it is assumed that Cl_1^- does not act as deep or shallow hole trap [18]

Effect of Alloying a-Se with Arsenic

The alloying of a-Se with of arsenic has two effects. First is that the As has a valency of 3 and bonds with three neighbors. This means that it is able to link Se-chains together and crystallization chains have been aligned in the crystal with the dihedral angle along a chain having the same sign. Further, the hole life time (τ_h) and the hole range$(\tau_h \mu_h)$ both decrease with the addition of arsenic but the hole drift mobility remains unaffected. In the case of electron transport, the addition of As increases the electron lifetime and the drift mobility of the electrons decreases. The overall increase in the electron lifetime τ_e results in an increase in electron range$(\tau_e \mu_e)$ [18].

The effect of hole transport and electron transport due to alloying with small amounts of arsenic can be explained by the following structural changes upon the introduction of As.

$$Se_3^+ + As_3^0 \longrightarrow Se_2^0 + As_4^+ \qquad 2.7$$

$$Se_2^0 + As_3^0 \longrightarrow Se_1^- + As_4^+ \qquad 2.8$$

The electronegativity of arsenic is 2.18 whereas that of selenium is 2.55. Thus a Se atom has more attraction for electrons than an As atom. One could therefore argue that the formation of the under-coordinated negative As_2^- center is less likely than that of the formation of the under-coordinated Se_1^- center. Thus, the modification of the structure by $Se_2^0 + As_3^0 \rightarrow Se_3^+ + As_2^-$ is less likely than the second reaction in Equation 2.8.

Reaction in Equation 2.7 explains the effect of arsenic on electron transport because if As_4^+ is assumed to be a shallow electron trap then its formation reduces the drift mobility. It also represents the conversion of a deep electron hole trap to shallow electron trap resulting in the

population increase of shallow electron traps .Thereby the electron life time increases and the drift mobility decreases[18]. While this explanation can certainly account for the observations qualitatively, it cannot explain the observation quantitatively because there is actually a distinct increase in the $\mu_e \tau_e$ product for electrons.

Reaction in Equation 2.8 explains the formation of the deep hole traps, remember that the whole medium has to be neutral. The formation of negative charged shallow electron traps must be accompanied by the formation of Se_1^- negative centers. It should be emphasized that while we only need a few ppm of chlorine addition for large changes in the electrical properties, we need 0.1 – 1 % alloying with As for similar changes [18]. In terms of scientific understanding and reproducibility, the electronic properties of a given Se alloy has a strong dependence on the starting pure Se material [51].

Dark Currents in Amorphous Selenium Photoconductors

There are several factors that determine the quality of the image and the performance of the detector. Dark current is one among the important characteristics of a photodetector which determines the performance of the detector in a particular application. The dark current is defined as the "unwanted electric current" that is generated by the photodetector in the dark arising from the application of a bias voltage. This dark current is the cause of noise and it reduces the dynamic range (DR) of the photodetector. Various experiments performed by several authors have created a systematic model for denoting the transient and steady state behavior of dark current in a-Se detectors. Their results were obtained by considering the main source of dark current as carrier injections from the metallic contacts and thermally generated carriers [54]. Those results have also denoted that the dark current was mainly due to the injected carriers from a Schottky type contacts and the thermal generated carriers were negligible [55]. In these previous works, it has been described that the injection of carriers from the metal is dependent of the blocking layer thickness, carrier release time, concentration of traps in the blocking layer and the effective barrier height [3].

2.10 Optical Properties

When an optical photon is incident on an a-Se, the probability of absorption of the photon within the a-Se medium depends on the absorption coefficient α of the photoconductor and it is dependent upon the energy of the incident photon and the density of states. If the energy of the incident photon is less than the bandgap then the absorption coefficient is small because there are not many states with which the photon can interact. When the incident photon has a higher energy than the bandgap, then the absorption coefficient magnitude can be significant because the photon can now interact with a large density of states. There is a direct relationship between the magnitude of the absorption coefficient and the density of states distribution [56].

Experimental studies on a-Se have given the Urbach edge of the form $(h\nu) = 7.35 \times 10^{-12} \exp(h\nu/0.058)$ eV cm^{-1}. The Urbach edge is believed to represent the excitation of charge carriers from tail states or gap states to extended states [57]. When the energy of an optical photon is more than the bandgap, absorption coefficient α has been found to follow $\alpha h\nu \propto (h\nu - E_0)$ where $E_0 \approx 2.05$ eV at room temperature. This behavior indicates a band-to band type excitation is involved. Tauc's law in the form $\alpha h\nu \propto (h\nu - E_0)^2$ has also been reported for a-Se and gives an optical bandgap $E_0 \approx 1.9$ eV [58].

Tan et al [42] have fitted $\alpha h\nu$ vs. $h\nu$ data for a cold deposited a-Se (Figure 2.11) to the "linear Tauc rule" in which $\alpha h\nu = B(h\nu - E_{\mathrm{op}})$, where E_{op} is called the optical bandgap. Tan et al find E_{op} to be about 2.0 eV.

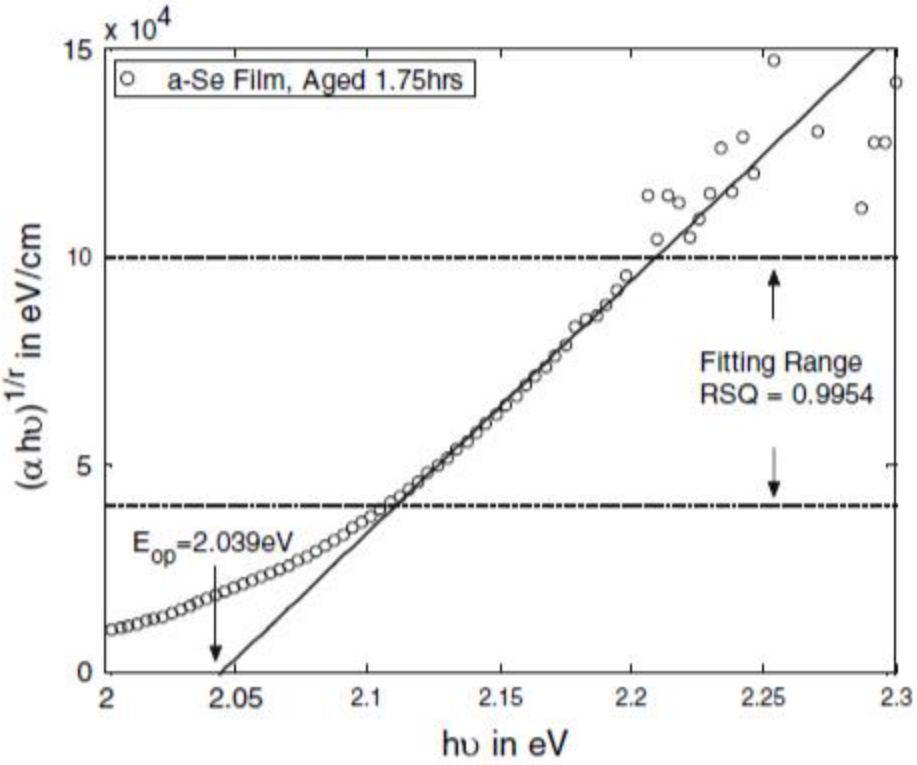

Figure 2.11: $(\alpha h\nu)^{1/r}$ vs. $h\nu$ for a cold deposited a-Se film with thickness d = 2.026 μm. The best fit gives r = 1 [42].

Tan et al have found that, the best r depends on the exact data range but it is typically close to '1' and it does not change during aging or annealing. Similarly, the fundamental absorption for various cold deposited, hot deposited, Cl-deposited a-Se films have been examined and they follow $\alpha h\nu = B(h\nu - E_{\mathrm{op}})$ with E_{op} = 1.99 – 2.05 eV. The optical gap and Urbach edge show no dependence on 67 ppm Chlorine doping. It was concluded that ΔE does not depend on aging or annealing but there is a slight decrease in E_{U04} [42].

2.11 Summary

The theoretical background for understanding the electronic and optical properties of amorphous selenium and it alloys were discussed in this chapter. Based on the modern theory of solids, the electrical and optical properties of a-Se material were demonstrated. The band theory of solids was derived from quantum mechanical treatment of the relationship between the bonded electrons when large number of atoms were brought together to form a bulk solid. As there is no

long range order in amorphous solids it is difficult to represent the analytical derivation of the band model. On the other hand, several experimental observations and research in the electronic and optical properties in these amorphous materials has said that crystalline band model can also be applied to amorphous semiconductors.

In this chapter, common bonding arrangement of amorphous selenium is discussed and said that dihedral angle varies randomly in a-Se. Localized electronic states and thermodynamically stable VAP defects exists in the bandgap. The location and density of these localized states have a thoughtful impact on the optical and transport properties of amorphous materials

The optical and electronic properties of a-Se are related to the density of states function. Several experimental researches on amorphous materials have been discussed in this chapter to develop a generalized shape of density of states function. Recently it has been accepted that the structural disorder in the material has resulted in encroachment of localized states in the forbidden gap of the material. The thermodynamically stable VAP defects introduce mid-gap states. The carrier lifetime, and hence the carrier schubweg are controlled by the mid-gap states and carrier mobility is controlled by localized tail states.

CHAPTER 3. EXPERIMENTAL PROCEDURE AND TECHNIQUES

This chapter provides a description of the selenium sample structure used to study the dark current transients during irradiation with X-rays and preparation of sample sets. Five different amorphous selenium sample structures were used to study the dark current transients with X-ray exposed at different time intervals. These sample sets were fabricated at Anrad's laboratories in Quebec. Dark current transients produced by these samples have been examined as a function of time, applied voltage, discharge currents, X-ray dosage, and sample structure.

3.1 Sample Set A

Four samples from the Sample set A were used to examine the dark current measurements with applied electric fields and X- ray exposure. These mammographic type samples are approximately 210 µm thick samples with various kinds of structures listed in Table 3.1.The *p-i-n* photodiode like structures are used in commercial FPXI's were implemented based on the assumption that the dark current is dominated by the career injections from the contacts.

A *p-i-n* sample from Sample set A is photgraphed and can be seen in Figure 3.1. The *p-i-n* sample has a glass coated substrate electrode with ITO as a conductive layer and the top electrode is Cr coated in an area of $21 cm^2$. All the *i*-layers in this set has non-chlorinated Se:0.2%. As alloy with determined electron and hole schubwegs of 5mm and 6mm respectively at 10V/µm. The *p*-layers are a-As_2Se_3 which is 2 µm thick and *n*-layer is alkali doped stabilized a-Se and it is roughly 6µm thick. By varying the *p-i-n* structure and holding all other parameters as constant as possible the exact effect of each layer and its position can be determined [3]. These effects are observed by measuring the dark current transients of the samples as a function of electric field and time and comparing them with different structures.

Figure 3.1: Photo of a sample from sample set A, with its entire top surface coated with chromium, which forms one of the electrodes.

3.2 Sample Set C

To further analyse the dark current , *n-i-p* multiple sandwiched structure from sample set C was experimented. This sample has the Aluminium thin contact deposited and platinum thin contact sputtered on the top surface each of area $1.2 cm^2$ and the dark currents produced in aluminum and platinum area of the sample is analysed. The substrate electrode of the sample is coated with glass with ITO as conductive layer.The *n*-layer and *p*-layer is 6µm thick with former made of alkali doped a-Se and latter is $As_2 Se_3$. The i-layer is made of stabilized a-Se alloyed with 0.3% As and doped with 2.5ppm Cl.

Table 3.1: Summary of characteristics of sample set A and C.The sample structure represents the next layer to the radiation receiving electrode

Sample set	Sample Number	Structure	*n*-layer thickness (µm)	*i*-layer thickness (µm)	*p*-layer thickness (µm)
A	839-4	i-layer	-	212	-
	847-2	n-i	7	198	-
	842-1	p-i	-	223	2
	850-1	p-i-n	6	193	2
C	1452-1	n-i-p	6	196	6

3.3 Sample Preparation

Amorphous selenium (a-Se) is used as a X-ray photoconductor as it satisfies three conditions which are necessary in X-ray imaging. It has a very good X-ray photosensitivty and produces high signal, has high resistance and limits dark current and it can be inexpensively prepared. Samples A and C used in the analysis of dark current were prepared by Vapour deposition process. A-Se thin film samples are prepared by thermal evaporation of selenium in the form of small, vitreous pellets from a molybdenum boat in a standard vacuum system.The substrate and the boat temperature determines the elecronic quality of amorphous Selenium samples [59].

Glass substrates coated with ITO layer were used in the preparation of a-Se thin layer films. The substrate was cleaned in an ultrasonic bath and blown dry with compressed and filtered air [3]. A-Se films with good electron and hole times require substrate temperature to be high as possible during vacuum deposition and above the glass transition temperature. Keck has discovered that a-Se films are produced when the substrate temperature is less than 50ºC and many hexagonal crystallites appeared on the films when the substrate temperature is more than 90ºC [59].

NORTON NRC 3117 vacuum coater (Figure 3.3) is used for the deposition of the photoconductive layer. The vacuum pressure inside the system is less than ~ 10^{-6} torr. The substrate temperature is increased more than the glass transition temperature around 60ºC - 65ºC for Se and 70ºC for As_2Se_3 by the substrate heater. The substrate heater is otherwise known as radiative heater and its temperature is maintained within 0.5ºC. The boat has the selenium pellets melted at 230ºC and cooled to desired temperature. The selenium pellets in the boat were melted by passing large ac current (100- 150A) through the boat. The source and substrate temperature were controlled electronically by thermocouple system. The boat and substrate temperature profile are seen in Figure 3.2 [59]

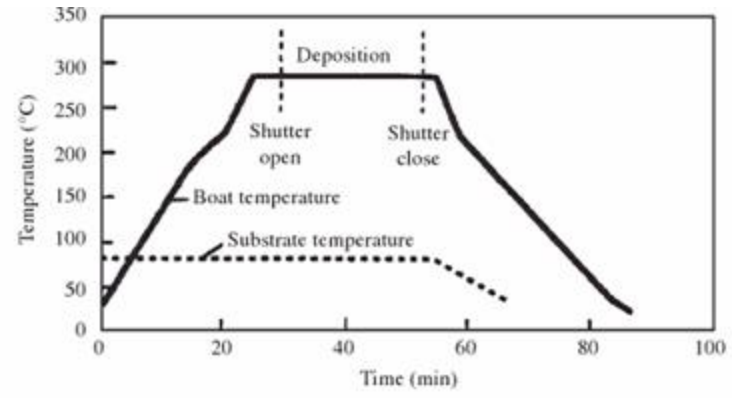

Figure 3.2: Boat and substrate temperature versus time profile [59].

The molybdenum boat is heated to 250ºC and 400ºC for Se and As_2Se_3, respectively. When the boat temperature reaches a constant value the shutter is opened and the deposition is allowed on the substrate. The substrate is protected until steady evaporation and steady deposition cool down conditions are met by the shutter operations. The sample was then removed from the system and placed in dark environment under room temperature for stabilization. The thicknesses of the deposited layers are then measured with Perkin Elmer Lambda 900 photo spectrometer and digital micrometer [3] [59].

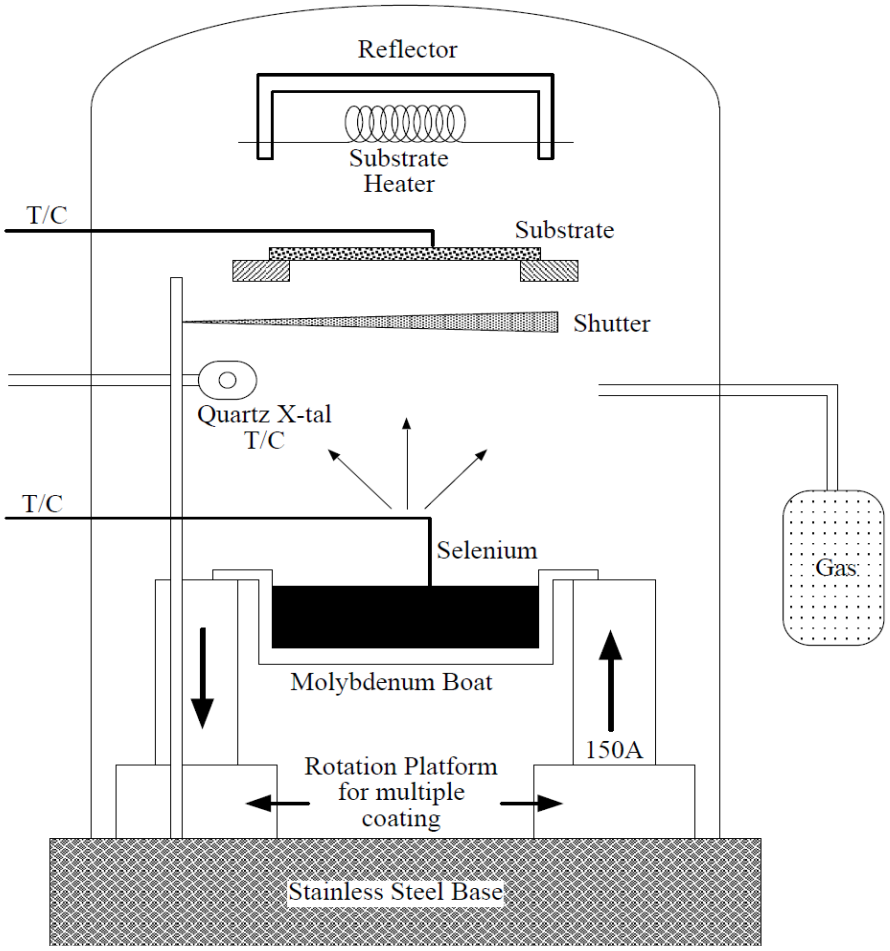

Figure 3.3: Schematic diagram of NORTON NRC 3117 vacuum coater [59]

3.4 Fabrication of Thin Film Contacts

The contacts over the glass substrate were deposited by evaporation and sputtering techniques. The U of S Electronic Research lab used Hummer VI unit for DC Sputtering and METROVAC coating unit for evaporation. The contact deposited on the substrate determines which technique and unit can be used for the deposition process. However the DC sputtering technique by Hummer VI unit was less expensive compared to the METROVAC coating process. The coating process is very gentle and it eliminates the effect of very high temperature and damages caused by electron bombardment.

Custom milled shadow masks were used in the fabrication technique to make the contacts . The schematic diagrams of the sample structures with top and bottom contacts used in the analysis of dark current can be seen in the Figure 3.4.

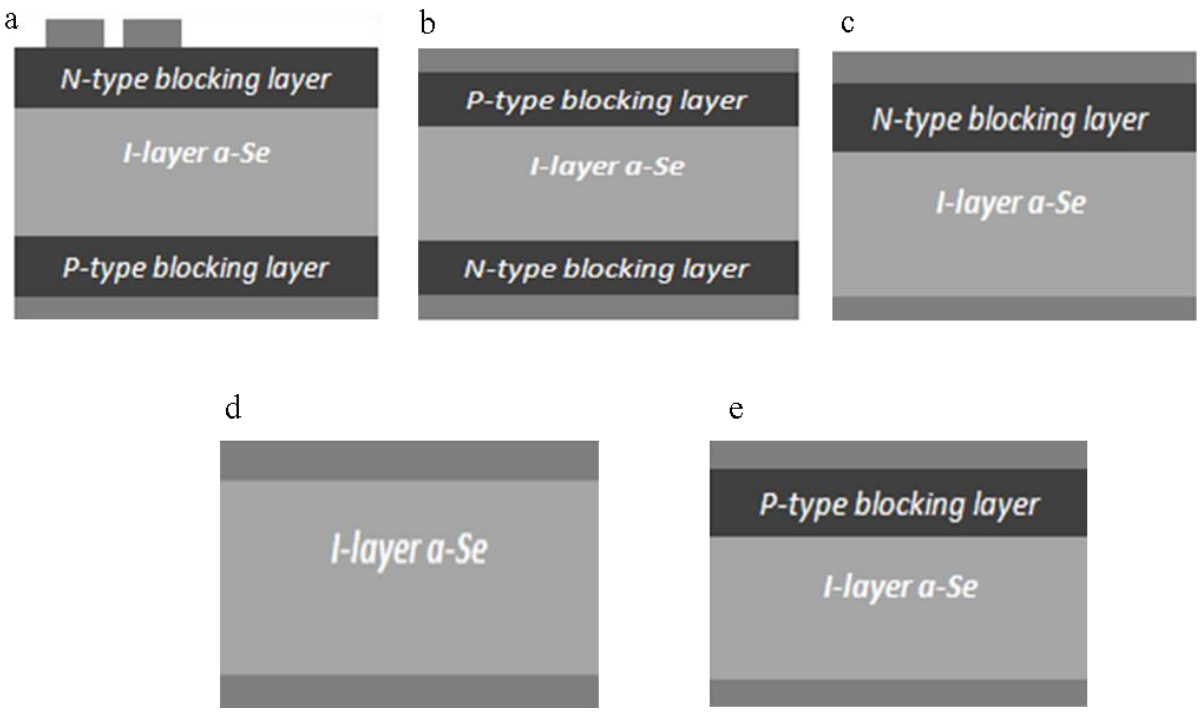

Figure 3.4: Sample structures used in the dark current measurement (a) *n-i-p* layer, (b) *p-i-n* layer, (c) *n-i* layer, (d) *i*-layer, (e) *p-i* layer

Amorphous selenium used in photoconductor applications is stabilized and the stabilization process is done by alloying a-Se with small amounts of As (0.2 %- 0.5%) and chlorine is doped in parts per million range. Alloying pure Se with Arsenic delays crystallization in the sample and the deep hole traps produced by the addition of As is prevented by doping Chlorine [11]. Addition of Cl with Selenium improves the hole transport and drastically reduces the electron lifetime. The electron life time values are always less than ~10μs and it was estimated from the decay rate of the photocurrent values [51].

Many researches have previously reported that amorphous selenium (a-Se) semiconductor material is well suited for large-area solid state device applications due the fabrication of a-Se photoconductive layers by conventional vacuum deposition techniques. The dark current is an important characteristic of a detector, and determines the performance in terms of detective quantum efficiency (DQE). In this chapter, we will discuss the principles and techniques involved in the measurement of the dark current in different stabilized a-Se samples before and after exposure, as well as the x-ray exposure system used.

3.5 Experimental Technique Used in Dark Current Measurements

The Experimental unit consists of a PS 350 High Voltage power supply, a computer workstation, dark chamber where the sample is placed, X-ray unit, GPIB interface and a Keithley 6512 electrometer as shown in Figure 3.5. The voltage to the sample in the dark chamber is supplied by the Stanford Research PS 350 High voltage Power supply which can supply a voltage from 0 to 5000 V. The dark current in the sample is measured by the Keithley 6512 electrometer and the measurement ranges from 0.1 fA to 20 mA. The PS 350 high voltage power supply and Keithley 6512 electrometer are connected to the computer workstation by the General Purpose Interface Bus. The X-ray unit has a Siemens Heliodentic X-ray tube to expose the samples to x-ray radiation. The X-ray tube has tungsten anodes and operates at a tube voltage of 57 kV and a tube current of 7 mA. The aluminum filtration in the beam is 2 mm. A photograph of Heliodentic X-ray tube is shown in Figure 3.6. The Heliodentic X- ray tube angle and the sample are aligned in such a way that all of the sample captures the X-rays. The light proof chamber has a lead shield to prevent the leakage of X-ray radiation to the outside environment.

Dark current measurements were done on 5 different samples *p-i, n-i, i, n-i-p,* and *p-i-n* structures. The sample to be tested was first rested inside the chamber in the dark for 8 hours and the dark current was measured. The same cycle was repeated 3 times with different resting periods till lowest dark current was measured. After the last cycle, each sample was rested for 24 hours in short circuit prior to the dark current measurements. The current vs time data were taken with the electrometer as shown in Figure 3.5. As the dark current transients have features that can occur several hours after the application of a high voltage, the measurements were automated using a computer and communication over a GPIB interface. The system allows the measurement of a maximum current of 0.5 mA, due to the internal current limiting resistance. Noise current coupled capacitvity from the high voltage power supply is of the order of 0.1 pA.

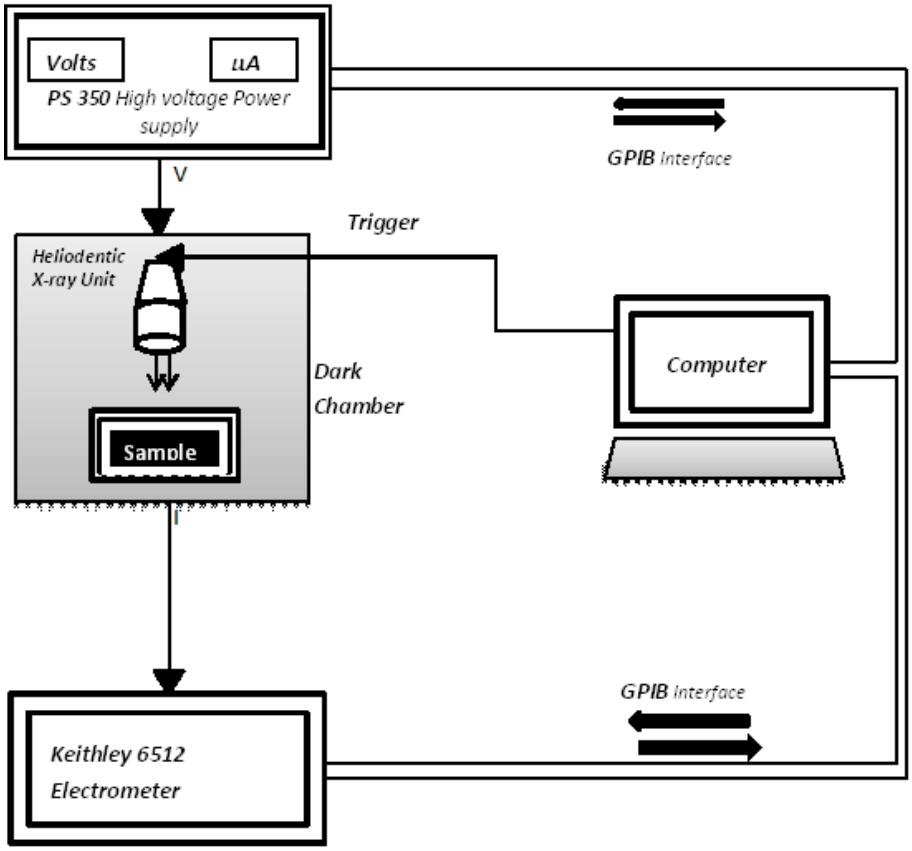

Figure 3.5: Experimental setup for measuring dark current in amorphous selenium photoconductors

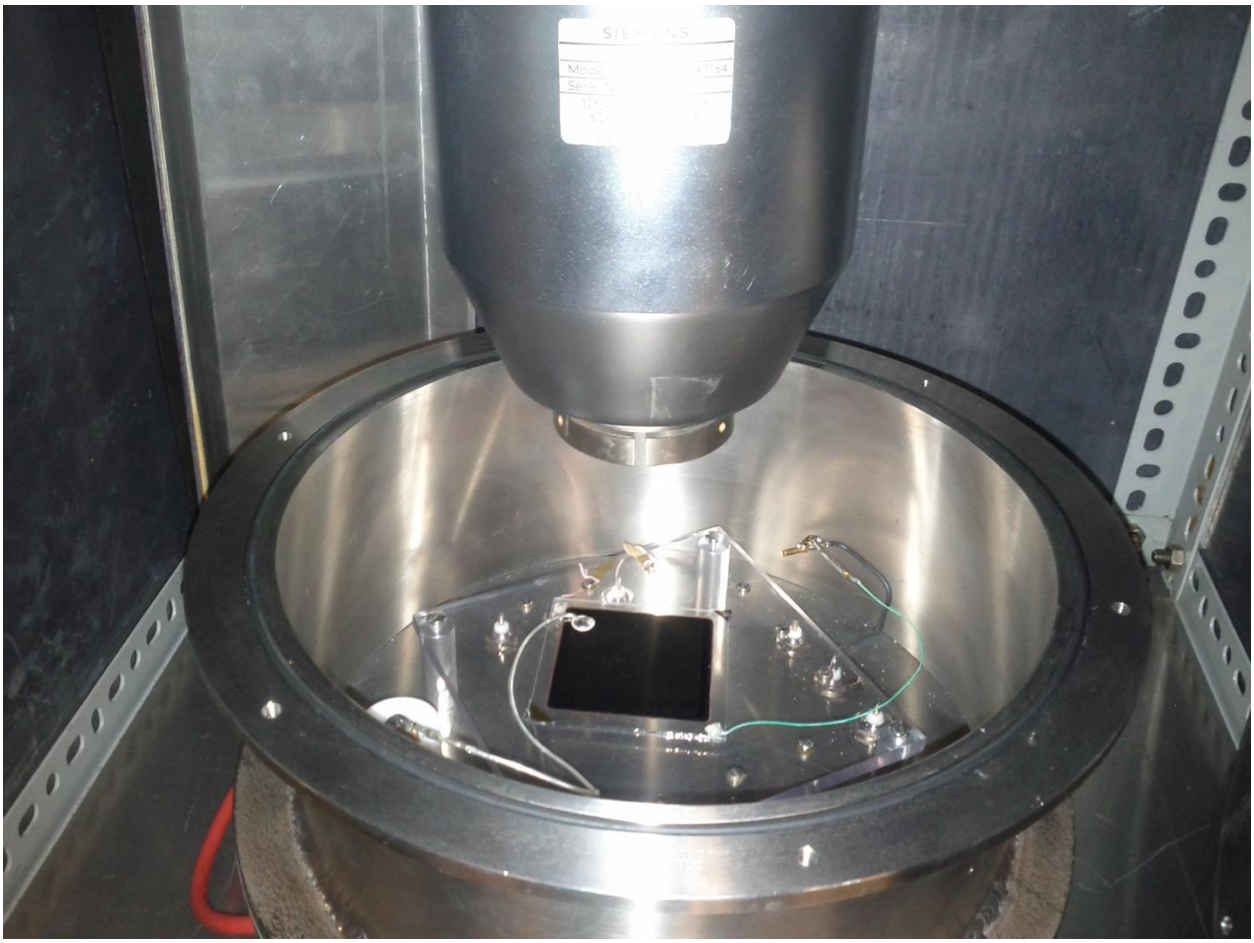

Figure 3.6: Stabilized amorphous selenium sample placed in the X-ray chamber with the contacts connected.

The positive and negative current follow directions and the terminology for positive and negative bias are important factors in the discussions of the experimental data. These will be defined below.

Figure 3.7 represents a schematic diagram of a *n-i-p* sample that has the *n*-layer next to the top contact, that is, the radiation receiving electrode. In this configuration, the top contact is biased positively with respect to the bottom contact in analogy with the *n-i-p* photo detector terminology in optoelectronics. It is termed as positive bias. When the sample is positively biased, the injected holes from the high voltage power supply will be trapped in the *n*-layer and the electrons injected from the bottom electrode will be trapped in the *p*-layer. The term reverse

bias is also used to describe this condition. It is important to emphasize that in a-Se detector technology, the *p*- and *n*-layers do not represent layers that behave similarly to *p*- and *n*-type crystalline silicon in which the Fermi level is either close to E_v (*p*-type) or E_c (*n*-type). The *p*- and *n*-layers in this case are layers that trap electrons and holes respectively so that electron and hole injections from positive and negative contacts are suppressed. The term forward biased will be used when the *p-i-n* sample is positively biased or when an *n-i-p* sample is negatively biased.

Irrespective of the biasing condition, the positive direction of the current will always be defined to flow from the positive electrode of the battery as represented in Figure 3.7.

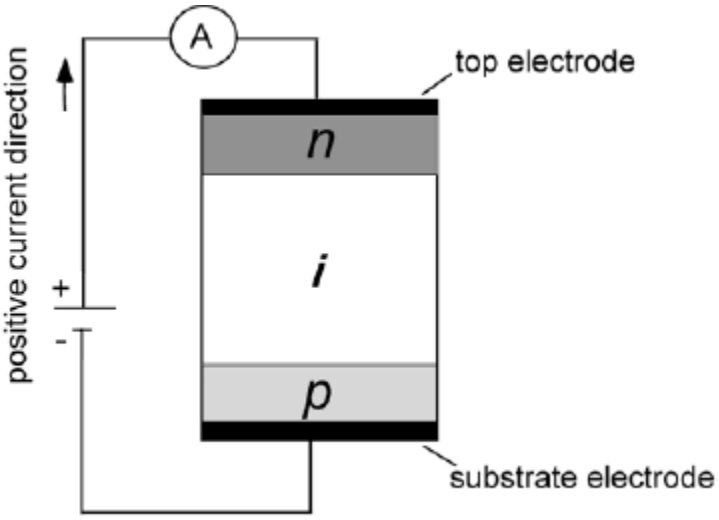

Figure 3.7: Representation of *n-i-p* sample under reverse biased condition. Irrespective of the biasing condition, positive current direction can be seen flowing into the top contact from the power supply.

The applied voltage to the sample was determined by the thickness of the device. To obtain results that are related to the practical use of a-Se detectors, the applied field as set to 10 $V\mu m^{-1}$, which is a typical operating field in a practical detector.

3.6 Measurement of X-ray Exposure and Dose

Radiation Related Quantities

There are a number of ways in which ionizing radiation is characterized. Roentgen is an ionizing radiation exposure unit. It is widely used. One roentgen (1 R) is defined as the amount of radiation that will impart sufficient energy to 1 cm^3 of air to ionize an amount of charge that is $(1/3)\times10^{-9}$ C at STP (standard temperature and pressure). Thus 1 R ionizes 1 cm^3 of air to generate 0.33 nC of charge. At STP, 1 R releases 2.58×10^{-4} C of charge per kg of air. The amount of energy that 1 R deposits into a volume of 1 cm^3 of air is 1.14×10^{-8} J/cm^3 or, stated differently, the energy deposited by 1 R into a 1 kg of air is 8.77×10^{-3} J/kg (Table 3.2).

Table 3.2: Definition of 1 Roentgen

1 Roentgen on	1 cm^3 of air	1 kg of air
Charge released	0.334×10^{-9} C / cm^3	2.58×10^{-4} C / kg
Energy deposited	1.14×10^{-8} J / cm^3	8.77×10^{-3} J / kg

X-ray dose, as different from exposure, represents how much energy is actually absorbed from an incident ionizing radiation (X-rays and γ-rays) per unit mass of a body subjected to the radiation; it is measured in Grays (Gy). Suppose that when an ionizing radiation is incident on a body of mass M, a mean energy $E_{absorbed}$ is absorbed from the radiation, then the *mean absorbed dose D* in units of J kg^{-3} that is in Gray or Gy is

$$D = E_{absorbed}/M$$

Dose in *air* and *exposure* both refer to a given amount of air, and hence can be readily converted between each other. At STP, 1 R of exposure is equivalent to depositing 8.77×10^{-3} J into 1 kg of air. Thus 1 R = 8.77 mGy or 1 μR = 8.77 mGy; or 1 mGy = 114 mR. Exposure always involves the ionization of air. On the other hand, dose depends what medium has been subjected to the radiation, and thus its determination always involves calculating the actual energy absorbed by the medium per unit mass. Dose calculations require the knowledge of the spectrum of the incident radiation (photon fluence vs photon energy) and knowledge of the the mass attenuation and mass energy absorption coefficients of the constituents present in the body; quite complicated compared with exposure.

Mass attenuation coefficient is the *linear attenuation coefficient* (μ) of a medium for high energy radiation per unit density (ρ) of the medium, μ/ρ. Most important property is the linear attenuation coefficient μ which is defined as the fraction of photons lost from the radiation beam per unit distance of propagation in the medium; the loss may be due to absorption and/or scattering. If $N(E)$ is the number of photons each with energy E traveling in the direction of a collimated beam of radiation along a particular direction z in a medium, then $\mu(E)$ at the photon energy E is defined by

$$\mu(E) = -\frac{1}{N(E)} \cdot \frac{dN(E)}{dz} \qquad 3.1$$

so that the photon concentration decays exponentially

$$N(E) = N_o(E)\exp[-\mu(E)z] \qquad 3.2$$

where N_o is the number of photon at $z = 0$. The attenuation depth δ is the reciprocal attenuation coefficient, $\delta(E) = 1/\mu(E)$. The coefficient $\mu(E)$ depends on the photon energy E as well as the density ρ and the atomic number Z of the medium. For high energy radiation such as x-rays, it has been found that μ depend linearly on the density ρ. *Mass attenuation coefficient* is the linear attenuation coefficient of a medium normalized by its density, *i.e.* it is μ/ρ with units $cm^2.g^{-1}$. Usually standard tables list the mass attenuation coefficient μ/ρ rather than μ. Therefore, the number of photons N at z becomes $N = N_o \exp[-(\mu/\rho)\rho z]$. Attenuation can be due to a number of reasons, such as the photoelectric effect (absorption), Compton scattering, Rayleigh scattering, and triplet production. The *total mass attenuation coefficient* can be written as

$$\frac{\mu}{\rho} = \frac{\tau}{\rho} + \frac{\sigma}{\rho} + \frac{\sigma_r}{\rho} + \frac{\pi}{\rho} + \frac{\gamma}{\rho} \qquad 3.3$$

where τ, σ, σ_r, π and γ are attenuation coefficients due to the photoelectric effect (τ), Compton scattering (σ), Rayleigh scattering (σ_r), pair production (π) and triplet production (γ). In the present case., over the present range of photon energies, only the first two terms are important. It should be emphasized that μ, or μ/ρ, does not specify how much energy has been deposited into the material; it simply characterizes the attenuation. μ/ρ for mixtures and compounds can be easily calculated from the simple summation (additivity) rule

$$\frac{\mu}{\rho} = \sum_i w_i (\mu / \rho)_i \qquad 3.4$$

where w_i is the weight fraction of the ith constituent in the compound.

The actual energy E_{absorbed} deposited into a medium by high energy radiation per photon of energy E is characterized by the mass energy absorption coefficient μ_{en}/ρ,, which can be defined by

$$E_{\text{absorbed}} = E \frac{(\mu_{\text{en}} / \rho)}{(\mu / \rho)} \qquad 3.5$$

μ_{en}/ρ is not exactly the same as μ_{tr}/ρ because the latter characterizes how much kinetic energy has been given to charged particles and not necessarily deposited into the material. As these charges decelerate in the medium they lose energy by radiation (Bremsstrstahlung) that escapes the material so that μ_{en}/ρ is less than μ_{tr}/ρ.

The *energy fluence* Ψ_E of incident ionizing radiation is the incident beam energy per unit area, and it increases linearly with the exposure X (Roentgens) [60]

$$\frac{\Psi_E}{X} = \frac{2.58\times10^{-4} W_{\text{air}}}{e(\mu_{\text{en,air}} / \rho_{\text{air}})} = \frac{0.00873}{(\mu_{\text{en,air}} / \rho_{\text{air}})} \quad \text{J cm}^{-2}\ \text{R}^{-1} \qquad 3.6$$

where the density of air is ρ_{air} and its mass energy coefficient is $\mu_{\text{en,air}}/\rho_{\text{air}}$ at the photon energy of interest, and $\mu_{\text{en,air}}/\rho_{\text{air}}$ is in $\text{cm}^2.\text{g}^{-1}$. If E is the photon energy, photon fluence Φ, the number of photons incident per unit area per Roentgen, is

$$\Phi = \frac{\Psi_E}{E} = \frac{8.73\times10^{-6}}{(\mu_{\text{en,air}} / \rho_{\text{air}})E} \qquad 3.7$$

in which E is in keV. According to Boone [61] the photon fluence at one photon energy E per unit exposure is given by

$$\Phi = \Phi(E) = \left[a + b\sqrt{E} \ln E + \frac{c}{E^2} \right]^{-1} \qquad 3.8$$

where Φ is in photons mm^{-2} per mR and E is the photon energy in keV, and $a = -5.0233\times10^{-6}$, $b = 1.8106\times10^{-7}$, $c = 0.0088387$.

Deposited energy or absorbed energy by a medium per unit area can be calculated from

$$E_{\text{absorbed}} = \int_0^{E_{\max}} \Phi(E) E \frac{\mu_{\text{en}}}{\mu} [1 - \exp(-\mu L)] dE \qquad 3.9$$

Exposure and Dose Measurement

To measure the amount of X-ray exposure the sample experiences, a Keithley 35050 dosimeter, an ion chamber model 96035, was used and connected to a Keithley voltmeter. The X-ray source was the same as above, a Siemens Heliodentic X-ray tube. The Keithley 35050 dosimeter and Ion chamber can be seen in the Figure 3.8 and Figure 3.9.

Figure 3.8: Keithley 35050 dosimeter for measuring the X-ray dosage

Keithley 96035 Ion chamber

Figure 3.9: Keithley 96035 ion chamber

Figure 3.10: Keithley Programmable Electrometer and High voltage power supply used for applying bias voltage across the sample. It provides stable DC voltages up to 5000 V, allowing for fields up to 25 V μm^{-1} for mammographic detector type samples. The resultant current is measured by the Keithley programmable electrometer with a current range of 2 fA to 20 mA.

The ion chamber (Figure 3.9) was connected to the Keithley integrator using tri-axial cable and the integrator was connected to the Keithley voltmeter (Figure 3.10). The Ion chamber was placed inside the light proof chamber where the samples are usually placed. The front face of the ion chamber is aligned to the bottom edge of the cone and its central axis is perpendicular to the beam.

The X-ray unit is warmed up and a series of measurements were taken to stabilize the readings. Zero adjustment of the voltage was done by pushing the Reset button on High voltage power supply. The dosimeter specifications are as follows. The calibration constant of the dosimeter is 0.743 ± 0.011 Roentgens per volt. On the rate output, 1 V corresponds to a dose rate in air of 100 R / min. The exposure was measured for 1s irradiation with the ion chamber located at the

sample location and the dosimeter registered a maximum voltage of 1.43 V and a minimum voltage of 0.017 V. Thus, the radiation related output is 1.43 – 0.017 = 1.413 V and corresponds to 1.05 R. The mean dose rate in air should be 1.05 R / s. The dose rate was measured to be 6.73 V/min, which corresponds to 1.12 R/s.

The dosage rate is given by 10 V = 100 R/min and 1 V = 10 R/min and the calibration factor is 0.743±0.011 Roentgen/volt. During the exposure, the maximum voltage was measured to be 1.43 volts.

The actual dose, measured in grays is discussed in the following section

Typical Delivered Dose Calculation

The mass attenuation coefficient and energy absorption coefficient of Selenium for X-rays and gamma rays within the energy range from 1 keV to 20 MeV data are presented in Figure 3.12 (http://physics.nist.gov/PhysRefData/XrayMassCoef/ElemTab/z34.html; accessed September 20, 2015). The units of mass attenuation coefficient and energy absorption coefficient are cm^2/g as per NIST website.

First, we will do a reasonable estimate of the deposited dose as Grays per unit Roentgen exposure by assuming an average photon energy of E = 34.2 keV (discussed below) at which μ and μ_{en} are readily available.

The incident photon fluence Φ is

$$\Phi = \left[(-5.0233\times10^{-6}) + (1.8106\times10^{-7})\sqrt{34.2}\ln(34.2) + \frac{(0.0088387)}{(34.2)^2} \right]^{-1}$$

which gives Φ = 1.60×10 photons mm^{-2} mR^{-1} or 160×10^{10} photons cm^{-2} R^{-1}.

At E = 34.2 keV, μ/ρ = 11.0 cm^2/g and μ_{en}/ρ =8.08 cm^2/g, so that, taking ρ = 4.28 g cm^{-3}, we have μ = 47.2cm^{-1} and μ_{en} = 34.6 cm^{-1}. The quantum efficiency (fraction of photons attenuated within the thickness L) is

$$\eta_{QE} = 1 - \exp(-\mu L) = 1 - \exp[-(47.2\ cm^{-1})(200\times10^{-4}\ cm)] = 0.61$$

The actual energy deposited into a sample with 1 cm^2 area and 200 μm thickness is

$$E_{deposited} = \Phi E(\mu_{en}/\mu)\eta_{QE}$$

$= (1.60\times10^{10}$ photons $cm^{-2}\ R^{-1})(34200\ eV \times 1.6\times10^{-19}\ J/eV)(34.6/47.2)(0.61)$

$= 3.91\times10^{-5}\ J\ cm^{-2}\ R^{-1}$

The mass of a sample of area 1 cm^2 and thickness 200 μm is

M = density × volume $= (4.28\ g\ cm^{-3}) \times (200\times10^{-4}\ cm)(10^{-3}\ kg/g)$

$= 8.56\times10^{-5}\ kg\ cm^{-2}$

Therefore the mean deposited dose is

$D = E_{deposited} / M = 3.91\times10^{-5}\ J\ cm^{-2}\ R^{-1} / 8.56\times10^{-5}\ kg\ cm^{-2}$

that is

$D = 0.46\ Gy\ R^{-1}$

The above deposited dose is for the whole sample and represents the mean deposited dose at 34.2keV. The next step involves taking into account the x-ray spectrum and the distribution of photons in this spectrum.

We can view the incident x-ray spectrum as a probability distribution for photons. Let P_i in arbitrary relative units represent the magnitude of the probability of receiving at photons at a photon energy E_i. For example, P_1/P_2 is the probability ratio of photons at energies E_1 and E_2. We can divide the spectrum into N energy values from $i = 1$ to N. Normally the sum of all P_i should be 1 but because Pi is in arbitrary relative units, the sum is not unit.

Suppose that D_i is the deposited dose at energy E_i. Then, the average dose delivered over the spectrum E_1 to E_N is

$$D = \frac{\overline{E}_{absorbed}}{M} = \frac{\sum_1^N P_i D_i}{\sum_1^N P_i} = \frac{\sum_1^N P_i(E_i) D_i(E_i)}{\sum_1^N P_i(E_i)} \qquad 3.10$$

where $D_i(E_i)$ is the delivered dose calculated as in the above example for the photon energy E_i. The above example used $E_i = 34.2$ keV and we need to use a sufficient number of energy values in the spectrum to capture the effect of the spectrum on the dose.

The ideal W (tungsten) anode spectrum at 57 kVp was downloaded from the Seimens website and is shown in Figure 3.13. A 2 mm Al filtering was used and the ripple factor was set to 1 because the tube voltage is half rectified. The spectrum in Figure 3.11 with average energy 34.2 keV can be digitized as shown in Table 3.3, which has 22 points.

We can easily calculate the average energy in the spectrum by

$$\overline{E} = \frac{\sum_{1}^{N} E_i P_i(E_i)}{\sum_{1}^{N} P_i(E_i)} = 34.2 \text{ keV} \qquad 3.11$$

Table 3.3: Photon Energy vs Incident Photon fluence

E **(keV)**	**Incident photon fluence (Photons mm^{-2} keV^{-1})**	***E*** **Φ**
15	2.74E+06	4.11E+07
17	2.32E+07	3.94E+08
19	9.04E+07	1.72E+09
21	1.98E+08	4.16E+09
23	3.25E+08	7.48E+09
25	4.47E+08	1.12E+10
27	5.51E+08	1.49E+10
29	6.39E+08	1.85E+10
31	6.82E+08	2.11E+10
33	6.60E+08	2.18E+10
35	6.24E+08	2.18E+10
37	5.67E+08	2.10E+10
39	5.14E+08	2.00E+10
41	4.55E+08	1.87E+10
43	3.69E+08	1.59E+10
45	2.96E+08	1.33E+10
47	2.13E+08	1.00E+10
49	1.59E+08	7.80E+09
51	1.07E+08	5.48E+09
53	6.17E+07	3.27E+09
55	2.31E+07	1.27E+09
57	1.20E+06	6.84E+07
SUM	**7.01E+09**	**2.40E+11**

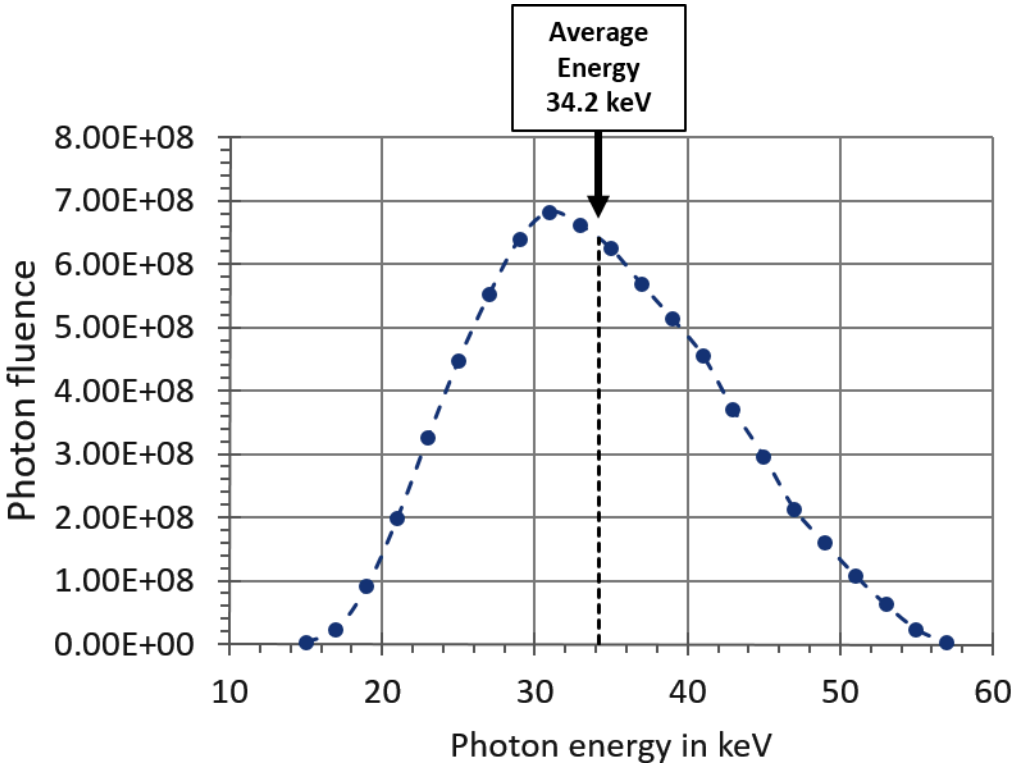

Figure 3.11: Digitized X-ray spectrum with average photon energy of 34.2 keV.

Table 3.4, summarizes the exposure and dose used in the present measurements. Ch4 will present the results on the dark current upon irradiation with x-rays. The irradiation period was 3s, and the a-Se samples were exposed to 3.15 R of radiation. 1.38 Gy of radiation energy was deposited into the samples.

Table 3.4: Exposure and dose used in current measurements

X-ray Quantity	**1 s**	**3 s**	**Comment**
Exposure in air	1.05 R	3.15 R	Direct measurement at the sample location
Exposure rate	1.12 R/s	1.12 R/s	Direct measurement at the sample location
Average photon energy	34.2 keV	34.2 keV	W-anode x-ray tube, 2mm Al filtering, halfwave rectified
Dose in 200 μm a-Se	0.46 Gy	1.38 Gy	Calculated using the x-ray spectrum

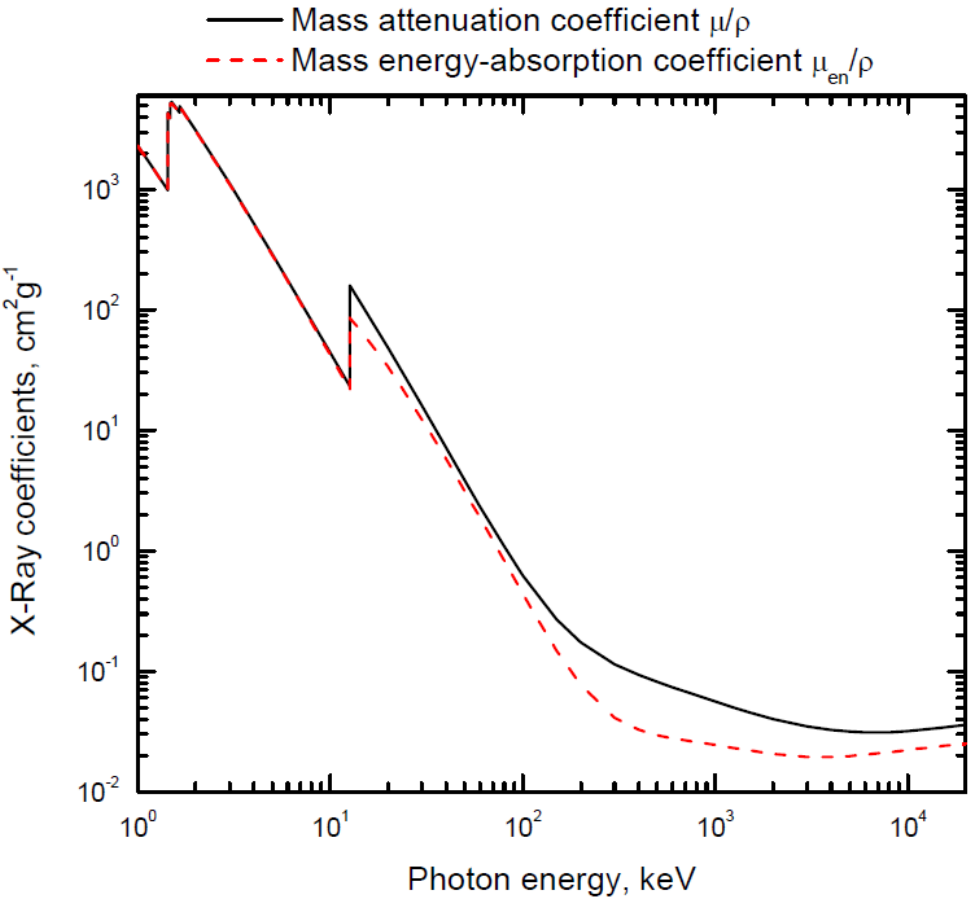

Figure 3.12: Mass attenuation coefficient and Mass energy absorption coefficient of Selenium of X-rays and gamma rays with energy range from 1 keV to 20 MeV. Data is taken from NIST website (http://physics.nist.gov/PhysRefData/XrayMassCoef/ElemTab/z34.html, accessed September 20, 2015)

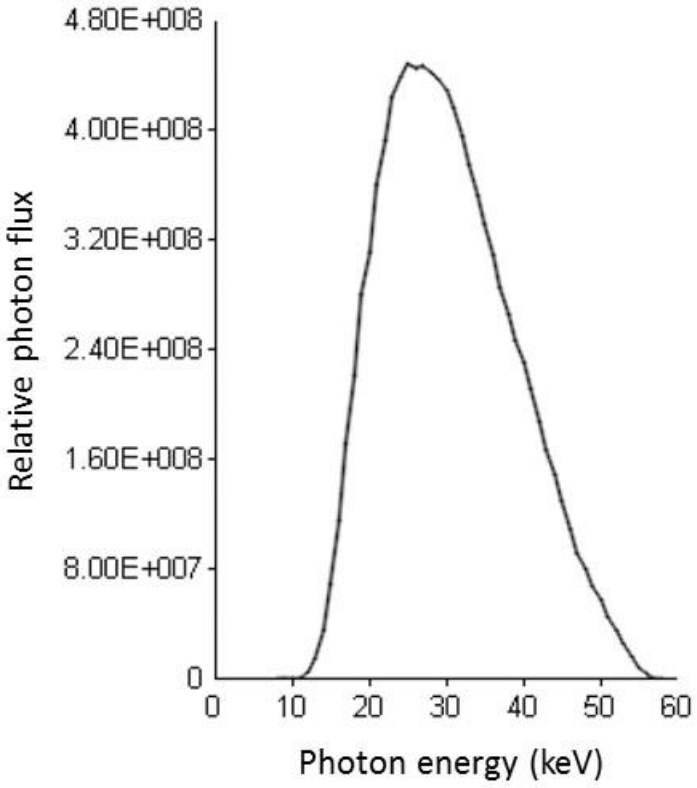

Figure 3.13: The X-ray spectrum of a W anode X-ray tube operating at 57 kVp with 2 mm Al filtering from http://www.oem-products.siemens.com/x-ray-spectra-simulation (December 16, 2015). The maximum voltage is set to 57 kVp, and the ripple is set to unity because the tube voltage in the Siemens x-ray unit is half-rectified.

3.7 Recording of Dark Current

The measurement of dark current, which is automated, can be seen in the transient recorder represented in Figure 3.14. Description of the sample and experimental sequence is given in the transient recorder and the real time dark current graph will be plotted in the Current task graph box. The progress of the experiment will be visually displayed in the transient recorder. Single X-ray irradiation on the sample can be readily automated in the transient recorder and the dark current measurements are recorded during and after the irradiation.

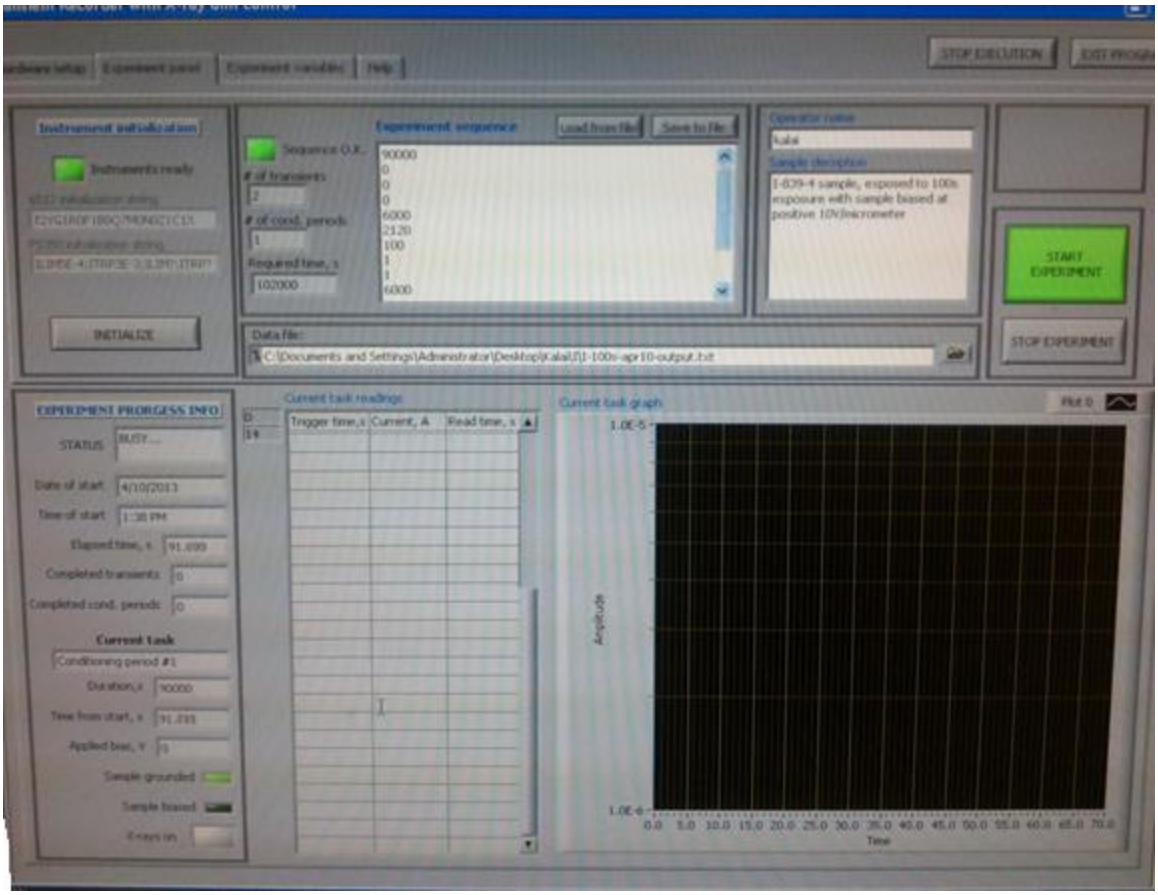

Figure 3.14: Transient Recorder in the computer system for measuring the dark current.

3.8 Control Experiments

Control experiments were earlier performed by Frey to indicate the impedance to an output transient in which the current flows in an opposite direction is implied by the polarity of the output voltage. A schematic representation of the fundamental control experiment is shown in Figure 3.15 in which the two voltage sources and the switch represents a step change in voltage supplied by a Stanford Power supply. The RC circuit in Figure 3.15 is built from discrete components and placed between the leads used for measuring dark current. The following values are used in this experimental, R_{int} = 10 M (electrometer internal resistance), R = 22 M, C = 1 µF, which results in a time constant τ of approximately 32s. The predicted waveforms are shown in the Figure 3.15b. When the capacitor charges to V_A, the input voltage switches to V_B, which results in a negative current as the voltage across the capacitor decreases to V_B. The charge accumulated in the area under the current graph in Figure 3.15b is

$$Q_{\mathrm{A}} = \int_0^{\infty} \frac{V_{\mathrm{A}}}{R_{\mathrm{tot}}} e^{\frac{-\mathrm{t}}{\mathrm{R_{tot}C}}} \mathrm{dt} = V_A C[1-0] = \mathrm{C}V_A \qquad 3.12$$

At t = 100 seconds the switch between V_{A} and V_{B} occurs with V_{A} = 40 V and V_{B} = 20 V [4].

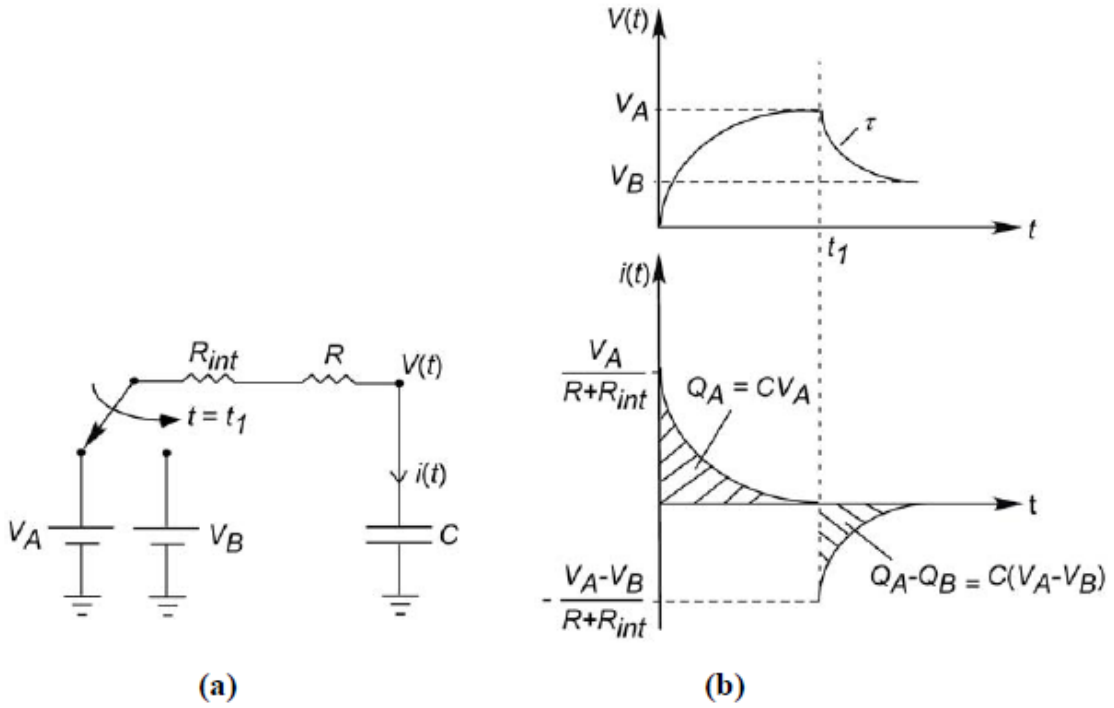

Figure 3.15: Diagrammatic representation of Current reversal control experiment. At time t = t_1, the applied voltage switches from higher voltage V_{A} to lower voltage V_B. Expected transient graph for voltage through the capacitor, V(t) and expected current, i(t) through the RC circuit [4]

Results for the control experiments with expected and observed charges are given in Table 3.5 below.

Table 3.5: Expected and Observed charges. The observed charges were calculated using Matlab, setting the initial values to zero [After Frey 4].

Parameter	Expected	Observed
i_1	1.25 µA	1.07 µA
i_2	0.625 µA	0.57 µA
τ	32s	35s
Q_A	4 x 10^{-5} C	3.3 x 10^{-5} C
$Q_A - Q_B$	2 x 10^{-5} C	1.7 x 10^{-5} C

The electrometer used in these experiments is capable of measuring the data points approximately 2s after the applied bias voltage. Therefore, the measurements performed in the voltage step experiments and discharge experiments are not related to the response time of the power supply transients or transients due to RC time constant of the sample which is approximately 3ms.

3.9 Step Voltage Measurements

The voltage step measurement experiments were performed by Frey for a *p-i-n* sample from Set A. Different multiples of field were applied across the sample and the dark current for each applied field was measured during a given time interval. When a negative $-0.625\ V\mu m^{-1}$ was applied across the sample, at t = 0s, it resulted in a dark current transient for 1000s, falling by an order of magnitude and reached a plateau at approximately 2×10^{-3} pA mm^{-2}. When t = 1000s, the applied field was doubled to $-1.25\ V\mu m^{-1}$. However, the dark current value did not go further than for the applied field of $-0.625\ V\mu m^{-1}$. This might be due to the trapped charge carriers arising from the previously applied field, which has created a built-in electric field that opposes the $-1.25V\ \mu m^{-1}$ applied field. But, this effect is not seen at t = 2000, 3000 and 4000s as the change in the applied field is greater than that generated by the space charge in the sample. When the applied field is increased at smaller steps, for example 1.5 times of the initial voltage, the effect is more convincing as current density peaks are seen below the first peak (Figure 3.16).

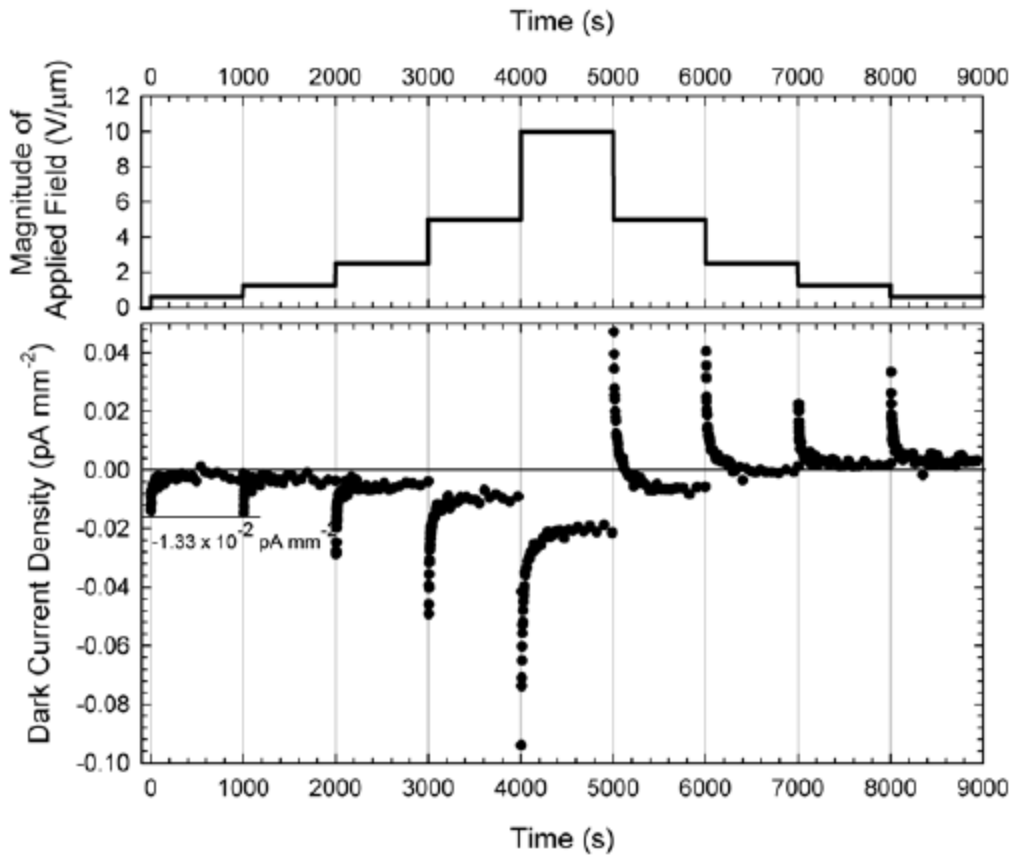

Figure 3.16: Dark current density for a *p-i-n* sample from sample set A for step wise applied voltage changes. At 1000 s, with 2 times the applied voltage the peak value of current density is equal to that of t = 0s. With the application of step down voltage after 5000s, the current density spikes are in the opposite direction [4].

When the applied voltage to the *p-i-n* sample is reduced in steps, the current density peaks are in the opposite direction after 5000s. These effects can be seen in Figure 3.16 and they are due to the space charge built-up in the sample which leads to the reversal of current in a very shorter time frame [4].

The above mentioned results agree with Simmons and Taylor's prediction for defective insulators. These insulators have very deep trap states with a depth between 0.5 eV to 1 eV[54]. The fundamental features of the current density are due to the release of the trapped holes. The electrons are deeply trapped and they take longer to be released than holes. This can be noticed in Figure 3.16 during the time t = 7000s and 8000s, a quasi-steady state is present, which is due to the trapped electrons and will not be released for a longer time.

Similar experiment was performed for the *i*–sample and the current density was monitored with applied step up and step down voltages. Representation of applied voltages and the resultant current density is given in Figure 3.17. A second current density peak that is lower than the first was absent in *i*-layer sample for increasing step up voltages. During 7000s and 8000s a small peak can be seen in the positive direction when the applied bias was step down. Experiments performed in *p-i* and *i-n* samples from the set A showed results specifying the amount of charge stored greater than the i-layer but less than the *p-i-n* layer. This observation is expected since *p-i* and *n-i* layers have blocking layers that trap charges.

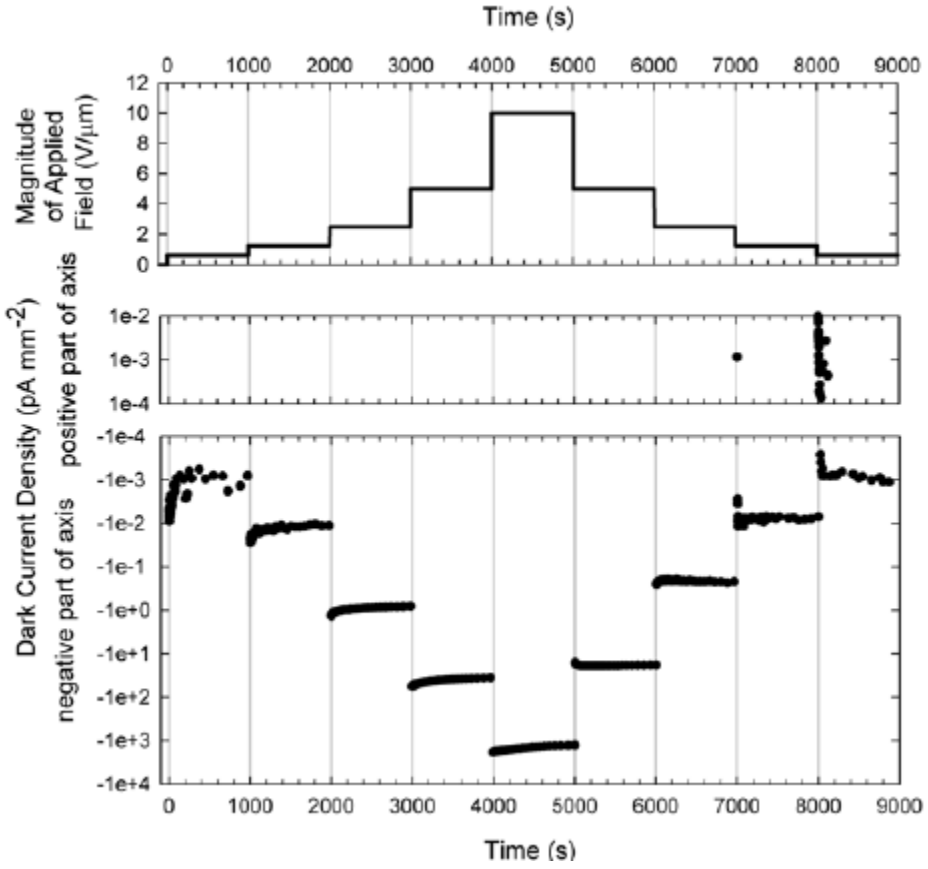

Figure 3.17: Dark current density for *i*-layer sample from Set A with respect to the step wise change in applied voltage.

As the *p-i-n* layer has 2 blocking layers, more charge carriers are trapped in the blocking layers and the peak is more noticeable in Figure 3.16. This result indicates that much more charge carriers are trapped in the blocking layers than the *i*-layer sample. The charges trapped in the

blocking layers are conducive to create a potential or an internal field in the opposition to the applied field [4]

3.10 Summary

In this chapter, the experimental procedures used throughout the course of this work were discussed. The samples used to measure the dark current were prepared by a conventional vacuum deposition technique. A Keithley programmable electrometer and high voltage power supply were used to bias the sample and measure the small current transients. Automated measurements of the dark current is outlined and various control experimental are reported, including measurements of current in a well-defined *RC* circuit. Seimens Heliodentic X-ray tube was used to irradiate the samples. A Keithley dosimeter and ion chamber were used to measure the amount of X-ray exposure the sample receives. An X-ray exposure corresponding to 1.12 R/s was incident on a typical sample for approximately 3s. Step voltage measurements and control experiments are also outlined in this chapter.

CHAPTER 4. RESULTS AND DISCUSSION

4.1 Introduction

This section reports the experimental results of dark current for various structures of amorphous selenium samples under no x-ray exposure, single exposure and multiple exposures. The irradiation experiments and experiments with no exposure were performed under different applied bias voltages. The time evolution of the dark current was measured for the samples with various reverse bias voltages such as 12V μm^{-1}, 10 V μm^{-1}, 5 V μm^{-1} and 1 V μm^{-1} and over different time periods

The changes in the dark current by exposing the single layer and multi layered a-Se samples to x-ray irradiation will be reported and discussed in the following sections. The purpose of this study is to identify the changes in the behavior of the dark current (such as the time evolution of the dark current) caused by x-ray exposure on each type of a-Se detector structure

4.2 Dark Current after Different Resting Periods

Introduction

To find the least value of dark current after different resting periods, a 3 layered amorphous Selenium sample was tested. It is very important to rest the sample as the sample can take a long time to relax and release all the trapped charges. In a-Se, electrons have a release time in the order of thousands of s. The results of dark current with different resting periods are measured and presented in this section.

Experimental Results and Discussion

The experiment to measure the dark current without exposure on the sample was repeated three times to find the lowest value of the dark current. The experiment was repeated by placing the sample in light-proof chamber for different resting periods such as 8 hours, 12 hours and 24 hours and dark current decay after each resting period is recorded. Typical results are shown in Figure 4.1 for an *n-i-p* type a-Se sample. The sample was reverse biased to achieve a nominal field of 10 Vμm^{-1}. Figure 4.1 represents the dark current decay of an *n-i-p* sample with the platinum contact biased at positive 10V/μm.

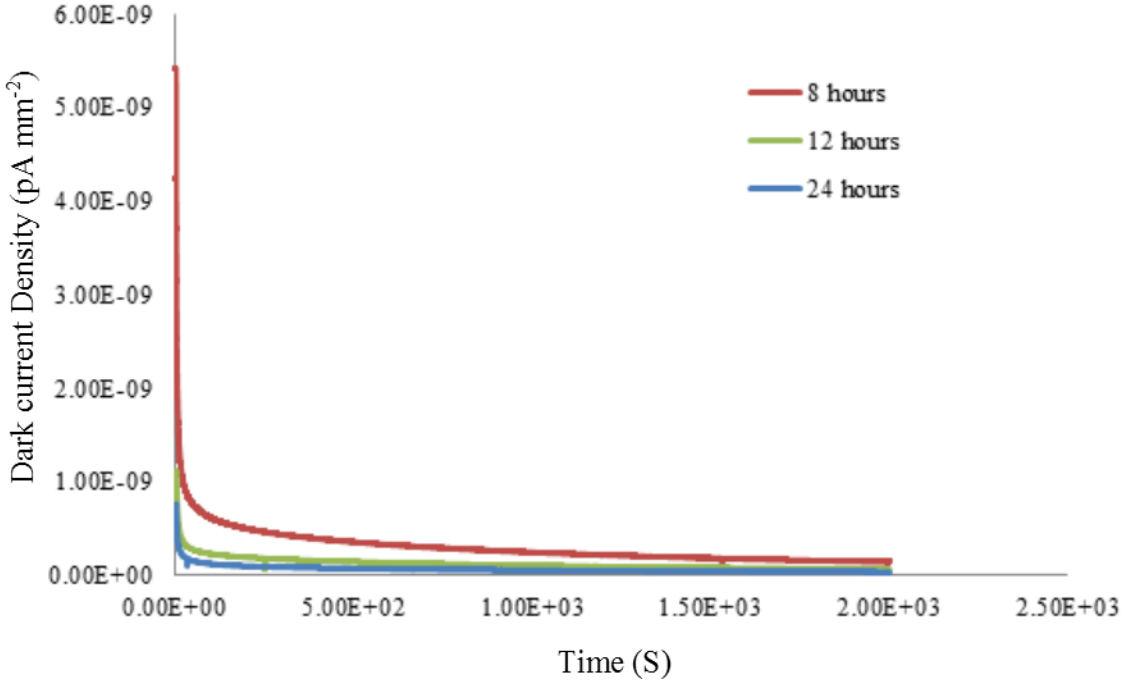

Figure 4.1: Dark current decay of an *n-i-p* sample biased at 10V μm^{-1}. Measurements were taken after resting the sample for different periods, 8 hours, 12 hours and 24 hours to illustrate the need for adequate dark rest between measurements.

From the Figure 4.1 it is clearly seen that dark current for the sample after resting for 8 hours has a value that is 1 order of magnitude greater than the dark current of the sample rested for 24 hours. Resting the sample for a long time will result in the so-called "relaxation" of the sample in which trapped charges are released so that the bulk space charge in the sample is eliminated. Trapped electrons in the a-Se sample will take a much longer time to become released, compared to the holes, as the Electron traps are deeper than hole traps [41]

Consider the *n-i-p* a-Se device as apparent from Figure 4.1 a longer resting period of the sample in the dark, results in a smaller dark current. From the plot, there is a significant difference seen in dark current measured when the sample was rested for 8 hours and 24 hours. Based on the above experimental measurements, experiments on all other samples were performed by resting the sample for at least 24 hours to get a low value of dark current.

The dark current measured after resting the sample for 8 hours and 24 hours begin to merge around 2000s after the application of the bias voltage as can be seen in the Figure 4.1. The reason

is that over a long period, the initial bulk space charge is no longer important because the accumulated trapped charge in the bulk brought in by the current becomes significant, and comparable in both cases. As we are interested in the initial dark current after x-ray exposure, the dark current measurements were all performed with a 24 hour rest period between applications of voltage. Such a resting period allows a meaningful comparison of the effects of x-ray exposure without any artifacts arising from insufficient resting of the sample, which would result in some unreleased bulk space charge.

4.3 Dark Current as a Function of Sample Structure

Experimental Results and Discussion

Several experiments have been performed earlier to measure the reduced dark current in various amorphous selenium structures. In this section, experimental proof will be provided to find the least value of dark current as a function of sample structure with applied reverse bias voltages such that the nominal field is comparable between samples.

Measurements were taken on the sample set A for samples *i-*, *p-i* , *n-i* and *p-i-n* and the sample set C for sample *n-i-p* with the same experimental set up as mentioned in Section 4.2. The samples were rested for 24 hours previously before the start of the experiments so that the trapped charges will be released.

From the previous research [3],[18] and the current measurements taken, it is well noticed that dark current in a-Se sandwich structures decays monotonically with time and this can be seen in Figure 4.2. The measurements were taken up to 2000 s with applied field of 10V μm^{-1} for all the samples.

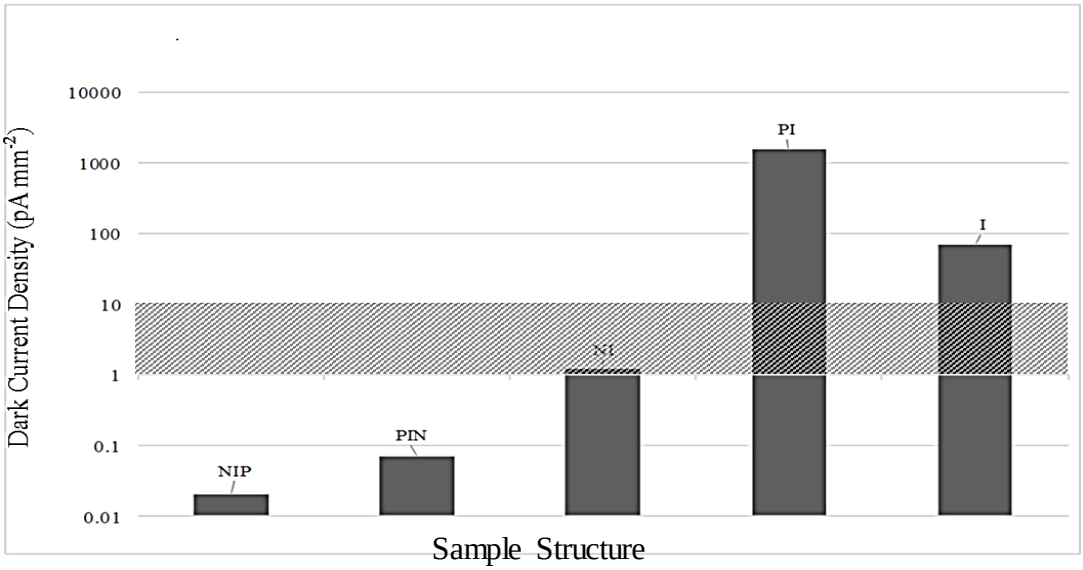

Figure 4.2: Comparison of the magnitude of dark current level at 300s after the application of field 10V μm^{-1} for sample structures *p-i* , *n-i-p*, *n-i*, *p-i-n* and *i*- when the samples are not radiated. The acceptable level of dark current is given by the hashed area. The samples having *n*-layer has produced dark current below the acceptable range

Figure 4.2 shows the comparison bar graph for the dark currents measured in different multilayer sample structures with an applied field of 10V μm^{-1}. Note that a reverse bias voltage is applied to both the *n-i-p* and *p-i-n* structure which means a positive voltage on the electrode on the *n*-side of *n-i-p* and negative voltage on the electrode on the *p*-side of *p-i-n*. It is clear from Figure 4.2 that the addition of both blocking layers in the *p-i* -n and *n-i-p* structures has resulted in a much less dark current compared to the *n-i* and *p-i* structures.

The addition of 2 μm thick p-like layer next to the negative top electrode in *p-i* sample does not have any effect on the dark current (Figure 4.2). The p-layer essentially traps electrons and reduced the field at the negative electrode and hence reduces the electron injection. In a-Se, the holes have a much higher drift mobility than electrons so the actual contribution of electrons to the full current is less important than holes. Thus, the insertion of a p-layer between the *i*-layer and the negative electrode reduces the injection of electrons but this is not sufficient to reduce the dark current significantly [3]. A significant reduction in the dark current can only be achieved by limiting the injection of holes from the positive electrode. From Figure 4.1 and Figure 4.2 it is observed that *n-i-p* sample structure has the lower limit of dark current after 2000s of decay with an applied field of 10V μm^{-1}. This small dark current is within the acceptable level of dark

currents for a detector operation [10] . This is achieved due to the addition of *p*- type and *n*-type blocking layers.

It can also be seen that the addition of a thin *p*-layer in both the *n-i-p* and *p-i-n* family has a very little effect on the transient and the *n*-layer plays major role in blocking the injection of holes and it supports the theory that the dark current in metal/a-Se/ITO structures is mainly due to the conduction of holes. The *n*-layer in the *n-i-p* multilayer structure is 6 µm thick and it blocks the injection of holes and reduces the dark current level by more than 3 orders magnitude compared to the *p-i* structure where there is just a 2 µm *p*-layer to block the electrons and no *n*-layer to block the holes.

Continued reduction in the dark current can be seen by increasing the complexity of the structure from *n-i* or *p-i* to *n-i-p* and *p-i-n* and this is well represented in the Figure 4.2 showing reduced dark currents for *n-i-p* and *p-i-n* structures. The dark currents in *n-i* structures are significantly lower than those in *p-i* structures but the lowest dark current are in *n-i-p* and *p-i-n* layers. This is probably due to the fact that there is no layer to trap the electrons in the *n-i* layer and the electrons can make a contribution to the dark current.

The *n-i-p* sample with a aluminum contact has resulted in the lowest value of dark current compared to other sample structures. This is due to presence of blocking layers *p*-layer and *n*-layer which are appropriately doped to serve as unipolar conducting layers that can easily trap electrons and holes, but allow the transport of oppositely charged carriers.

The multilayered sample structures *p-i-n* and *n-i-p* with metallic contacts have produced lesser dark current compared to single layer and two layered structures. Therefore, the presence of both *p*-layer and *n*-layer has an important effect on the dark current in a-Se detectors. In the next section, a model will be provided to explain the observations.

Electric Field Distribution across the Sample

This section provides an explanation of the model that can be used to explain the dark current in multilayer a-Se structures. The basic assumptions are the following. The *p*-layer traps injected electrons, which then blocks the further injection of electrons from the negative electrode. The *n*-layer traps the injected holes and blocks the further injection of holes from the positive electrode. Trapped charges modify the fields within the device and at the contacts and control F_1 and F_2,

which is illustrated in the Figure 4.3. The electric field is related to the space charge density by Poisson's equation

$$\frac{dF(x)}{dx} = \frac{\rho(x)}{\varepsilon_0 \varepsilon_r} \quad 4.1$$

in which ρ is the space charge density due to the trapped carriers, ε_r is the relative electric permittivity and ε_0 is the permittivity of vacuum.

Solving the above equation with the boundary condition

$$\int_0^L F(x)dx = V \quad 4.2$$

where V is the applied bias voltage and L is the thickness of the sample.

Assuming the trapped carrier densities in the blocking layers are uniform Equation 4.1 and 4.2 can be solved analytically to obtain the instantaneous electric field at the contacts as

$$F_1 = F_0 - \frac{e}{\varepsilon_0 \varepsilon_r}\left[\left(L_n - \frac{L_n^2}{2L}\right)p_{\mathrm{tn}} - \frac{L_p^2}{2L} n_{\mathrm{tp}}\right] \quad 4.3$$

$$F_2 = F_0 - \frac{e}{\varepsilon_0 \varepsilon_r}\left[-\frac{L_p^2}{2L} p_{\mathrm{tn}} + \left(L_{\mathrm{p}} - \frac{L_p^2}{2L}\right)n_{\mathrm{tp}}\right] \quad 4.4$$

where F_1 is the instantaneous electric field at the positive contact, F_2 is the electric field at the negative contact, F_0 is the applied electric field (the so-called nominal field), p_{tn} is the trapped hole concentration at the *n*-layer, n_{tp} is the trapped electron concentration at the *p*-layer, and $L_p$and L_n are the thicknesses of the blocking *p*- and *n*- layers and ε_0 is the permittivity of free space and ε_r is the relative permittivity of amorphous Selenium

The rate of change of deeply trapped hole and electron concentrations is given by the following rate equation

$$\frac{dp_t(t)}{dt} = C_{\mathrm{th}} N_{\mathrm{th}} \theta_h \left(1 - \frac{p_t(t)}{N_{\mathrm{th}}}\right) p(t) - \frac{p_t(t)}{\tau_{\mathrm{rh}}} \quad 4.5$$

$$\frac{dn_t(t)}{dt} = C_{\text{te}} N_{\text{te}} \theta_e \left(1 - \frac{n_t(t)}{N_{\text{te}}}\right) n(t) - \frac{n_t(t)}{\tau_{\text{re}}} \qquad 4.6$$

where N_{th} is the deep hole concentration in the *n*-layer and N_{te} is the deep electron concentration in the *p*-layer, C_t is the deep trapping coefficient and θ is the ratio of effective drift mobility in the presence of shallow traps. These equations include the effect of deep trap filling with time and trap release. τ_r is the release time of a trapped electron or hole from a trap depth of E_t and it is given as

$$\tau_r = \frac{1}{v_0} \exp\left(\frac{E_t}{kT}\right) \qquad 4.7$$

Here v_0 is the attempt to escape frequency. v_0 is related to N_v and C_{th} by $v_0 = N_v C_{\text{th}}$

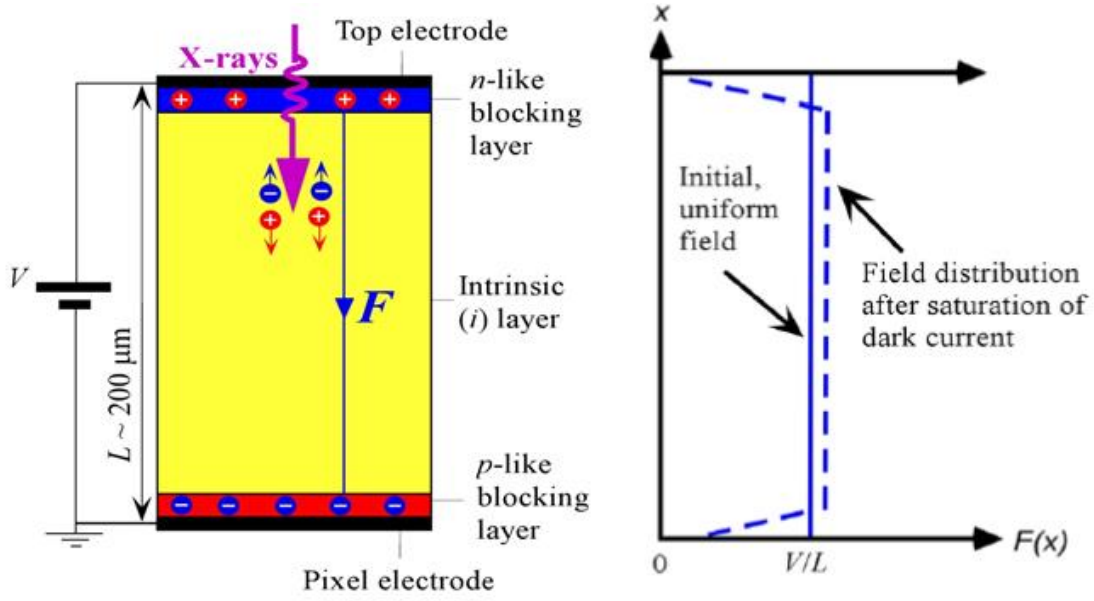

Figure 4.3: Simplified cross-section of a *n-i-p* multilayer amorphous selenium sample. The injected charge carriers due to the applied bias voltage are trapped in the blocking *n*-layer and *p*-layer. Therefore, the field distribution decreases at the blocking contacts but remains constant in the intrinsic layer. Drawing not to scale. From [55]

The field at both the positive and negative contacts gets reduced due to the trapped holes in the *n*-layer, and electrons in the *p*-layer as shown in Figure 4.3. Equations 4.3 and 4.4 can be used to calculate the field at the positive contact and negative contact. As the carriers are trapped in the blocking layers, the interactions in the *i*-layer are therefore p_{ti} and n_{ti} are 0. If the fields at the contacts are known, the total current due to the injection of holes and electrons can be calculated by using Equation (4.8)

$$J_{\text{tot}} = J_h + J_e = e\mu_h F_1 N_{\text{v}} \exp\left(-\frac{\varphi_h - \beta_s\sqrt{F_1}}{kT}\right) + e\mu_{\text{e}} F_2 N_{\text{c}} \exp\left(-\frac{\varphi_e - \beta_s\sqrt{F_2}}{kT}\right) \quad 4.8$$

4.4 Discharge Measurements

Background

Space charge is built up in the a–Se layer during the flow of dark current. The current flows through the sample in the opposite direction when the applied bias is removed. The reasons for this flow of current is identified and discussed in this section. Discharge transients can be measured by short-circuiting the sample through a current-limiting resistance.

Experimental Results and Discussion

Following the measurements in Section 4.3, the a-Se sample is short-circuited through a current – limiting resistance for 2000s and the resulting current is measured. This measurement was taken for the samples *p-i-n, p-i, i-, n-i* in sample set A and the sample *n-i-p* in sample set C. The current measured flows in the opposite direction. The graphical representation for the measurements taken for *p-i-n* sample under reverse bias condition, and short-circuited condition is shown in the Figure 4.4.

Following the dark current measurement with the application of voltage, dark discharge current in the opposite direction due to short-circuiting the sample is measured. This discharge current in the *p-i-n* sample is due to the injected electrons that are trapped in the *p*-layer and injected holes that are trapped in the *n*-layer which is similar to the way storing of charge built up in the plates of a parallel plate capacitor. This discharge current is at lower level of the preceding dark current. The dark current transient measured at 10V μm^{-1} applied across the sample for 3000s and the corresponding discharge transient are represented in Figure 4.4.

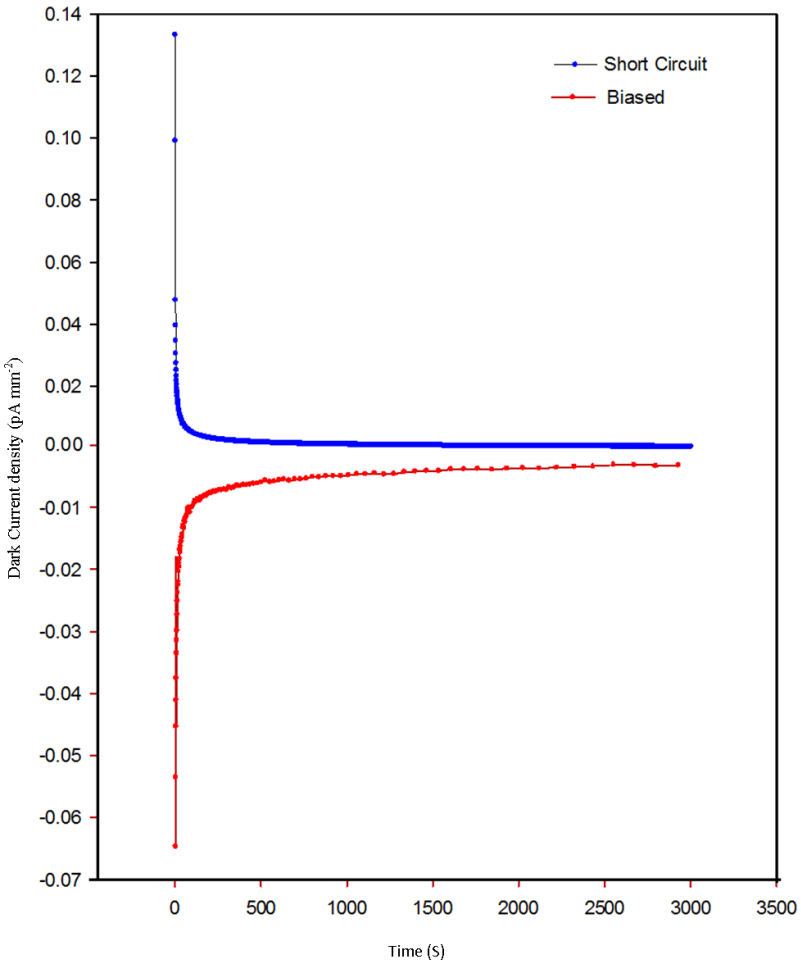

Figure 4.4: Dark discharge under short –circuited condition and biased condition.

Frey, in his research has taken this analysis to the next level by integrating the discharge currents to find the amount of charge released by using the numerical calculations in Matlab by setting the initial value of dark current to '0'. The baseline measurements were taken by resting the sample for 12 hours and observing the dark current from the sample without the application of bias for another 12 hours. The observed signal was noisy between 0.1 and 0.01 pA. Discharge current measurements can be continued for up to 12 hours following the short-circuited condition, and providing a continued decay below the baseline value.

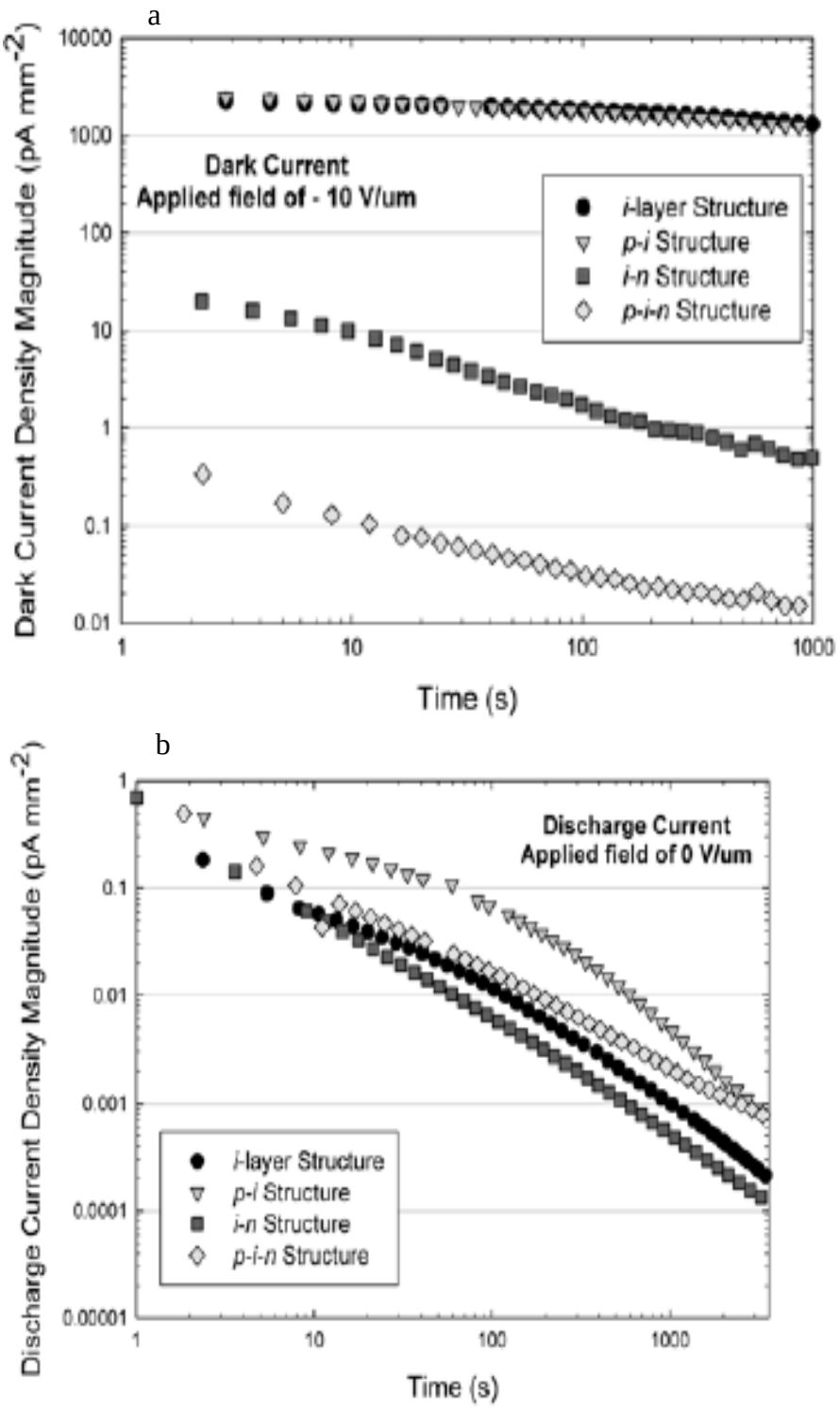

Figure 4.5: a) Measurement of dark current density for the *p-i-n* family under applied bias of -10V μm^{-1}. b) Discharge current density for the *p-i-n* family under short-circuited condition After Frey [3].

The dark current density and discharge current density for the *p-i-n* family is represented in Figure 4.5 a and b, respectively. It has been discussed that the discharge current density does not depend on the thickness of the *i*-layer but depends on the thicknesses of the *n*- and *p*-layers [55]. It was demonstrated that the dark current is limited by the injection of carriers at the electrodes, which is controlled by the fields at the contacts as in Equation (4.8)

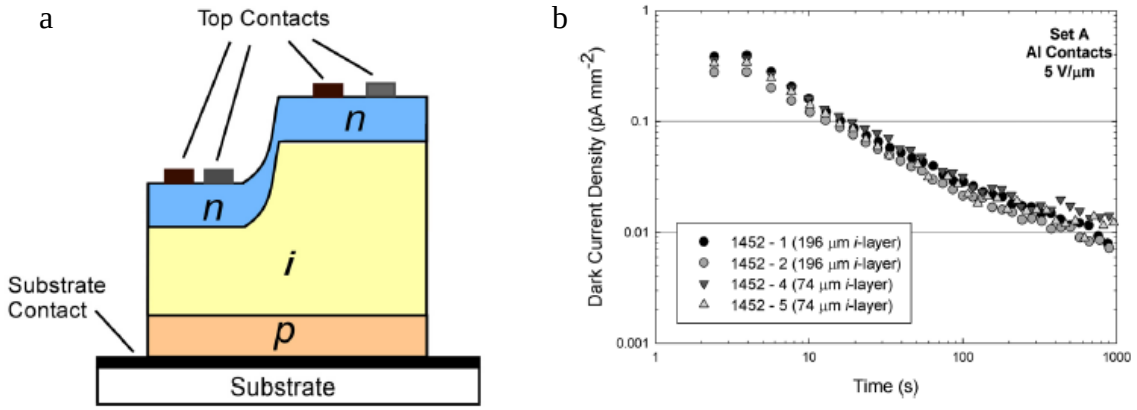

Figure 4.6 a) Schematic representation of a *n-i-p* 1452-1 sample. The *i*-layer has two distinct regions of thickness while the *n*-layer is as uniform as possible across the entire sample. The sample has two top contacts, one of Al and one of Pt. Drawing is not to scale [55]; b) Dark current transients for four different samples with different *i*-layer with Al contacts biased at 5V µm-1. At 1000s dark current decay has reached 2 orders of magnitude without reaching a steady state [55]

In Figure 4.6a, the dark current transients observed are right on top of each other and therefore it demonstrates that the contribution to the dark current of thermal generated carriers in the bulk of *n-i-p* structured sample is indeed negligible. It can be seen that the carrier injection from the contacts is the dominant source of dark current.

The schematic illustration of charge stored in each sample in set A and set C is given in Figure 4.7, redrawn from [3]; the location of the charges stored in different sample structures can be seen in this figure. In all these sample structures, there is equal amount of charge stored, but at different locations. By assuming that the trapped holes are twice as that of electrons, as an equal number of trapped carriers, trapped evenly throughout the sample. In case of *i-layer*, the trapped carrier concentrations in this layer would be small (both holes and electrons drift in the layer) and one can

take the *i*-layer as relatively neutral compared with the *n*- and *p*-layers. Further, there will be some cancellation of negative and positive trapped charges in the bulk but the main argument is weak trapping of carriers in this layer.

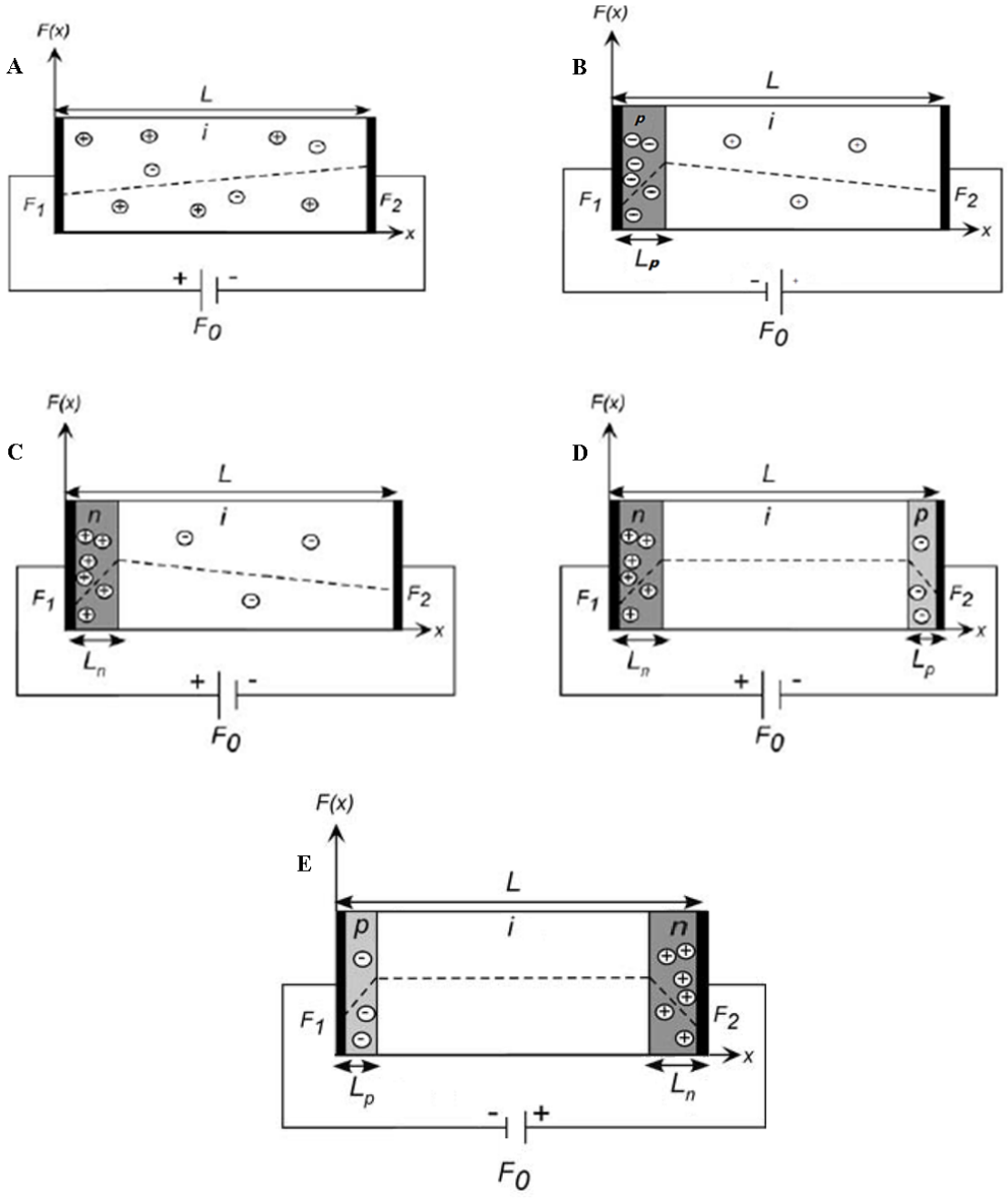

Figure 4.7: Representation of built up space charge layers (a) *i*-layer with electrons and holes uniformly trapped, (b) a *p*-*i* sample with electrons trapped in the *p*-layer and holes in the intrinsic layer, (c) a *n*-*i* sample with holes trapped in the *n*-layer and electrons in the *i*-layer, (d) a *n*-*i*-*p* sample with holes trapped in the *n*-layer and electrons trapped in the *p*-layer. The amount of

charge stored in each sample is same, but the charge location has fluctuating effect on the electric field at the contacts Redrawn from [3].

4.5 Single X-ray Irradiation

Background

Some changes in the dark current due to the effects of x-ray irradiation on a-Se structures have been discussed in previous papers. In this section we have reported our basic observation that the irradiation of an a-Se detector with x-rays leads to higher dark current. However, the change in the dark current is not permanent, and the detector reverts back to its normal dark current after a suitable rest time in the dark.

Experimental Results and Discussion

The samples *p-i, n-i, p-i-n,* from sample set A and *n-i-p* sample from the sample set C were examined. The sample under investigation is irradiated for a duration of 3s at different time periods. Dark current measurements were taken for the samples after a resting period of 24 hours and with the application of bias to yield a field of 10V μm^{-1}, the samples were exposed to radiation at 100s and 400s separately. The graphical representation of dark current produced by each of the samples *p-i, n-i, p-i -n and n-i-p s*tructures can be seen in Figure 4.8 up to Figure 4.12. The decay of dark current was monitored up to 2000s.

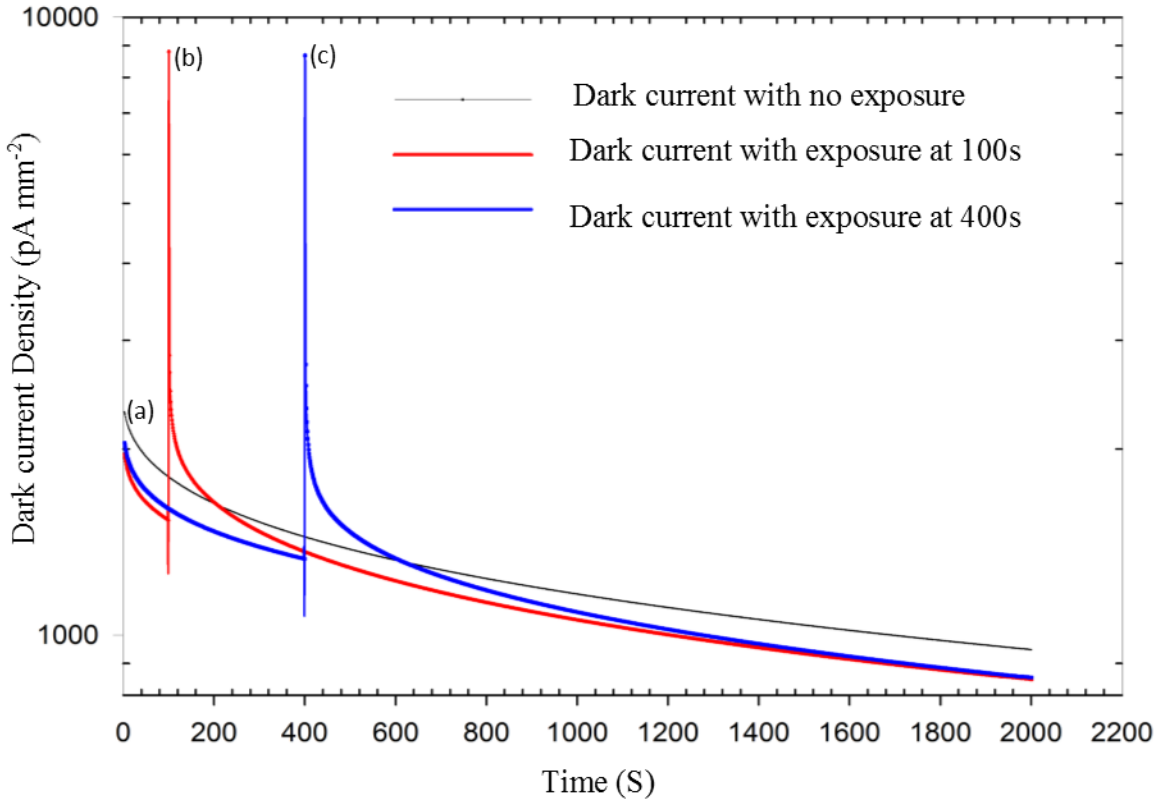

Figure 4.8: Measurement of dark current in *p-i* sample 842-1, from sample set A, with a chromium contact. The sample is irradiated at 100s and 400s and the rise of photocurrent due to the x-rays can be seen in the figure. (a) Dark current transient with no x-ray exposure. (b) Photo current peak at 100s (c) Photo current peak at 400s during x-ray irradiation. The applied field is 10V μm^{-1}.

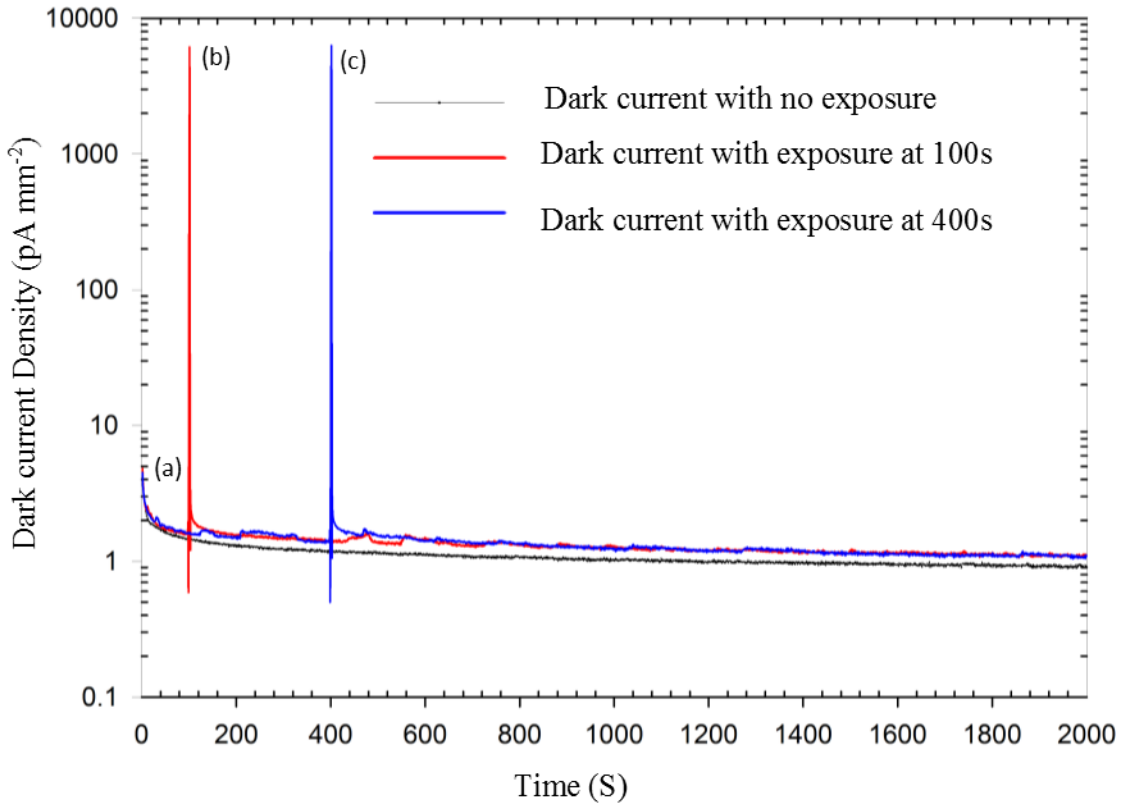

Figure 4.9: Measurement of dark current in *n-i* sample 847-2, sample set A, with chromium contact. The sample is irradiated at 100s and 400s and the rise of photocurrent due to the x-rays can be seen in the figure. Applied field is 10V μm^{-1}. The measurement is taken over a linear time scale (a) Dark current transient when the sample is not exposed to x-rays. (b) Dark current transient when the sample is exposed at 100s (c) Dark current transient when the sample is exposed at 400s. Transients with exposure at 100s and 400s merge from the beginning but there is a difference of less than 1 pA between the transients with exposure and no exposure.

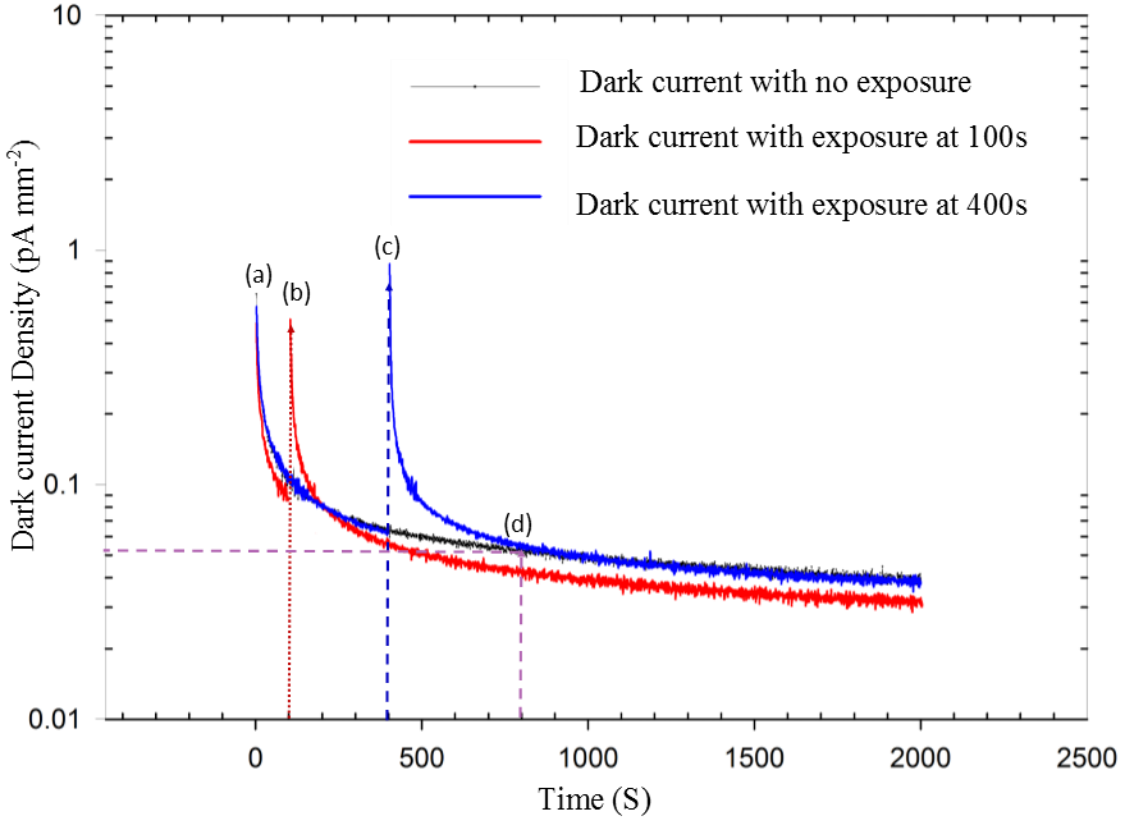

Figure 4.10 : Measurement of dark current in the *p-i-n* sample 850-1, sample set A, with a chromium contact. The sample is irradiated at 100s and 400s and the rise of photocurrent due to x-rays can be seen. Applied field is $10V\mu m^{-1}$. Measurement is taken over a linear time scale. (a) Dark current transient with no exposure (b) Dark current transient when the sample is exposed at 100s (c) Dark current transient when the sample is exposed at 400s. (d) At point d, approximately at 780s, the dark current transient with exposure at 400s merges with the transient with no exposure.

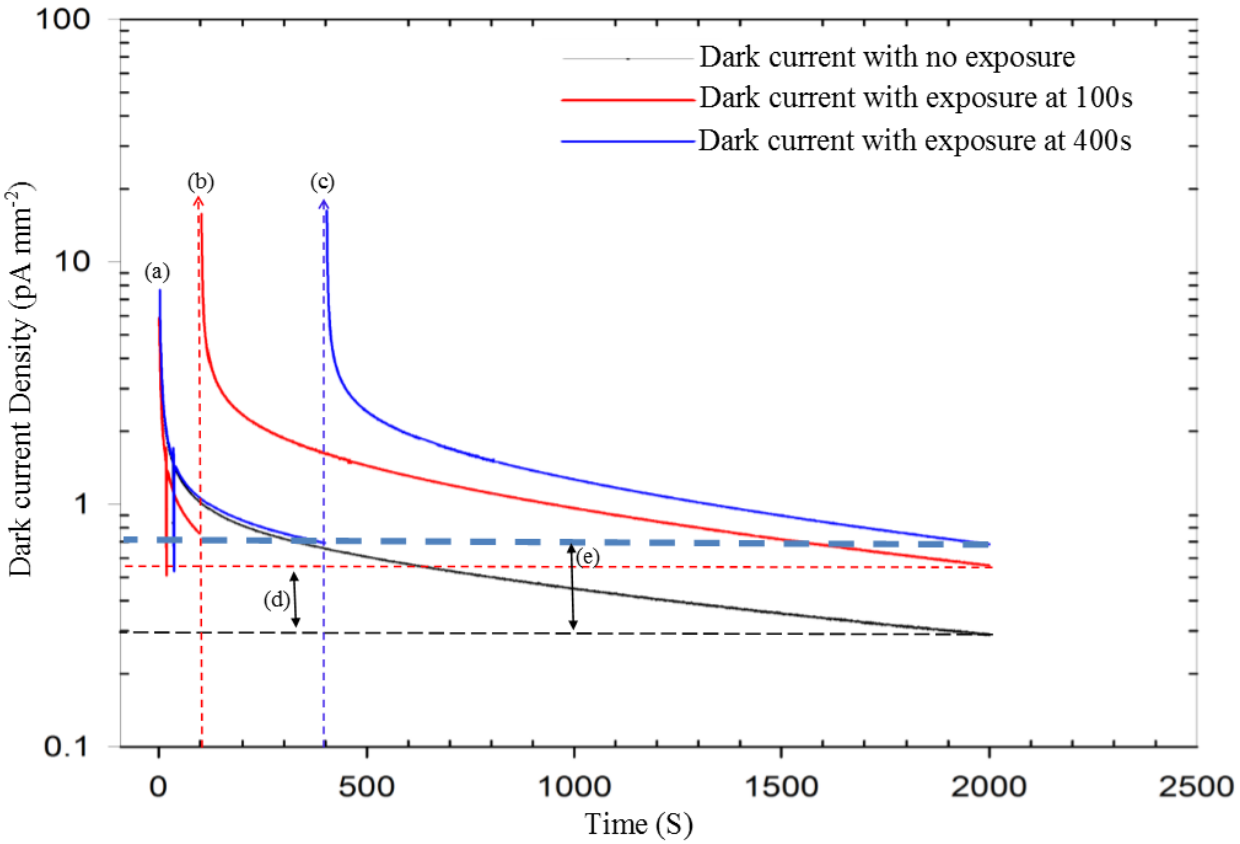

Figure 4.11: 1452-1 *n-i-p* sample with an aluminum contact exposed to radiation at 100s and 400s. Applied field is 10V μm^{-1} and the dark current decay measurements were taken for 2000s. (a) Dark current transient with no exposure (b) Dark current transient when the sample is exposed at 100s (c) Dark current transient when the sample is exposed at 400s. (d) At 2000s difference of 2.5 pA can be seen between the transients with no exposure and dark current transient with 100s exposure. At 2000s, difference of 3.5 pA can be seen between the transients with no exposure and dark current transient with 400second exposure

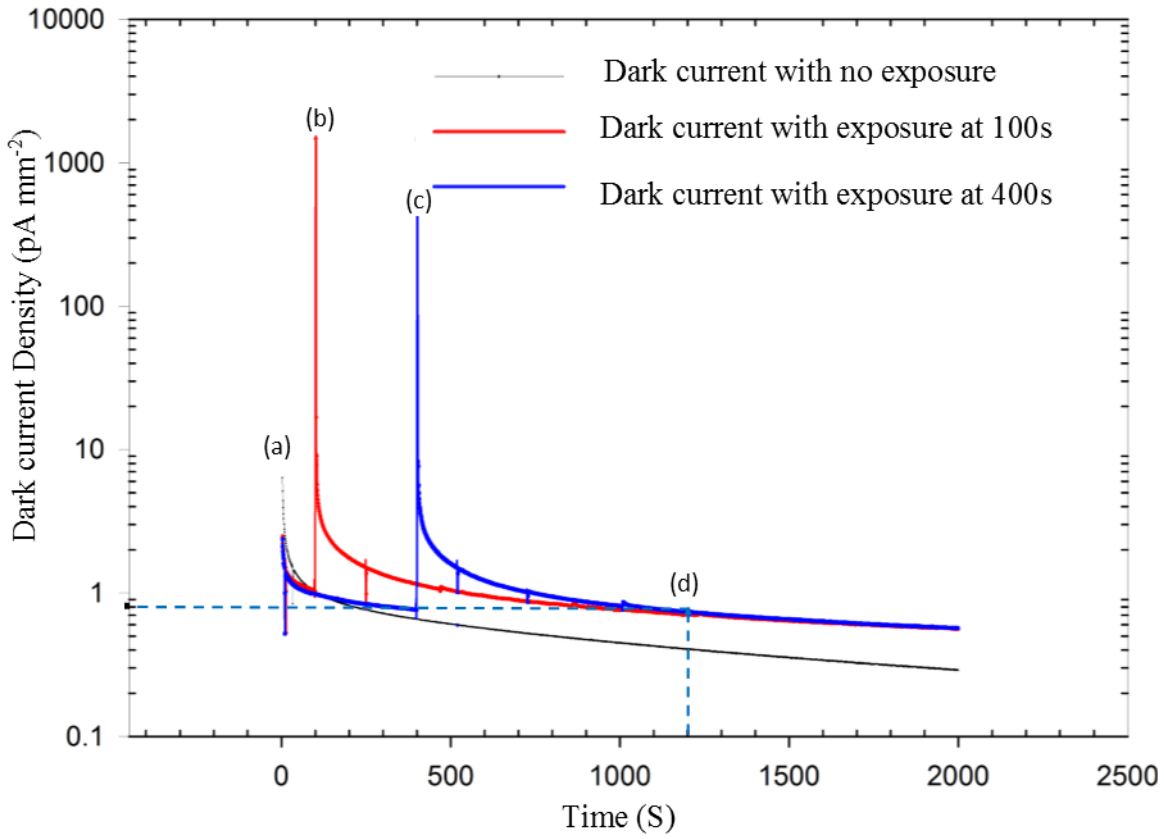

Figure 4.12: 1452-1, *n-i-p* sample with a platinum contact exposed to x-ray radiation at 100s and 400s respectively. Applied field to the sample is 10V μm^{-1} and the dark current decay measurements were taken for 2000s. (a) Dark current transient with no exposure (b) Dark current transient when the sample is exposed at 100s (c) Dark current transient when the sample is exposed at 400s. (d) At point approximately at 1200s the dark current transient with exposure at 400s merges with the transient with exposure at 100s. However, the dark current is still higher than that without exposure.

In all the figures illustrated in Section 4.5, the dark current immediately after the irradiation is large but it decays towards the normal value of the dark current in the unexposed sample. At 2000s, the dark current measured in the second cycle (exposure at 100s) and third cycle (exposure at 400s) does not reach the value of dark current measured in the first cycle. This is due to the fact that the x-ray generated charge carriers during the irradiation at 100s and 400s did not completely leave the sample or did not completely recombine and therefore the sample did not reach the same state as it is present in the first cycle. From the trend seen in the

measurements in Figure 4.11, the dark current in an irradiated sample should return to the normal values of the dark current of the unexposed sample if the measurement is extended for more than 2000s.

The x-ray generated current, also termed as "photocurrent" at 100s and 400s did not reach the same peak of current density during the irradiation. Even though the x-ray exposure of 1.1 Roentgen, average energy 34.2 Kev and exposure time of 3s are maintained constant, the current density during the exposure at 100s and 400s did not exhibit at the same level in *p-i-n* sample and *n-i-p* sample with aluminum contact and these are illustrated in Figure 4.10 and Figure 4.11. It is important to emphasize that the initial photocurrent is very difficult to measure because of the response time limitation of the measuring circuit (including the current limiting resistance)

In Figure 4.10, the dark current density after x-ray irradiation at 400s merges with the dark current density at approximately the 780 s mark but dark current density after irradiation at 100s did not seem to merge with the dark current in the unexposed case at point D. The x-ray induced current in the third cycle (dark transient when the sample exposed at 400s) is approximately 10 times greater than the dark current measured in the unexposed sample.

In Figure 4.11, after the application of a positive voltage to the top electrode in the *n-i-p* sample with a aluminum contact, the dark current starts to decrease and a major reduction in dark current can be seen at around 300s. The sample is irradiated at 100s with x-rays and x-ray induced photocurrent has jumped from a dark value of 10^{-11} to 10^{-9} A which has increased by 2 orders of magnitude. After 3s (the termination of x-ray irradiation), the dark current starts to decrease. The observation of a large and decaying dark current immediately after x-ray irradiation can be tentatively explained as follows. During the x-ray irradiation, electrons and holes will be generated and these will be drifting under the applied field. Some of these will be trapped. In addition, x-ray irradiation will generate additional defects in the structure which can capture electrons and/or holes; as shown, by Walornyj [62] Further, x-ray generated carriers electrons within the *n*-layer can recombine with trapped holes in this layer and hence reduce the positive space charge within the *n*-layer. Similarly, x-ray generated holes which recombine with trapped electrons in the *p*-layer. Consequently, after the cessation of x-ray irradiation, the field across the sample would be significantly modified. Therefore, given the decrease in the space charge in the *n*-layer and the *p*-layer, the electric fields at the contacts would also have been modified, that is

increased. Consequently, the carrier injection rates would be higher. With time, holes injected from the positive electrode will become trapped in the *n*-layer, and electrons injected from the negative electrode will become trapped in the *p*-layer and slowly restore the *n*- and *p*-layers to their normal space charge capacity. In addition, the release of trapped x-ray generated carriers from the bulk (*i*-layer) will also contribute to the modification of the field.

In Figure 4.12, the dark current density after x-ray irradiation at 400s and 100s merges at point D (in approximately at 1200s), but these two curves do not seem to merge with the dark current measured when the sample is not irradiated. There is approximately 0.4 pA mm^{-2} difference between the two dark current densities between the samples with and without radiation at 1200s, which is not a large difference, given that the current levels are already very small. The x-ray generated photocurrent in the second cycle appears to be approximately 1000 times greater than the dark current measured in the unexposed sample.

When the sample is irradiated, the photocurrent reaches an upper limit of 10^{-9} A for the aluminum electrode sample, and 10^{-7} A for the platinum electrode sample. For Al, the photocurrent increases about 200 times from the initial dark current value and for Pt, it has increased by 400 times. The platinum contact to the sample gives invariably higher dark current than the aluminum contact due to the predictable model of injection over a Schottky barrier i.e. higher the work function (φ) of the contact metal, the lower the barrier to the injection of holes. The work function of platinum is φ = 5.65 eV is higher than the Aluminum contact work function, with φ = 4.25 eV. The *n-i-p* sample with the Pt contact has always revealed higher dark current compared to the aluminum contact in *n-i-p* sample.

After the end of the exposure in Figure 4.11and Figure 4.12, at around 500s, the dark current decay stays less than 1 order of magnitude to the normal value with no-exposure measurements and it is about 10^{-11} Amps and this can be seen for both Al and Pt contacts.

With the application of a constant nominal electric field of 10 V μm^{-1} to the sample, and x-ray exposure of 1.12 Roentgen for 3s, at an average energy of 34.2 keV, generates a large amount of electron-hole pairs in the sample and the generated EHP's can interfere significantly with the space charge region by the process of trapping and recombination. Subsequently, the space

charge regions built up after the irradiation is far different than they were before and therefore, as explained above, different currents will flow through the sample.

This big difference in the x-ray induced dark current and the dark current in the unexposed sample suggests that the electric field at the positive electrode (the radiation receiving electrode) has increased after irradiation. The reasons were explained above. There is one additional contribution. The x-ray photo generation in a-Se depends on the electric field. As x-ray generated electrons in the *n*-layer recombine with trapped holes in this layer, and hence reduce the space charge, which causes the electric field near the contact to increase. The latter increase leads to even more x-ray generated electrons and holes, which further reduces the positive bulk space charge in the *n*-layer. It is therefore quite likely that the deterioration of the blocking effectiveness of the *n*-layer that leads to the observed greater dark current than the deterioration of the *p*-layer.

4.6 Multiple X-ray Irradiations

Background

In the past, research work has been performed on single layer and multilayer a-Se structures with various applied bias fields, and using a single x-ray exposure. Recent numerical calculations [63] have predicted that during a series of x-ray exposures with short and dark rest periods measured immediately before each exposure will increase with accumulating exposure due to the shifting field distribution within the sample. In order to seek experimental evidence for the numerical calculations, several experiments were performed on a-Se structures that belongs to a sample set A and set C.

Experimental Results and Discussion

Experiments were performed on *p-i*, *n-i*, *i-layer*, *p-i-n* and *n-i-p* a-Se sample structures and dark current transients were measured with samples exposed periodically to x-ray radiation for 3s. The above sample structures were examined under different applied bias fields and irradiated at specific time intervals for every 200s until a total time of 2000s is reached. As usual, a reverse bias (positive bias to the *n*-side and negative bias to the *p*-side) is applied to all the sample structures during the experiment because, as explained earlier, the application of a reverse bias voltage leads to a much lower dark current compared to the forward bias case. Experimental results are illustrated in Figure 4.13, 4.14, 4.15, 4.16, 4.17 and 4.18.

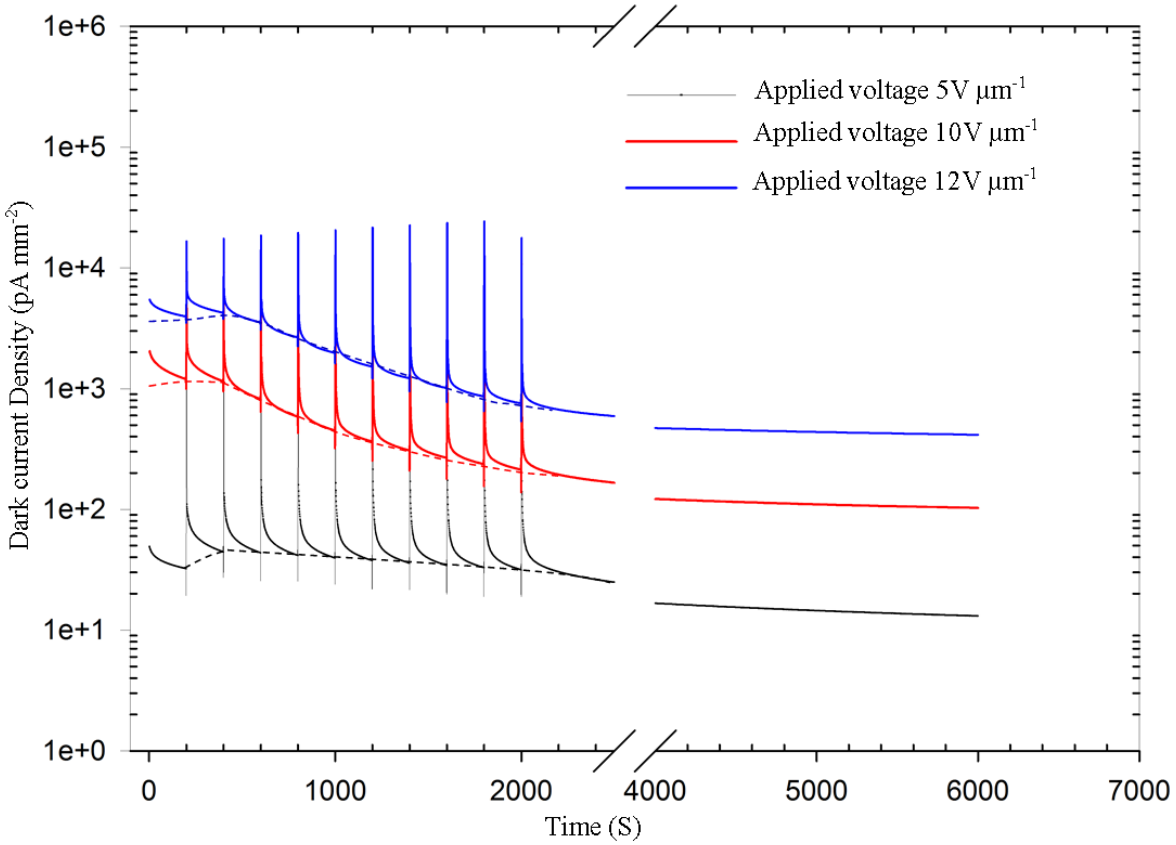

Figure 4.13: The measured transients with different applied voltages for the *p-i* sample with a Cr contact. This sample belongs to the sample set A. Dark current measurements were taken for different applied fields of 5 V μm^{-1}, 10 V μm^{-1} and 12 V μm^{-1} for 6000s. The sample is irradiated 10 times, starting from 200s to 2000s with x-rays at every 200^{th} s.

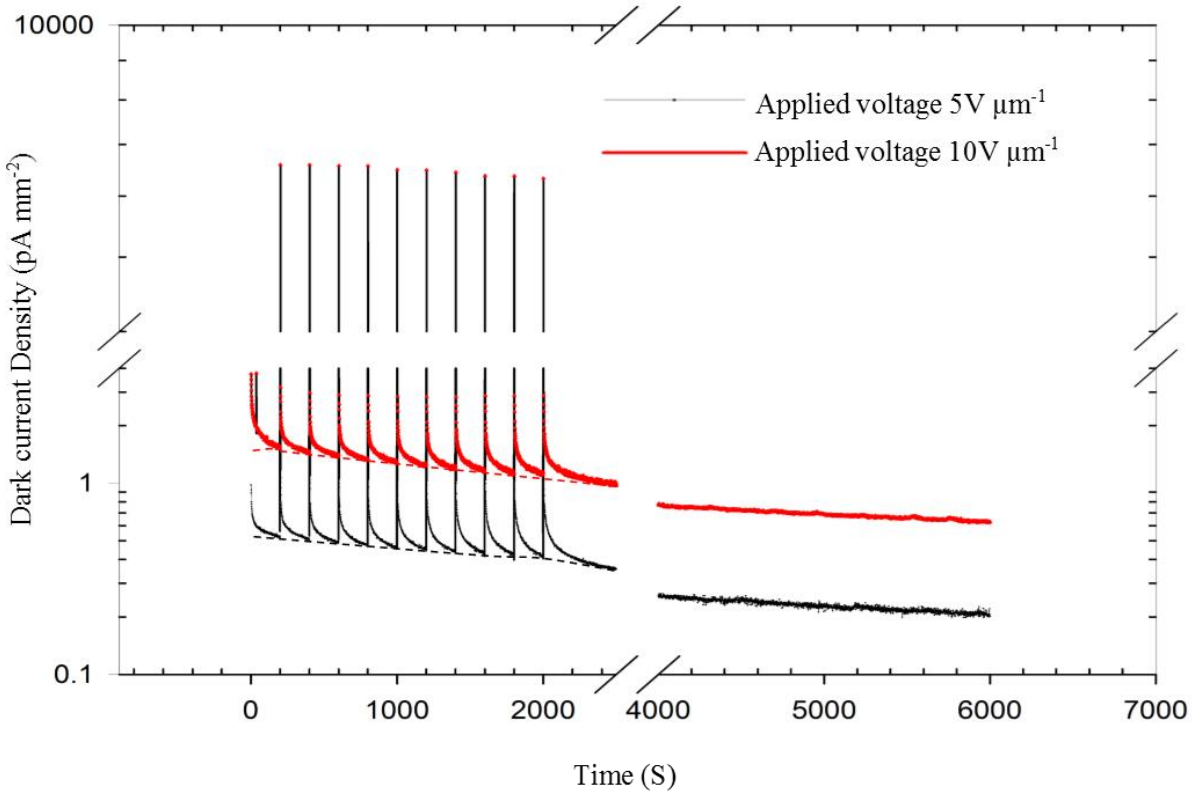

Figure 4.14: Dark current transients for the *n-i* sample with different nominal applied fields (reverse bias) of 5V μm^{-1} and 10 V μm^{-1} for 6000s. The sample is irradiated 10 times starting from 200s to 2000s. This sample belongs to the sample set A. The peak observed at every 200th second until 2000s is the photocurrent in the sample generated by the x-ray radiation.

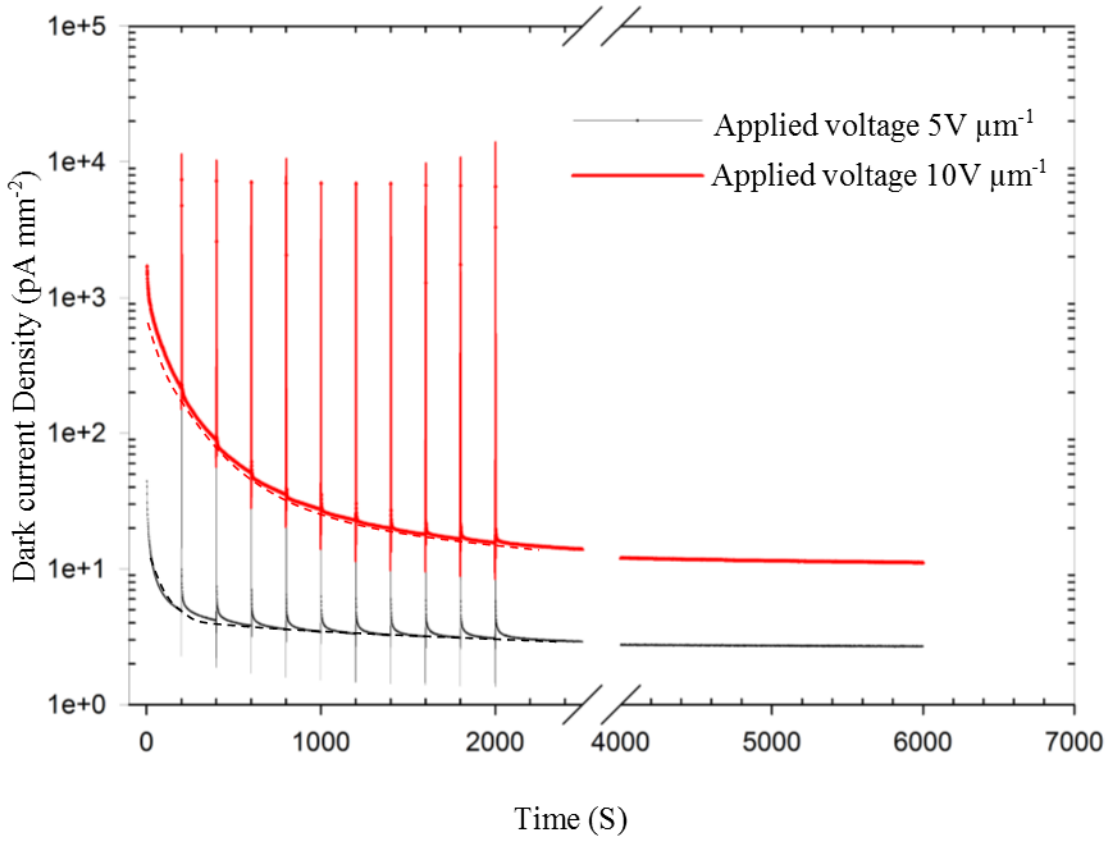

Figure 4.15: Dark current transients for an *i*-layer only with different applied fields of 5 V μm^{-1} and 10 V μm^{-1} for 6000s. The sample is irradiated 10 times starting from 200s to 2000s. This sample belongs to the sample set A. The peaks observed at every 200^{th} second until 2000s is the photocurrent in the sample generated by the x-ray radiation.

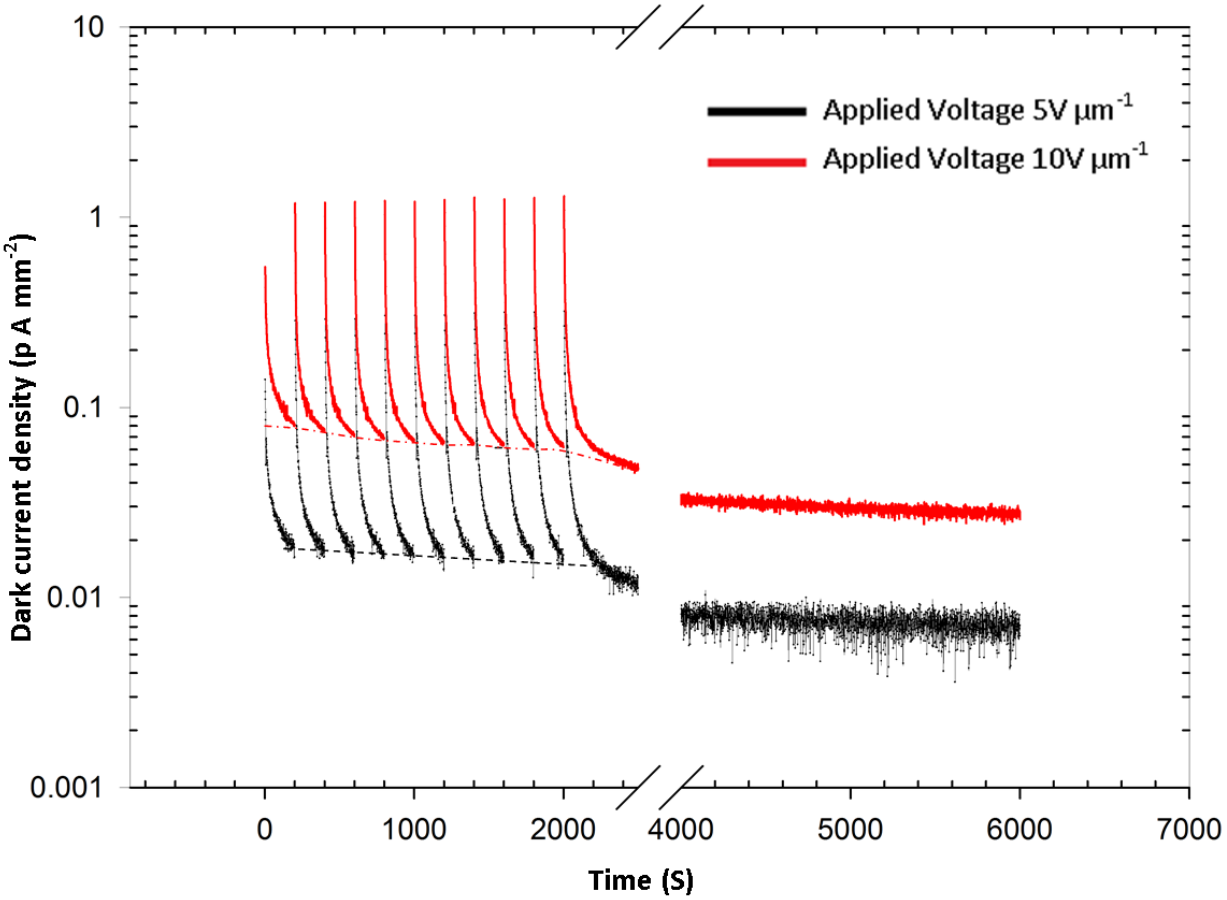

Figure 4.16: Dark current transients for a *p-i-n* sample with a chromium contact for different applied fields (reverse bias) of 5 V μm^{-1} and 10 V μm^{-1} for 6000s. The sample is irradiated 10 times starting from 200s to 2000s. This sample belongs to sample set A. The peak observed at every 200th second until 2000s is the photocurrent in the sample generated by the x-ray radiation.

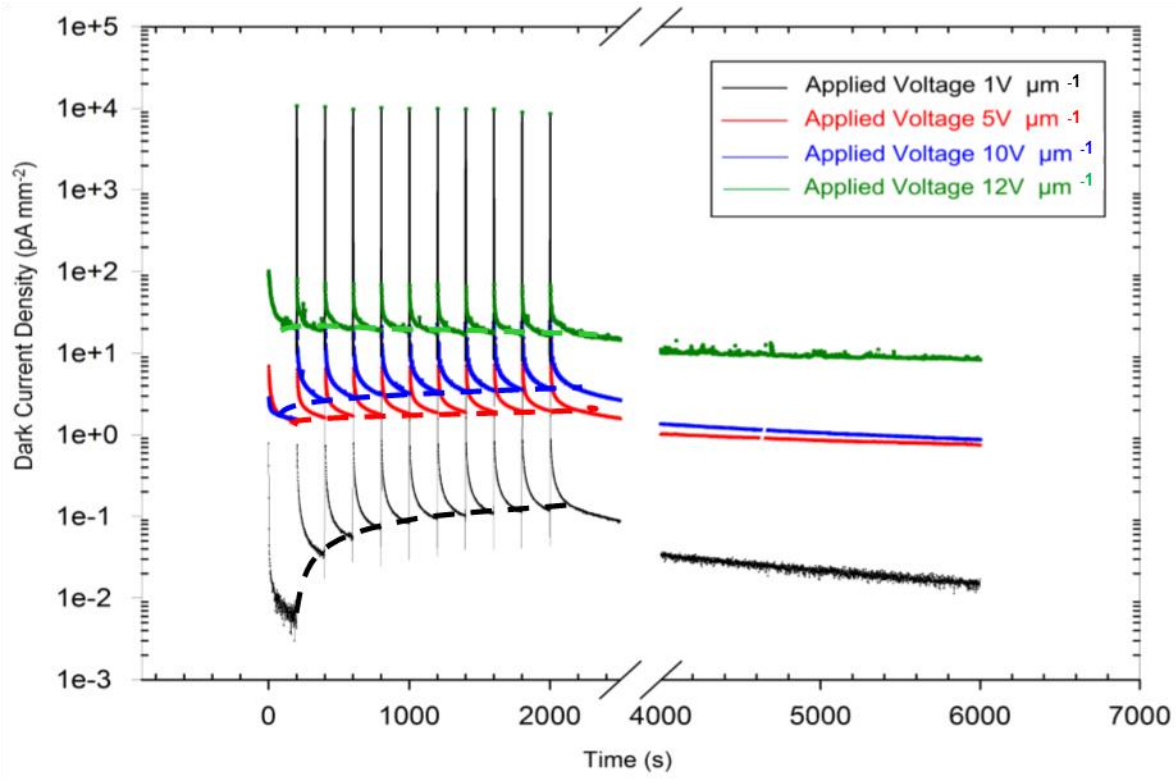

Figure 4.17: Dark current transients for the *n-i-p* sample with a platinum top contact and with applied voltage of field (reverse bias) of 1V μm^{-1}, 5 V μm^{-1}, 10 V μm^{-1}, 12 V μm^{-1} for 6000s. The sample is irradiated 10 times starting from 200s to 2000s. X-ray induced photocurrent peaks can be observed at every 200th second until the end of exposure at2000s. This sample belongs to the sample set C.

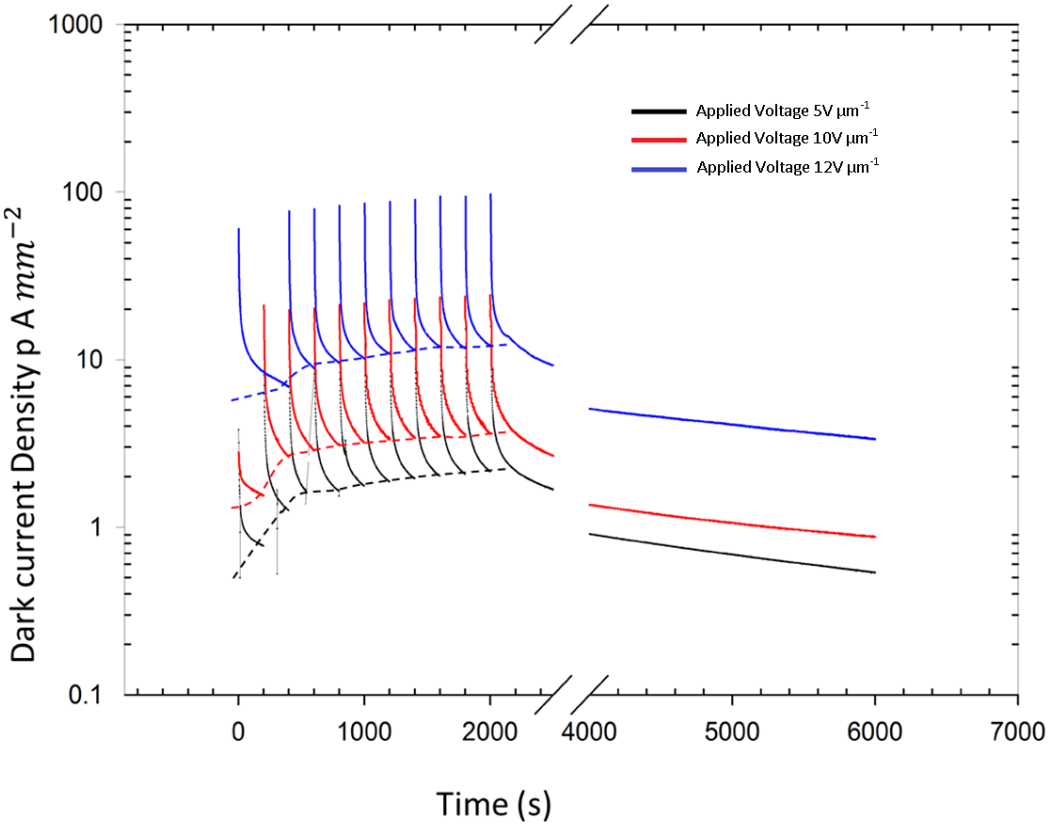

Figure 4.18: Dark current transients for the *n-i-p* sample with an aluminum top contact and with applied voltage of positive 5 V μm^{-1}, 10 V μm^{-1}, 12V μm^{-1} for 6000s. The sample is irradiated 10 times starting from 200s to 2000s. X-ray induced photocurrent peaks can be seen at every 200second on the plot until we reach 2000s. This sample belongs to the sample set C.

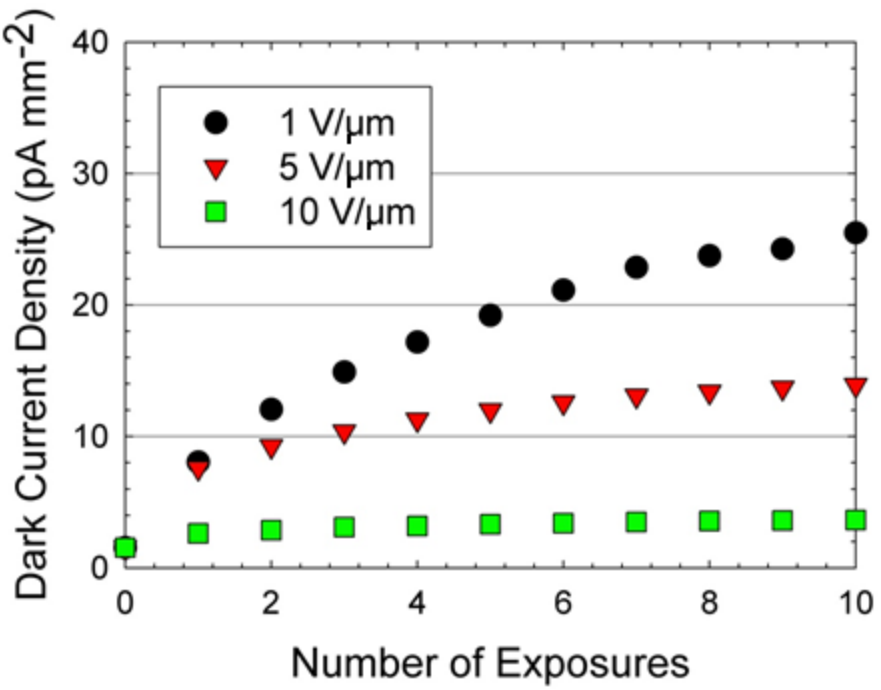

Figure 4.19: The relative increase in the dark current vs, number of exposures (accumulated dose) at three different fields for the *n-i-p* sample with a platinum contact.

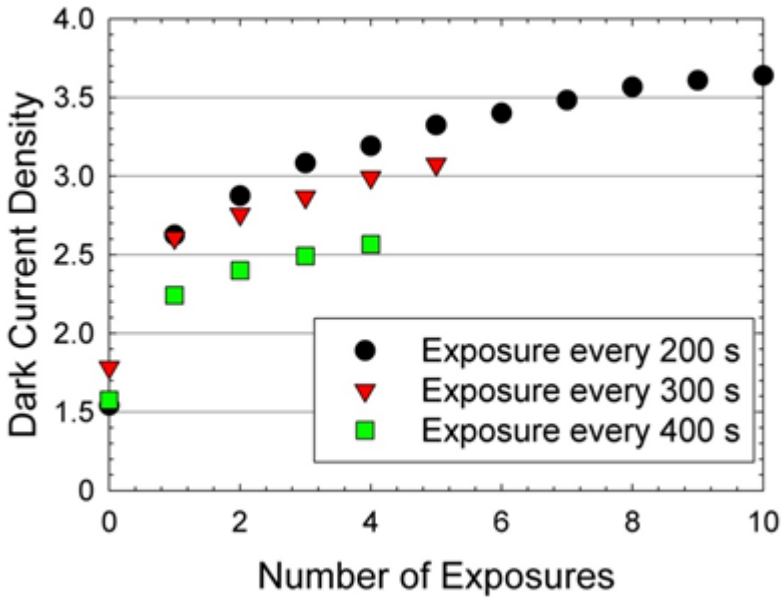

Figure 4.20: The relative increase in dark current as a function of number of exposures (accumulated dose) at various exposure levels for the *n-i-p* sample with a platinum contact.

Transients is recorded by irradiating the sample at every 200s, 300s and 400s. The applied electric field to the sample is 10 V μm^{-1}.

Figure 4.13, illustrates the dark current transients for *p-i* device when it is irradiated periodically for every 200s with the device biased at three difference fields, corresponding to 5V μm^{-1},10V μm^{-1} and 12V μm^{-1}.

From the plot, it is observed that, as expected, the dark current increases with the applied field. The photocurrent peaks can be observed at every 200s in the dark current transients until the 2000 mark is reached

For every increase in negative applied bias voltage, increase in dark current can be seen in the plot as expected. The dark current after each exposure attempts to recover to the normal level and the steep decrease in the dark current after cumulative exposure can be observed from Figure 4.13.

The dark current in *p-i* sample is comparatively higher than *n-i*, *p-i-n*, *n-i-p* samples because of the absence of the *n*-layer in the structure. The absence of the *n*-layer means that there is no hole injection blocking layer next to the positive electrode. This layer normally has trapped holes and hence a positive bulk space charge, which reduces the field at the contact and hence reduces the hole injection rate from the metal into the *n*-like a-Se. As noted in [3], the hole mobility in a-Se is much higher than the electron mobility and hole drift constitutes the major part of the dark current.

The *p-i* sample used in this experiment has a non-chlorinated *i*-layer and electron trapping is unlikely in the *i*-layer. Electrons are only trapped in the blocking *p*-layer. The top layer receives most of the radiation and the generated holes recombine with the electrons trapped in the *p*-layer and decrease the negative space charge in the *p*-layer. This might be reason why field distribution increases initially until 400s. However, after 400s, there is a decrease in the current with the cumulative exposure.

Figure 4.14 illustrates the dark current transients for *n-i* layer sample when it is irradiated periodically for every 200s with applied bias fields of 5V μm^{-1} and 10V μm^{-1}. It is clear that

reducing the field results in lower dark currents, for example, the dark current at 5V μm^{-1} is less than that at 10 μm^{-1} but lower fields also mean lower x-ray sensitivity, because the ionization energy depends on the field [18].

The intrinsic layer in the *n-i* sample has a non-chlorinated layer and there is no *p*-layer present in the sample. There is no effective trapping of electrons happening in this sample because of the non-chlorinated *i*-layer and the absence of *p*-layer. There is no increase in dark current due to cumulative exposure and the dark current in this sample is mainly due to the flow of electrons because of the absence of the *p*-blocking layer at the negative electrode.

In Figure 4.14 the dark current after each exposure reduces compared to the dark current level due to previous irradiation thereby reducing the total dark current value due to cumulative exposure. The measured dark current density at 1 second is 0.6 pA mm^{-2} when the applied voltage is 5V μm^{-1} and dark current density at 6000s is 0.2 pA mm^{-2} which is less than the starting value of dark current for the *n-i* sample.

Due to the applied bias voltage across the sample, the injected positive charge carriers are trapped in the *n*-blocking layer which causes an effective trapping layer for holes. The *n*-layer therefore has a positive bulk space charge density within the layer and there is therefore a reduction in the field at the positive contact. The dark current decay in this sample is mainly due to the injection of electrons from the negative electrode. As there is no *p*- type blocking layer in this sample to trap electrons, the dark current is controlled by the injected electron carriers. The photo current during each exposure reaches an even level of 6500 Amps mm^{-2} and tries to come back to the lower level value observed before each exposure.

Figure 4.15 represents the dark current transients for the *i*-layer sample with photocurrent peaks seen at every 200^{th} s until the 2000s mark is reached. The dark current transients were recorded for the applied bias field of 5V μm^{-1} and 10V μm^{-1}. Application of positive bias and negative bias to the intrinsic sample did not lead any significant changes in the dark current results.

With cumulative exposure to the intrinsic sample, the dark current reduces monotonically and it can be seen clearly when the bias field is 5V μm^{-1}. After each exposure, the dark current tends to decrease and reaches a value less than the value observed before exposure. The dark current

transient values are comparatively very high than dark current transients observed in *p-i* , *n-i*, *p-i -n* and *n-i-p* samples. As the blocking layers are absent in this single *i*-layer, there is no control of the electric fields at the electrodes.

In the course of x-ray irradiation, the photogenerated holes will drift towards the negative electrode and the hole concentration increases towards the negative electrode. The electron charge carriers generated due to x-ray irradiation will drift towards the positive electrode. The injected electrons and holes are trapped by some localized states and deep states present in the intrinsic layer. Even though the deep trap centers start to become full, the x-ray exposure on the sample continuously creates more deep trap centers and therefore leads to continuous carrier trapping. As a result of high concentration of deep traps, higher rate of recombination occurs in *i-layer* with drifting carriers

The internal field depends on the relative distribution of trapped charges in deep traps. During the x-ray irradiation, some of the x-ray generated electrons and holes become trapped as well, though the fact that the dark current does not change significantly means that it is unlikely that the x-ray generated and trapped carriers lead to a major field distribution in this device.

The dark current voltage characteristics of pure a-Se single layer films with electrodes have been studied by a number of researchers [64]. In single layers, the dark current is believed to a mixture of emission limited current at the electrodes and bulk space charge controlled transport as discussed by Belev and Kasap.

Figure 4.16 represents the dark current transients for a *p-i-n* sample with applied reverse bias fields of 5 V μm^{-1} and 10V μm^{-1} for 6000s. The photocurrent peaks can be seen at every 200s until the 2000second mark is reached. The dark current density in this sample structure after multiple exposures has recorded a lesser value of dark current compared to *p-i*, *n-i* and intrinsic sample structures. This is due to the fact that this sample has two blocking layers, that is, *p*-layer and *n*-layer on both the sides of the sample.

The *p*-layer and *n*-layer have made a significant contribution in trapping the injected electrons and holes respectively. However the dark current transient recorded in the *p-i-n* sample failed to provide experimental evidence for the increase in dark current due to cumulative exposure.

It is also observed that the dark current in this *p-i-n* sample is more than the dark current observed in *n-i-p* sample in Figure 4.17. This might be due to the fact that the *p-i-n* sample has a non-chlorinated *i*-layer which does not trap electrons effectively. The injected electrons are trapped only in the *p*-layer whereas the injected holes are trapped in the *n*-layer (bottom layer on ITO) which causes effective trapping of holes. Therefore, several minutes after the application of a bias voltage, electron current becomes more significant and dominant and consequently the electrons become the main contributor to the dark current in the *p-i-n* sample. The electric field distribution changes across the *p-i-n* photoconductor sample idue to the cumulative exposure. The theoretical modelling on *p-i-n* sample was performed by Manouchehri also has the change in the electric field distribution during the accumulated exposure and it is illustrated in Figure 4.21.

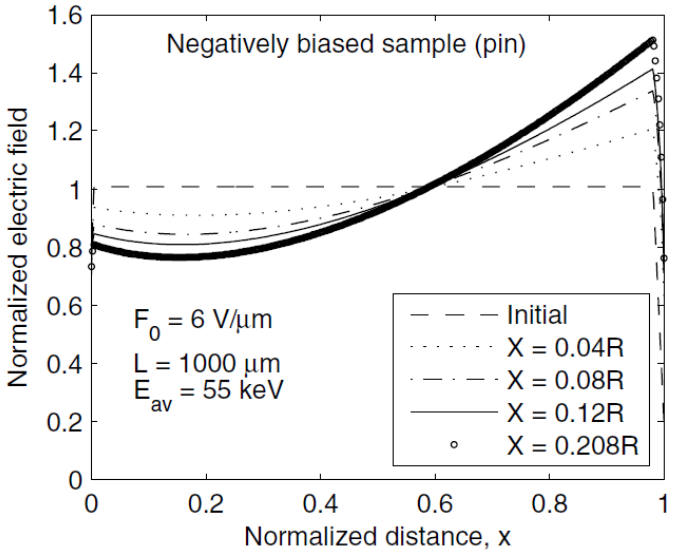

Figure 4.21: Change in Electric field distribution due to cumulative exposures, theoretical modelling by Manouchehri on *p-i-n* sample. (After [63])

Figure 4.17 represents the dark current transients for an *n-i-p* sample with a platinum contact when the sample is irradiated at every 200th second until the 2000second mark is reached. The measurements were recorded when the bias applied field to the sample was 1V μm^{-1}, 5 V μm^{-1}, 10 V μm^{-1}, 12V μm^{-1} for 6000s. It is observed that the dark current increases with cumulative exposure and the dark current measured after every exposure is greater than the mark observed before exposure and this behavior can be clearly seen in the transient when the applied field is positive 1V μm^{-1}. Until the last irradiation, the increase in the dark current density is observed and the dark current starts to decrease in the absence of irradiation after the 2000 mark is reached

beyond which the sample was not irradiated. During each irradiation, the photocurrent has reached the same value of current and this can be observed by the spikes at every 200s interval till 2000s is reached. The dark current tends to increase exponentially when the applied bias to the sample was less.

Manoucheri in his recent work [63][56] has predicted that the *n-i-p* sample with applied reverse bias voltage has revealed increase in dark current density with accumulated cumulative exposure and this *n-i-p* sample structure with platinum contact has provided experimental evidence for his theoretical work. There is a change in field distribution due to the injected carriers and the cumulative radiation on the sample. The field in the sample near the radiation receiving electrode increases as shown in a model calculation in Figure 4.22. This is because the x-ray generated electrons recombine with trapped holes in the *n*-layer, and the space charge become reduced, which means an increase in the field at the contact.

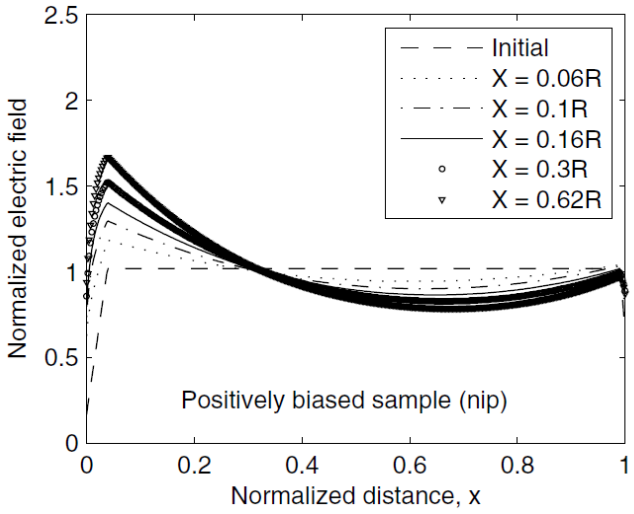

Figure 4.22: The electric field distribution across the *n-i-p* photoconductor for different cumulative exposures, after Manouchehri [63]

The increase in dark current density transients is clearly visible when the applied field to the sample was $1V\mu m^{-1}$, $5V\mu m^{-1}$ and $10V\mu m^{-1}$. When the applied bias voltage is $12V\ \mu m^{-1}$ there is not much of significant change in the dark current density.

Figure 4.18 represents the dark current transients for an *n-i-p* sample with an aluminum contact when the sample is irradiated at every 200th second until the 2000s mark is reached. The measurements were recorded when the reverse bias field applied to the sample was 5 V μm^{-1}, 10 V μm^{-1} and 12 V μm^{-1} for 6000s. The dark current tends to increase at every exposure and this behavior can be seen until the sample is exposed until 2000s. This can be seen in all the dark current transients when the applied bias voltage is 5 Vμm^{-1}, 10 Vμm^{-1} and 12Vμm^{-1}. After 2000s the dark current starts to decrease (the repeated exposures cease) and attempts to recover and reach a steady state value.

This *n-i-p* sample with an aluminum contact also has given experimental evidence for Manoucheri's theoretical work by producing increased dark current density with accumulated cumulative exposure under reverse bias condition.

Figure 4.19 represents the relative increase in the dark current density with various reverse applied fields for the *n-i-p* sample with Platinum contact. The applied bias fields to the sample are 1 V μm^{-1}, 5 V μm^{-1} and 10V μm^{-1}. The dark current tends to increase exponentially when the applied bias to the sample was less. A sharp increase of dark current can be seen at every exposure when the applied bias field to the sample was 1 V μm^{-1} but this scenario was not seen in the dark current transient recorded at high field 10V μm^{-1}.

Figure 4.20 represents the relative increase in dark current at various exposure levels for an *n-i-p* sample with a platinum contact. The dark current transients were recorded when the applied bias field to the sample was 10 V μm^{-1}.The sample was exposed at regular intervals for every 200s, 300s and 400s. The dark current measured when the sample was exposed at 200s lead to higher levels when compared to the dark currents corresponding to exposures at 300s and 400s. The higher the resting period between irradiation, the smaller is the build-up in the dark current due to repeated x-ray exposures.

For the reverse biased *n-i-p* sample, the relative dark current versus time can be seen in Figure 4.23.

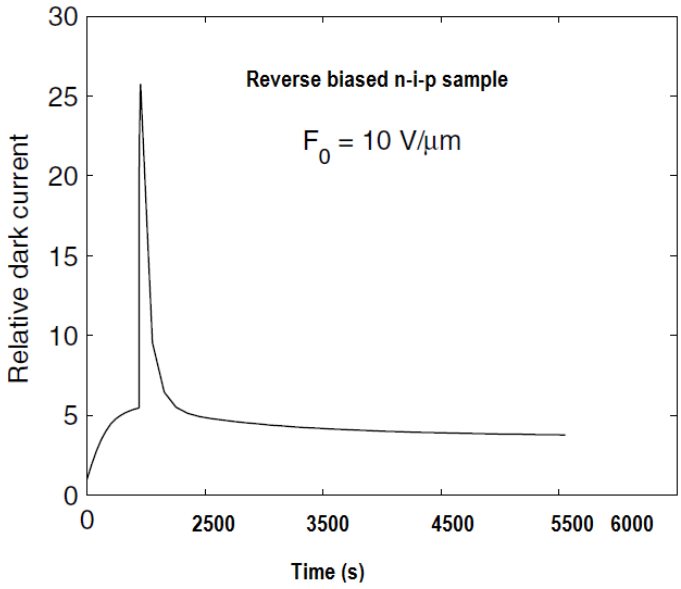

Figure 4.23: Relative dark current vs time for *n-i-p* sample under reverse bias after cumulative exposures

From all the multiple exposure experiments on *p-i-n* and *n-i-p* samples, it is evident that the electric field increases with accumulated x-ray exposure at both the contacts. This shows that dark current has a dependence on electric field at the contacts. When irradiating the sample multiple times, a significant number of photo generated carriers may recombine with the trapped charges present in the blocking layers. This will temporarily reduce the charges in the blocking layer and hence change the field at the electrodes. The field will increase at the contacts, leading to an increase in the dark current [63]. The rise in the dark current due to exposure can be fully recovered by resting the sample for a period of at least 2 h. After 6000s, a significant recover has taken place as can be seen in Figure 4.17 and Figure 4.18.

CHAPTER 5. SUMMARY AND CONCLUSIONS

Direct digital radiography is an important tool in breast cancer diagnosis that relies on photoconductive detectors for converting the incident x-ray photons to charges and hence to a digital image. The X-ray flat panel detector is self-scanning and the images are recorded and displayed immediately. Stabilized a-Se semiconductor material is currently the only semiconductor commercialized as a photoconductive material in mammographic detectors, because large area uniform layers can be economically fabricated using vacuum deposition techniques. Although a-Se is a suitable material for a flat panel detector, dark current which is an important characteristic becomes the source of noise which can impact the dynamic range of the detector and the detective quantum efficiency. Despite the extensive use of a-Se in commercial detectors, we still do not know the effect of x-ray exposure on the dark current. Throughout the course of this work, the dark current in practical a-Se photoconductive detectors were studied as a function of x-ray dose delivered into the detector

Both single X-ray exposure and multiple X-ray exposures were used. Dark current in *p-i, i- , n-i, p-i-n* from Set A and *n-i-p* sample from Set B were studied. Dark current was also studied under different resting periods, as a function of sample structure, discharge measurements, single irradiation on the sample and multiple irradiations on the sample.

X-ray irradiation was from a tungsten cathode x-ray tube. The average x-ray photon energy was 34.2 keV. The average exposure rates were approximately 1.12 R/s. The average delivered dose was calculated to be 0.46 Gy R^{-1} or 0.51 Gy s^{-1}.

5.1 Dark Current for Different Rest Time Periods

The dark current following the application of a step voltage to an a-Se photoconductor sandwich structure decays with time, over time scales from seconds to hours. Several experiments were performed by resting the sample for different time periods to find the acceptable dark rest period that leads to reproducible results, i.e. most trapped charges in the bulk j- of the material would have been discharged. a-Se samples *p-i. n-i, i- and p-i-n* from Set A and *n-i-p* sample from set B were rested for 8 hours and the dark current transient was measured for each. Similar experiment was performed on the samples after resting them for 12 hours and 24 hours. It is observed that

after 24 hours of rest, acceptable value of low dark current was obtained on these samples. These measurements were recorded when the sample was biased at 10 V/μm and also during short – circuit conditions while the sample was resting in the dark. All further experiments in this work involved resting the sample for 24-hour period, which was sufficiently long enough to release the trapped charge carriers which resulted in a reproducible dark current

5.2 Dark Current of Different Sample Structures

Dark current measurements were performed on different samples from sample set A and set B with an applied bias voltage of 10 $V\mu m^{-1}$. The experiment was performed after resting the samples for 24 hours. From the experiments, it was observed that *n-i-p* and *p-i-n* samples exhibit much less dark current values compared to other samples. The reason for less dark current density in these samples is due to the three layered structure of the sample. The injected holes are trapped in the *n*- blocking layer and injected electrons are trapped in the *p*- blocking layer. Single layered *i*- sample from Set A has the highest dark current than any other sample. This is due to the absence of blocking layers in the sample structure. Two layered *p-i* and *n-i* sample has dark current densities that exhibit dark currents less than that in the *i*-layer but higher than the three-layer *p-i-n* and *n-i-p* samples. The blocking layer in the *p-i* sample blocks the injection of electrons into the bulk (*i*-layer) but the holes are not trapped, whereas the injected holes are trapped in the *n –layer* in the *n-i* sample. The dark current in the *n-i* structure is much less than that in the *p-i* layer. These experiments support the theory that the dark current is controlled by the injection of charge carriers from the contacts.

5.3 Dark Current under Single X-ray Exposure.

Single irradiation experiments were performed on the samples from Set A and Set B. Samples were exposed to X-rays at 100s and 400 s. at the dose rate of 0.51 Gy s^{-1} and the exposure duration was 3s. During exposure, reverse bias voltage was applied to the samples, that is, they were biased as if they were being used in x-ray detection. There was a sudden increase in the current during exposure, which is the photocurrent. With the sample being irradiated, large number of electron- hole pairs are generated and they collapse the space charge region (by recombination) that was built by trapping. Therefore, the space charge region within the blocking layers after irradiating the sample is very different than they were before, and this leads to a different flow of current through the sample. The reason is that the change in the space charge in

the blocking layer alters the field at the electrode, which changes the rate of carrier injection. The experiments were performed for 2000 s, and in most of the samples, the dark current after irradiation did not reach the value of dark current in the absence of irradiation. However, after a dark rest period of 24 hours, the dark current was very close to its value before exposure.

5.4 Dark Current under Multiple X-ray Exposure

Dark current transients were measured on sample under different reverse bias voltages and the sample was irradiated 10 times from 200 s to 2000 s, with each exposure corresponding to a dose rate of 0.51 Gy s^{-1}. With the increase in the applied voltage, the dark current, as expected, increases. After time t = 4000 s, the dark tends to reach a steady state in all the samples.

Similar experiments were performed on the *n-i-p* sample, with the sample being irradiated at every 300 s and 400 s under an exposure of, with a delivered dose of 0.46 Gy R^{-1}. Differences in the dark current were observed. When the interval between exposures is small, a higher increase in dark current can be seen. The reason is that during a small time interval, there is less time for the sample to recover (relax) during which trapped carriers are released.

With the application of different reverse bias voltages (1 Vμm^{-1}, 5 Vμm^{-1}, 10 Vμm^{-1}) to the *n-i-p* sample, the dark current transients were measured. At the application of 1 Vμm^{-1}, there is a sharp increase in the dark current with multiple irradiations to the sample. However, at the highest fields (10 V μm^{-1}), there is essentially no change in the dark current with multiple exposure.

5.5 Recommendations for Future work

Although the influence of dark current after single and multiple X-ray exposures were studied, it would be beneficial to perform dark current experiments as a function of temperature. In order to perform this experiment, a measurement chamber which is purged with inert gas is required as it will avoid the condensation problems when the temperature is brought close to + 5°C. Care should be taken while cooling the sample, as they can crack and peel a-Se off the substrate at cooling temperatures. Dark current transient experiments should be performed with X-ray exposure and without exposure. It would be interesting to perform this experiment at lower temperature and find the resultant dark current. It would also be very useful to carry out the experiments at a higher temperature, for example at 35°C but below the glass transition temperature (50-60°C).

REFERENCES

[1] R.F. Mould,"Röntgen and the discovery of X-rays", *British Journal of Radiology* 68 (1995) 1145-1176.

[2] Michael Y. M. Chen, C.T. Whitlow, "Scope of Diagnostic Imaging.", in: Chen MY, Pope TL, Ott DJ (Eds.), *Basic Radiology*, vol 2nd ed, McGraw-Hill;, New York, 2011.

[3] J.B. Frey, An Experimental And Theoretical Study Of The Dark Current And X-ray Sensitivity Of Amorphous Selenium X-ray Photoconductors, Electrical and Computer Engineering, vol Doctor of Philosophy, University of Saskatchewan, Saskatoon, 2011, p. 246.

[4] W. Swindell, S. Webb, "X-ray Transmission and Computed Tomography", in: S. Webb (Ed.) *Physics of Medical Imaging*, 1988.

[5] M. Körner, C.H. Weber, S. Wirth, K.-J. Pfeifer, M.F. Reiser, M. Treitl,"Advances in Digital Radiography: Physical Principles and System Overview", *Radiographics* 27 (2007) 675-686.

[6] L. Lança, A. Silva,"Digital radiography detectors – A technical overview: Part 1", *Radiography* 15 (2009) 58-62.

[7] M.J. Samei E Fau - Flynn, M.J. Flynn,"An experimental comparison of detector performance for direct and indirect", *Med Phys* 30 (2003) 608-622.

[8] S.O. Kasap, J.A. Rowlands,"Direct-conversion flat-panel X-ray image detectors", *Circuits, Devices and Systems, IEE Proceedings* - 149 (2002) 85-96.

[9] C.C. Society, Canadian Cancer statistics 2012, 2012.

[10] S. Kasap, J.B. Frey, G. Belev, O. Tousignant, H. Mani, J. Greenspan, L. Laperriere, O. Bubon, A. Reznik, G. DeCrescenzo, K.S. Karim, J.A. Rowlands,"Amorphous and Polycrystalline Photoconductors for Direct Conversion Flat Panel X-ray Image Sensors", *Sensors* 11 (2011) 5112-5157.

[11] G. Belev, S.O. Kasap,"Amorphous selenium as an X-ray photoconductor", *Journal of Non-Crystalline Solids* 345–346 (2004) 484-488.

[12] M. Kabir, S. Kasap, J. Rowlands, "Photoconductors for x-ray image detectors", *Springer Handbook of Electronic and Photonic Materials*, Springer, pp. 1121-1137, 2006.

[13] J. Kaladė, E. Montrimas, J. Rakauskas,"The mechanism of sensitivity reduction in selenium layers irradiated by X-rays", *physica status solidi (a)* 25 (1974) 629-636.

[14] W. Zhao, G. DeCrescenzo, J.A. Rowlands, Investigation of lag and ghosting in amorphous selenium flat-panel x-ray detectors, Medical Imaging 2002, International Society for Optics and Photonics, 2002, pp. 9-20.

[15] M. Kabir, L. Chowdhury, G. DeCrescenzo, O. Tousignant, S. Kasap, J. Rowlands,"Effect of repeated x-ray exposure on the resolution of amorphous selenium based x-ray imagers", *Medical physics* 37 (2010) 1339-1349.

[16] F. Manouchehri, Ghosting and its recovery mechanisms in multilayer amorphous Selenium X-ray detectors, Concordia University, 2008.

[17] J.A. Rowlands,"Current advances and future trends in X-ray digital detectors for medical applications", *Instrumentation and Measurement, IEEE Transactions on* 47 (1998) 1415-1418.

[18] G.S. Belev, Electrical Properties of Amorphous Selenium based Photoconductive devices for application in X-ray image detectors, Electrical Engineering, vol Doctor of Philosophy, University of Saskatchewan, Saskatoon, 2007.

[19] R.A.Street, "Hydrogenated Amorphous Silicon", Cambridge University Press, NewYork, 2005, p. 1-13.

[20] B. Fogal, R.E. Johanson, G. Belev, S. O'Leary, S.O. Kasap,"X-ray induced effects in stabilized a-Se X-ray photoconductors", *Journal of Non-Crystalline Solids* 299–302, Part 2 (2002) 993-997.

[21] B.J. Fogal, Electronic transport properties of stabilized amorphous selenium x-ray photoconductors, vol Masters, University of Saskatchewan, 2005.

[22] B. Kramer, D. Weaire, "Theory of electronic states in amorphous semiconductors", in: M. Brodsky (Ed.) *Amorphous Semiconductors*, vol 36, Springer Berlin Heidelberg, pp. 9-39, 1985.

[23] S.O.Kasap, "Principles of Electronic materials and devices", McGraw-Hill, 2006, p. 285-313.

[24] A. Madan, M.P. Shaw, "The physics and applications of amorphous semiconductors", Elsevier, 1988.

[25] N. Mott,"Electrons in disordered structures", *Advances in Physics* 16 (1967) 49-144.

[26] P.W. Anderson,"Absence of diffusion in certain random lattices", *Physical review* 109 (1958) 1492.

[27] M.H.Brodsky, "Amorphous Semiconductors", New York: Springer -Verlag 1979.

[28] M.H. Cohen, H. Fritzsche, S. Ovshinsky, "Simple Band Model for Amorphous Semiconductor Alloys", *Disordered Materials,* Springer, pp. 14-16, 1991.

[29] J. Marshall, A. Owen,"Drift mobility studies in vitreous arsenic triselenide", *Philosophical Magazine* 24 (1971) 1281-1305.

[30] G. Lucovsky, E. Gerlach, P. Grosse,"The Physics of Selenium and Tellurium", *by E. Gerlach and P. Grosse, Springer-Verlag, New York* (1979).

[31] V. Minaev, S. Timoshenkov, V. Kalugin,"Structural and phase transformations in condensed selenium", *Journal of Optoelectronics and Advanced Materials* 7 (2005) 1717.

[32] S. Kasap,"Handbook of imaging materials", *Marceal Dekker, New York* (1991) 355.

[33] D. Adler, E.J. Yoffa,"Electronic structure of amorphous semiconductors", *Physical Review Letters* 36 (1976) 1197.

[34] S. Kasap,"Photoreceptors: the chalcogenides", *Optical Engineering - New York-Marcel Dekker Incorporated* 74 (2002) 329-368.

[35] D. Adler, E.J. Yoffa,"Localized electronic states in amorphous semiconductors", *Canadian Journal of Chemistry* 55 (1977) 1920-1929.

[36] S. Elliott,"A unified model for reversible photostructural effects in chalcogenide glasses", *Journal of Non-Crystalline Solids* 81 (1986) 71-98.

[37] N.F. Mott, E.A. Davis, "Electronic processes in non-crystalline materials", Oxford University Press,Oxford, 1979.

[38] D. Carles, G. Lefrançois, J. Larmagnac,"A model for steady-state photoconductivity in amorphous selenium", *Journal de Physique Lettres* 45 (1984) 901-906.

[39] F. Greuter,"Electronic surface properties of a liquid semiconductor: selenium", *Journal of Physics C: Solid State Physics* 18 (1985) 2527.

[40] P. Nielsen,"Density of states of amorphous selenium by vacuum photoemission", *Physical Review B* 6 (1972) 3739.

[41] M. Abkowitz,"Density of states in a-Se from combined analysis of xerographic potentials and transient transport data", *Philosophical magazine letters* 58 (1988) 53-57.

[42] W.C. Tan, G. Belev, K. Koughia, R. Johanson, S.K. O'Leary, S. Kasap,"Optical properties vacuum deposited and chlorine doped a-Se thin films: aging effects", *Journal of Materials Science: Materials in Electronics* 18 (2007) 429-433.

[43] S.O.Kasap, "Handbook of imaging materials", Second, CRC Press, Marcel Dekker, NewYork, pp. 329-368, 2002.

[44] H.-Z. Song, G. J. Adriaenssens, E. V. Emelianova, and V. I. Arkhipov, " Distribution of gap states in amorphous selenium thin films", *Phys. Rev. B*, 59 (1999), 10607

[45] M. Kabir, S. Kasap, J. Rowlands, "Photoconductors for X-ray Image Detectors", in: S. Kasap, P. Capper (Eds.), *Springer Handbook of Electronic and Photonic Materials*, Springer US, Boston, MA, pp. 1121-1137, 2007.

[46] J. Beutel, H.L. Kundel, R.L. Van Metter,"Handbook of Medical Imaging, volume 1: Physics and Psychophysics", (2000).

[47] D.C. Hunt, S.S. Kirby, J. Rowlands,"X-ray imaging with amorphous selenium: X-ray to charge conversion gain and avalanche multiplication gain", *Medical physics* 29 (2002) 2464-2471.

[48] M.Z. Kabir, S. Kasap,"DQE of photoconductive x-ray image detectors: application to a-Se", *Journal of Physics D: Applied Physics* 35 (2002) 2735.

[49] W. Que, J. Rowlands,"X-ray imaging using amorphous selenium: Inherent spatial resolution", *Medical physics* 22 (1995) 365-374.

[50] M.Z. Kabir, S. Kasap,"Modulation transfer function of photoconductive x-ray image detectors: effects of charge carrier trapping", *Journal of Physics D: Applied Physics* 36 (2003) 2352.

[51] G. Belev, D. Tonchev, B. Fogal, C. Allen, S.O. Kasap,"Effects of oxygen and chlorine on charge transport in vacuum deposited pure a-Se films", *Journal of Physics and Chemistry of Solids* 68 (2007) 972-977.

[52] S.O. Kasap, J.A. Rowlands,"Review X-ray photoconductors and stabilized a-Se for direct conversion digital flat-panel X-ray image-detectors", *Journal of Materials Science: Materials in Electronics* 11 (2000) 179-198.

[53] M. Kastner, D. Adler, H. Fritzsche,"Valence-Alternation Model for Localized Gap States in Lone-Pair Semiconductors", *Physical Review Letters* 37 (1976) 1504-1507.

[54] S. Mahmood, M. Kabir,"Dark current mechanisms in stabilized amorphous selenium based ni detectors for x-ray imaging applications", *Journal of Vacuum Science & Technology A* 29 (2011) 031603.

[55] J.B. Frey, G. Belev, O. Tousignant, H. Mani, L. Laperriere, S.O. Kasap,"Dark current in multilayer stabilized amorphous selenium based photoconductive x-ray detectors", *Journal of Applied Physics* 112 (2012) 014502.

[56] S.O.K. M.Z.Kabir, and J.A.Rowlands, "Photoconductors for X-ray Image Detectors", in: S.O.K.a. P.Capper (Ed.) *The Springer Handbook of Electronic and Photonic Materials*, Springer Science & Business Media, Germany, 2006.

[57] S. Kasap, P. Capper, "Springer handbook of electronic and photonic materials", Springer Science & Business Media, 2006, Chapter 3, Optical Properties

[58] H. Adachi, K.C. Kao,"Dispersive optical constants of amorphous $Se_{1-x}Te_x$ films", *Journal of Applied Physics* 51 (1980) 6326-6331.

[59] V.I. Mikla, V.V. Mikla,"Xerographic spectroscopy of gap states in Se-rich amorphous semiconductors review", *Journal of Non-Crystalline Solids* 357 (2011) 3675-3688.

[60] H.J.C. Johns," The Physics of Radiology", *Springfield, IL: Charles* (1983).

[61] J.M. Boone, "X-ray production, interaction, and detection in diagnostic imaging ", in: R.L.V.M.J.B.H.L. Kundel (Ed.) *Handbook of Medical Imaging, Volume 1. Physics and Psychophysics*, vol 1, pp. 1-78, 2000.

[62] M. Walornyj, Electron Lifetime and its dependence on Temperature and dose in a-Se Photoconductors, Electrical and Computer Engineering, vol MSc, University of Saskatchewan, 2013.

[63] F. Manouchehri, M.Z. Kabir, O. Tousignant, H. Mani, V.K. Devabhaktuni,"Time and exposure dependent x-ray sensitivity in multilayer amorphous selenium detectors", *Journal of Physics D: Applied Physics* 41 (2008) 235106.

[64] S. Kasap, G. Belev,"Progress in the science and technology of direct conversion X-ray image detectors: The development of a double layer a-Se based detector", *Journal of Optoelectronics and Advanced Materials* 9 (2007) 1-10.